Université du Québec

Institut National de la Recherche Scientifique

Énergie, Matériaux et Télécommunications

BIO/CHEMICAL SENSING AND GENERATION OF REACTIVE OXYGEN SPECIES BASED ON UPCONVERTING NANOPARTICLES

Par

Joe Gerald Jesu Raj

Mémoire ou thèse présentée pour l'obtention

du grade de Philosophiae doctor (Ph.D.)

en sciences de Énergie, Matériaux et Télécommunications

Jury d'évaluation

Président du jury et	Marc-André Gauthier
examinateur interne	INRS-EMT, Université du Québec
Examinateur externe	Fabio Cicoira
Institution	École Polytechnique de Montréal
Examinateur externe	Louis A. Cuccia
Institution	Concordia University, Montreal
Directeur de recherche	Fiorenzo Vetrone
	INRS-EMT, Université du Québec

ABSTRACT

The intention of this thesis is to explore new applications of hybrid near-infrared (NIR) perturbable lanthanide (Ln^{3+}) upconverting nanoparticles (UCNPs) in the fields of DNA biosensing and copper ion (Cu^{2+}) chemical sensing. Furthermore, the use of these UCNPs as well as superparamagnetic iron oxide nanoparticles (SPIONs) functionalized with an organometallic iridium (Ir) complex for the generation of reactive oxygen species (ROS), which are reactive intermediates in photodynamic therapeutic applications, is investigated. First, we investigated DNA biosensing by synthesizing Ln^{3+}-based, UV/blue emitting, thulium (Tm^{3+}) and ytterbium (Yb^{3+}) co-doped $NaYF_4$ UCNPs as the energy donor upon 980 nm NIR excitation. These UV/blue emitting UCNPs were then integrated into polymer-based nanoparticle and this polymer/upconverting nanohybrid material was appropriately functionalized with the probe DNA sequence via its amino end. In a separate synthesis monodispersed gold nanoparticles (AuNPs) and an Ir complex were prepared. The presence of two carboxyl functional groups on the Ir complex provided suitable conjugation chemistry for the covalent attachment of the complex to the surface of AuNPs through a suitable linker molecule having a thiol functional group. The other end of the probe DNA sequence possessing a thiol end was directly functionalized on the AuNPs thus forming the energy acceptor nanohybrid material. The donor UCNP/polymer nanohybrid and the acceptor AuNP/Ir nanohybrid were brought to close proximity through the helical structure formation of the probe DNA. This facilitates the energy transfer between the Tm^{3+}/Yb^{3+} co-doped UCNPs and the Ir complex functionalized AuNPs. Subsequent addition of target DNA sequence resulted in the DNA hybridization and elongation thus increasing the distance between

the donor and acceptor species. Since this energy transfer is distance dependent, a highly sensitive and selective DNA nanosensor was developed that is sensitive to picomolar concentration of target DNA and highly selective up to a single base mismatch. Optical nanosensors based on the Tm^{3+}/Yb^{3+} doping pair in a different upconverting host crystal such as $LiYF_4$ offers many advantages. In contrast to the $NaYF_4$ host matrix, $LiYF_4$ offers more intense NIR to UV/blue upconversion. These optical features of $LiYF_4$ thus enable the designing of multifunctional nanoplatforms based on $LiYF_4$ UCNPs with combined dual-mode (that is, upconversion and conventional luminescence) detection.

In another part of this thesis, we have integrated a naturally occurring, medicinally important organic compound, curcumin, in combination with the Tm^{3+}/Yb^{3+} co-doped $LiYF_4$ UCNPs. This NIR perturbable organic/inorganic nanohybrid material has been successfully used as a chemical sensor for the detection of Cu^{2+} ions and showed high sensitivity, selectivity, biocompatibility and excellent Stern-Volmer features. Energy transfer has been achieved between the donor UCNPs and the locally decorated curcumin as an acceptor or reporter molecule. The energy transfer has been a key feature in sensing of $Cu^{2+}$and was achieved by careful synthesis of UV/visible and NIR emitting $LiYF_4$:Tm^{3+}/Yb^{3+} co-doped UCNPs followed by coating of a thin layer of silica (SiO_2) in order to render them water dispersible. These SiO_2 coated UCNPs act as suitable donor material when functionalized with highly biocompatible curcumin leading to the formation of the inorganic/organic nanohybrid, which has been proven to be an excellent material for sensing of Cu^{2+} ions with high selectivity. The detection limit of this nanohybrid has been found to be 4.75 nM, which is far lower than the allowed Cu^{2+} limit

for drinking water allowed by the United States Environmental Protection Agency (USEPA). This curcumin tagged nanohybrid material also showed a robust selectivity towards Cu^{2+} ion even in the presence of other metal ions including heavy metals.

Another section of this thesis deals with the synthesis of monodispersed $LiYF_4:Tm^{3+}$, $Yb^{3+}@SiO_2$ UCNPs and their functionalization with varying concentrations of the Ir complex, used in the DNA sensing chapter 3 of this thesis, on their surface. The photophysical properties of these $LiYF_4:Tm^{3+},Yb^{3+}@SiO_2$-Ir nanostructures were investigated and it was demonstrated that upon surface functionalization with the Ir complex, a complete quenching of the upconverted UV emission from the Tm^{3+} ions was observed. Following absorption of the upconverted UV light, the Ir complex demonstrated a capacity to generate ROS, which was measured in the presence of a probe molecule 1,3-Diphenylisobenzofuran (DPBF). Spectroscopic studies of the upconversion luminescence showed that the photosensitization of the Ir complex was radiative in nature. To confirm that the generation of ROS was in fact due to photosensitization of the Ir complex from the UCNPs, two control experiments were also carried out. First, $LiYF_4:Tm^{3+},Yb^{3+}@SiO_2$ UCNPs alone (without the Ir complex) were studied to observe if the upconverted UV light itself was capable of generating ROS. Second, the Ir complex alone was studied following excitation at 980 nm. In both cases, no ROS was observed indicating that both the UCNPs and the Ir complex are required to generate ROS. This newly developed $LiYF_4:Tm^{3+},Yb^{3+}@SiO_2$-Ir nanoplatform lays the foundation for the NIR triggered generation of ROS, which effectively eliminates the need for low penetrating, high energy external UV excitation, normally required for such photosensitizers. In addition we have synthesized and integrated a multi-modal

nanoprobe that consists of an Ir complex functionalized on the surface of SiO_2 coated SPIONs. This particular nanohybrid offers generation of ROS under direct UV illumination, however, it allows for the possibility of exploiting the paramagnetic component of the system for potential applications such as magnetically guided targeting and magnetic resonance imaging. The production of ROS is vital in applications with regard to surface oncology. Since the as synthesized Ir complex exhibits intense visible emission under UV excitation, this Ir complex decorated SPIONs system offers multiple applications such as imaging, and ROS generation hence could be used as a multi-modal nanoprobe.

ACKNOWLEDGEMENTS

It is my honor and privilege to express my deepest and sincere gratitude to Professor Fiorenzo Vetrone, for giving me this wonderful opportunity to do my doctoral research under his supervision. It has been a pleasure working with him and I am forever and extremely grateful for his dedicated and sincere guidance, constant encouragements, his trust and the valuable freedom to think and work independently and at my own pace.

I express my sincere gratitude to my colleague Dr. Marta Quintanilla, who had been instrumental during the nascent stage of my research as well as setting up the newly procured optical instrument for measurements in the lab. I am also very much thankful to Dr. Eva Hemmer, Dr. Antonio Benayas Hernandez for their valuable help with the TEM measurements. Special thanks are due to Mr. Yue Huang who worked in tandem with me in the lab and offering his valuable time and help for characterization of the materials whenever needed.

I would like to express my sincere thanks to Professor Federico Rosei, Director of the institute, for extending financial support during my research. Many thanks are also due to INRS-EMT administrative staff Ms. Hélène Sabourin, Ms. Nathalie Graveline, Ms. Nathalie Métras, Ms. Michelle Marcotte, Mr. Sylvain Gingras for their help.

I am forever indebted my late Father Mr. Jesu Raj Michael, my Mom Mrs. Fatima Alphonsa Mary Lourdusamy and my dearest and ever enchanting younger sister Lourdu Jenifa Jesu Raj who has always been a part my life wherever I am.

TABLE OF CONTENTS

CHAPTER 1 – INTRODUCTION

CHAPTER 2 – APPLICATIONS OF UPCONVERTING NANOPARTICLES

CHAPTER 4 – DIRECT NEAR-INFRARED SENSING of Cu^{2+} IONS USING CURCUMIN TAGGED $LiYF_4$:Tm^{3+}, Yb^{3+} UPCONVERTING NANOHYBRID MATERIAL

CHAPTER 5 – NEAR-INFRARED TRIGGERED GENERATION OF REACTIVE OXYGEN SPECIES FROM UPCONVERTING NANOPARTICLES DECORATED WITH AN ORGANOIRIDIUM COMPLEX

LIST OF FIGURES

LIST OF ABBREVIATIONS AND NOTATIONS

AuNPs Gold Nanoparticles

CR Cross Relaxation

DLS Dynamic Light Scattering

DNA De-oxy Ribonucleic Acid

EDC 1-ethyl-3-(3-dimethylaminopropyl)carbodiimide

EDTA Ethylenediaminetetraacetic acid

EDX Energy Dispersive X-ray Spectroscopy

EMU Energy Migration Mediated Upconversion

ESA Excited State Absorption

ETU Energy Transfer Upconversion

FRET Fluorescence Resonance Energy Transfer

FTIR Fourier Transform Infrared Spectroscopy

GSA Ground State Absorption

I Intensity of Emitted Light

I_0 Intensity of Incident Light

Ir (III) Iridium Complex

LOD Limit of Detection

LRET Luminescence Resonance Energy Transfer

MB Molecular Beacon

mM Millimolar

NHS N-hydroxysuccinimide

NIR Near-infrared

nm nanometer

nM Nanomolar

NMR Nuclear Magnetic Resonance Spectroscopy

NPs Nanoparticles

OA Oleic acid

ODE 1-Octadecene

OM Oleylamine

PA Photon Avalanche

PAA Polyacrylic acid

PBS Phosphate Buffer Saline

PDT Photodynamic Therapy

PEG Polyethyleneglycol

PEI Polyethyleneimine

PL Photoluminescence

pM Picomolar

PSA Polystyrene-*co*-acrylic Acid

PSD Particle Size Distribution

PVP Polyvinylpyrrolidone

ROS Reactive Oxygen Species

SPIONs Superparamagnetic Iron Oxide Nanoparticles

TEM Transmission Electron Microscopy

TFA Trifluoroacetic Acid

UC Upconversion

UCNPs Upconverting Nanoparticles

UV-Vis Ultraviolet-Visible

XPS X-Ray Photoelectron Spectroscopy

XRD X-Ray Diffraction Spectroscopy

λ_{em} Emission Wavelength

λ_{ex} Excitation Wavelength

μM Micromolar

CHAPTER 1 - INTRODUCTION

Upconversion is a non-linear optical phenomenon in which low energy NIR light is converted to higher energy UV, visible, and NIR emissions. The upconversion phenomenon has been observed mainly in the lanthanide (Ln^{3+}) materials. Tri-positive Ln^{3+} ions have $4f^n\ 5d^{0-1}$ inner electronic configurations that are strongly shielded by overlying 5*s* and 5*p* orbitals. In addition, they have abundant, ladder-like 4*f* energy levels, which facilitate energy transfer between adjacent levels [1]. Ln^{3+} ions possess sharp emission peaks due to intra 4*f*-4*f* transitions, and although this transition is symmetry forbidden, it becomes partially allowed due to intermixing of 4*f* orbitals with the 5*d* orbitals in Ln^{3+} [2,3]. Due to the versatility of the energy levels involved, Ln^{3+} ions offer extensive photophysical and photochemical properties [4-6]. In particular, the anti-Stokes upconversion phenomenon is different from the conventional two-photon (or multiphoton) absorption process in which, two or more low energy photons are absorbed simultaneously through its virtual metastable state. On the other hand, upconversion involves sequential absorption of NIR photons and makes use of the real, long-lived (μs to ms) intermediate states [7]. The presence of these real intermediate states in the upconversion process acts as photon reservoirs, and hence, the efficiency of the upconversion process is generally several orders of magnitude higher than that of two-photon absorption [8]. This unique advantage of upconversion enables the process to be realized by an inexpensive continuous wave (CW) diode laser instead of the much more expensive ultrafast pulsed (femtosecond) lasers [8]. Since this unique frequency upconversion does not exist in biomolecules, UCNPs are well suited for bio-applications in sensing, imaging, therapy and drug delivery [9,10]. In particular, the large anti-Stokes shift paves the way for considerable difference between excitation and emission wavelengths in the electromagnetic spectrum, which permits multiplexed sensing, and imaging [11].

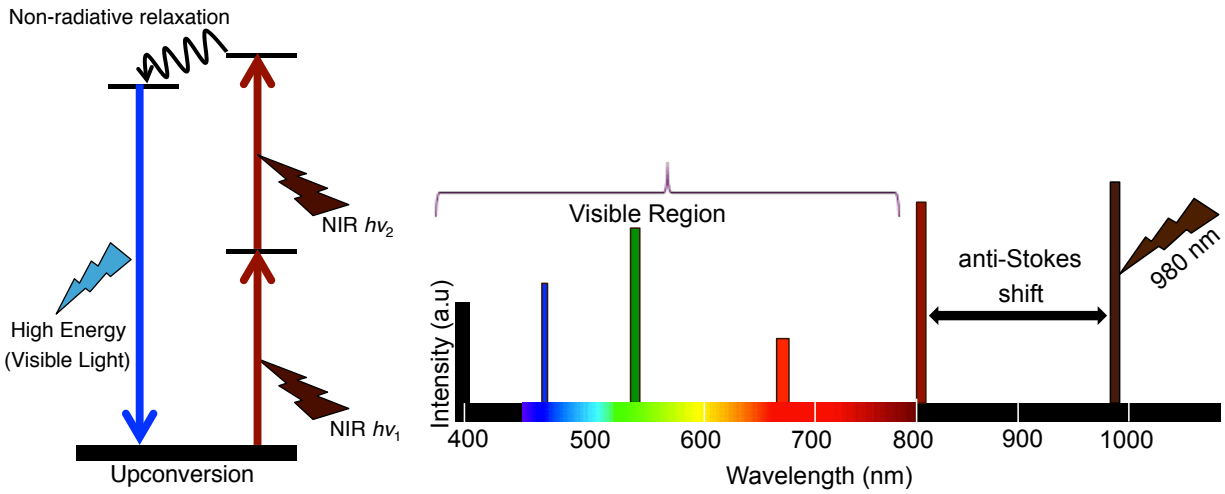

Figure 1.1 Fundamental upconversion mechanism and anti-Stokes shift following NIR excitation

Since the transition occurs within the 4*f* energy levels in the Ln^{3+}, the emission intensities are sharp and cannot be influenced by external factors. Hence, they are resistant to photo-bleaching [12] yielding stable luminescence and offer the advantage of being used for long-term repetitive and dynamic imaging [13]. Since the process of upconversion takes places following excitation with NIR wavelengths in the biologically transparent window, there is little to no background autofluorescence since the NIR excitation wavelength is specific only to the UCNPs. This allows for deep tissue penetration in biological tissues, less scattering and enhanced imaging capabilities [14].

1.1 Upconverting Nanoparticles (UCNPs)

UCNPs are considered as binary systems that contain a host crystal and optically active Ln^{3+} dopants with dimensions preferably less than 100 nm. The Ln^{3+} dopants are well dispersed within the host crystals and also at the surface [29]. Upon excitation at NIR wavelengths, the emission wavelength could range from the deep UV to visible to NIR. One of the intriguing facts about UCNPs is that they have similar optical properties as that of bulk materials due to their intra 4*f*-4*f* forbidden transitions, which are well protected from the outer 5*s* and 5*p* orbitals [15,16]. However, their luminescence efficiency is very low compared to that of bulk materials due to nanoscale induced surface defects. Due to the high surface area-to-volume ratio of UCNPs, most of the optically active emissive Ln^{3+} dopants are exposed to deleterious surface deactivation due to the presence of neighboring ligands and solvent molecules. The presence of

these impurities increases the phonon decay process and thus reduces upconversion luminescence efficiency [17]. The surface deactivation effect occurs in the following ways: (i) The presence of surface quenching centers located near the optically emissive dopants enhances the phonon energy loss; and (ii) random migration of energy from the optically active dopants which are located at the center of the UCNPs to their surface and subsequent energy loss [18]. In addition to the effect of host lattice, the concentration of Ln^{3+} dopants can also influence the upconversion efficiency. At higher concentration of emissive dopants, back energy transfer dominates which can lead to energy loss due to cross-relaxation process (to be discussed later in the thesis) and thus reduces upconversion efficiency [19]. Hence it has been a challenge to reduce the size of the nanocrystal and increase the luminescence efficiency. In order to achieve both, careful and judicious nanochemistry and surface engineering and functionalization of UCNPs are needed.

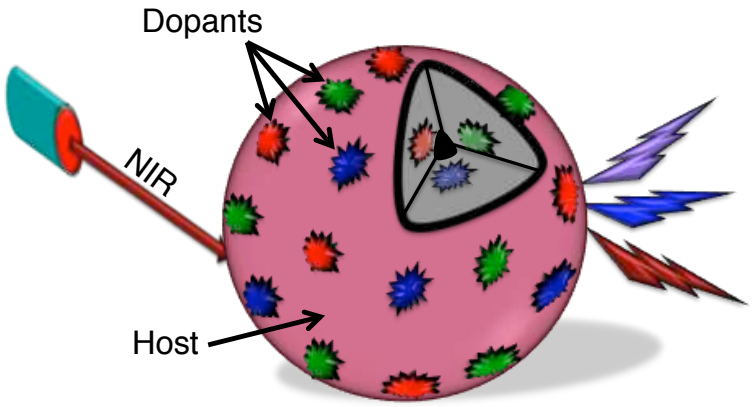

Figure 1.2 UCNP with host crystal and emissive dopants

1.1.1 Upconversion Host Crystal

Selection of a suitable upconversion host material is very crucial since they do influence the upconversion quantum yield and tuning of wavelength [20]. An ideal upconversion host material must be transparent in the wavelength range of interest, show high chemical stability, and should have high optical damage threshold. The host crystal would also have low lattice phonon energies in order to minimize non-radiative relaxation and thereby to enhance the upconversion luminescence [21]. Also, the host crystal should have minimum lattice mismatch with dopant ions. Among many reported host lattice crystals, alkali and alkaline earth metal-based host fluoride materials have

been employed extensively because of their low phonon energy, minimum lattice mismatch with dopants and stability towards moisture and optical transparency [22]. An extensive literature review reveals that hexagonal phase β-$NaYF_4$ is the most preferred host material over the cubic phase α-$NaYF_4$ due to stronger upconverted luminescence emission [23-25]. A significant advancement in reducing the size (less than 20 nm) of the UCNPs while simultaneously increasing upconversion intensity was reported by Yang. *et al*. for the Er^{3+} and Tm^{3+} doped $NaLuF_4$ host crystal [26]. Although multi-colored emissions were observed with various dopants in the β-$NaYF_4$ upconversion host, emission in the UV spectral range has been a challenge since it requires greater than three incident photons, which are less efficient than the two-photon visible emitting upconversion process. This was overcome by using $LiYF_4$ as the host crystal, which was reported by Mahalingam *et al*. [27]. In their work, the authors synthesized, Tm^{3+}/Yb^{3+} co-doped $LiYF_4$ by a thermal decomposition process. Their work resulted in the highly monodispersed hydrophobic UCNPs which was eventually made water dispersible through silica coating. In the present work, we have synthesized and used fluoride based host crystals such as $NaYF_4$ and $LiYF_4$ as the UV, visible and NIR emitting donor for biosensing, chemical sensing and the generation of ROS.

1.1.2 Upconversion Sensitizer

Ytterbium ion (Yb^{3+}) is the most widely used sensitizer for the upconversion process since the Yb^{3+} ion has a higher absorption cross section at the 980 nm NIR excitation wavelength [28]. Moreover, the Yb^{3+} ion has only one excited energy level and hence minimizes the non-radiative energy loss. The electronic energy level structure of Yb^{3+} is simple consisting of the ground state, $^2F_{7/2}$ and only one excited state, $^2F_{5/2}$. Since the sensitizer has only one excited state, changing its concentration will not cause any concentration related quenching (up to a certain point) [29]. High concentration of Yb^{3+} (greater than 18%) could help enhance the upconversion luminescence and has been reported along with Tm^{3+}, Er^{3+}, Ho^{3+} activator ions to achieve high upconversion luminescence [1].

1.1.3 Upconversion Activator

Tuning of upconversion luminescence requires judicious selection of activator/sensitizer combination. The Ln^{3+} dopant that emits the higher energy photon is known as the activator, and the most commonly used activator ions are erbium (Er^{3+}), holmium (Ho^{3+}) and thulium (Tm^{3+}) as dopants in host crystals due to their abundant, long-lived and ladder-like electronic energy states [29]. Heer *et al.* first reported efficient upconversion emission in colloidal Ln^{3+}-doped UCNPs [30]. They synthesized green emitting Yb^{3+}/Er^{3+} and blue emitting Yb^{3+}/Tm^{3+} co-doped $NaYF_4$ host UCNPs. Later, Boyer *et al*. reported on the synthesis of blue and green emitting, α-phase $NaYF_4$ UCNPs with similar dopant combination in a single, one-pot thermal decomposition method [31]. Other ions from the Ln^{3+} series have also been reported as activators for various applications [32]. In our work, we have focused only on the blue emitting Tm^{3+} activator doped in different host materials ($NaYF_4$ or $LiYF_4$). The UV/blue emission is of particular interest in our work because of the expected luminescence energy transfer to the appropriate acceptor for bio and chemical sensing as well as ROS generation.

1.2 Upconversion Mechanisms

The upconversion process has been extensively investigated in recent years and has been proved to be a valuable method for generating UV, visible, NIR emission upon lower energy NIR excitation. Upconversion is a non-linear optical process where two or more low energy photons are converted to higher energy emission, most commonly in the visible range. Since the emitted photons have energy higher than the excitation energy, this process has been defined as an anti-Stokes effect. Different upconversion luminescence mechanisms have been proposed. However, there are four fundamental upconversion mechanisms such as excited state absorption (ESA), energy transfer upconversion (ETU), photon avalanche (PA) and cross relaxation (CR). Also, energy migration mediated upconversion (EMU), a recent mechanism proposed for core/shell type nanoparticles has also been discussed.

1.2.1 Excited State Absorption (ESA)

Excited state absorption (also called sequential absorption) involves sequential absorption of two photons (Figure 1.3a). The mechanism was first proposed by Bloembergen [33]. ESA is a single ion process and takes place in materials with low Ln^{3+} dopant concentration. In the first step, a photon is absorbed to promote the ion from the ground state (GS) to its first excited state also known as the metastable state (ES1). This step is known as ground state absorption (GSA). In the next step, another photon is absorbed to excite the ion from the intermediate state to its ES2 level. Subsequently, the excited ion radiatively relaxes back to the ground state by emitting a higher energy photon.

1.2.2 Cross Relaxation (CR)

This energy transfer process typically results from the ion-ion interaction between two identical Ln^{3+} dopants. In this process, two neighboring Ln^{3+} ions ($Ln^{3+}(1)$ and $Ln^{3+}(2)$) are simultaneously excited to their first intermediate state by the incoming NIR photons. Subsequently, one of the Ln^{3+} ions, $Ln^{3+}(1)$, transfers its energy to the second Ln^{3+} ion, $Ln^{3+}(2)$ promoting $Ln^{3+}(1)$ from the first intermediate state (ES1) to the second intermediate state (ES2). $Ln^{3+}(2)$ then returns to the ground state (GS) (Figure 1.3b). The efficiency of the cross relaxation process depends on the dopant concentration and usually occurs in more heavily doped single ion systems. However, very high concentrations can result in back energy transfer and lead to vibrational decay, which results in the quenching of the upconversion luminescence.

1.2.3 Energy Transfer Upconversion (ETU)

Among all the upconversion processes, energy transfer upconversion (ETU) is the most efficient in Ln^{3+}-doped UCNPs and was first reported by Auzel [34]. Typically, two different Ln^{3+} ions (sensitizer and activator) are involved in the ETU process. In a typical ETU process, the sensitizer ion accepts the incident low energy photons in its ground state (GSA) thereby promoting it to the upper excited level. Subsequently, the sensitizer ion in the excited state transfers its energy to a neighboring Ln^{3+} ion in its proximity (the activator) promoting it from the ground state to its first intermediate excited state (Figure 1.3c). A second energy transfer from another sensitizer nearby promotes the activator

to the upper excited state. This is the most common mechanism in co-doped systems such as Er^{3+}/Yb^{3+}, Tm^{3+}/Yb^{3+}, and Ho^{3+}/Yb^{3+} [29].

1.2.4 Photon Avalanche (PA)

Photon Avalanche (PA), sometimes called absorption avalanche, was first discovered by Chivian *et al*. and it has been considered as a more advanced and efficient upconversion process, although it is more rarely observed [35]. A two-ion system is demonstrated in Figure 1.3d. $Ln^{3+}(2)$ is involved in a weak ground state (non-resonant) absorption process exciting the ion to the first excited state (ES1). Low energy NIR light is also absorbed by $Ln^{3+}(1)$ and promoting it to the first excited level ES1. Subsequent energy transfer from the ES1 level of $Ln^{3+}(1)$ to the ES1 state of $Ln^{3+}(2)$ populates this level. This population promotes $Ln^{3+}(2)$ from energy level ES1 to ES2. This is followed by cross relaxation between ES2 of $Ln^{3+}(2)$ and ES1 of $Ln^{3+}(1)$. In the next steps, energy transfer from ES1 of $Ln^{3+}(1)$ to the ES1 level of $Ln^{3+}(2)$ populates this level and again promoting $Ln^{3+}(2)$ to its ES2 level. This creates a looping process and exponentially increases the populations of the ES2 level of $Ln^{3+}(2)$ and hence enhances the upconversion emission to a great extent thus leading to an avalanche process [36].

1.2.5 Energy Migration Mediated Upconversion (EMU)

Energy migration mediated upconversion is usually observed in core-shell type UCNPs. There are four types of Ln^{3+} dopants employed such as the usual sensitizer, accumulator, migrator and activator (Figure 1.3e). The Ln^{3+} sensitizer dopant is used to collect the low energy NIR photons and transfers its energy to the adjacent accumulator ion at its ES1 level. Subsequent energy transfers promote the ion to its ES2 level. The role of the migrator ion is to receive the energy from the accumulator ion at its ES2 and transfer it through its sub-lattice and finally to the activator ion. All these energy transfers occur at their respective excited states only. The location of sensitizer/accumulator and accumulator/activator are controlled in such a way in the core/shell structure to reduce the energy loss by adverse cross relaxation process. The efficiency of EMU could be increased by a range of migrator ions through its core/shell structure to facilitate the energy transfer from the accumulator to the activator. An important aspect of EMU in the core/shell structure is that the excitation energy

acquired by the sensitizer can be transferred and stored in the accumulator which in turn transfers its energy in a step-wise manner to the adjacent migrator ion. The migrator ions carry this throughout the core/shell structure and finally to the activator ion. The process amasses the energy, and when the excited ion relaxes back from its ES2 level to the ground state, it emits higher energy photons. The core/shell composite structure offers the advantage of changing the concentration of the activator dopant at the same time minimizes the upconversion quenching. Hence, tunable upconversion luminescence can be achieved even for activators with short-lived intermediate states [37].

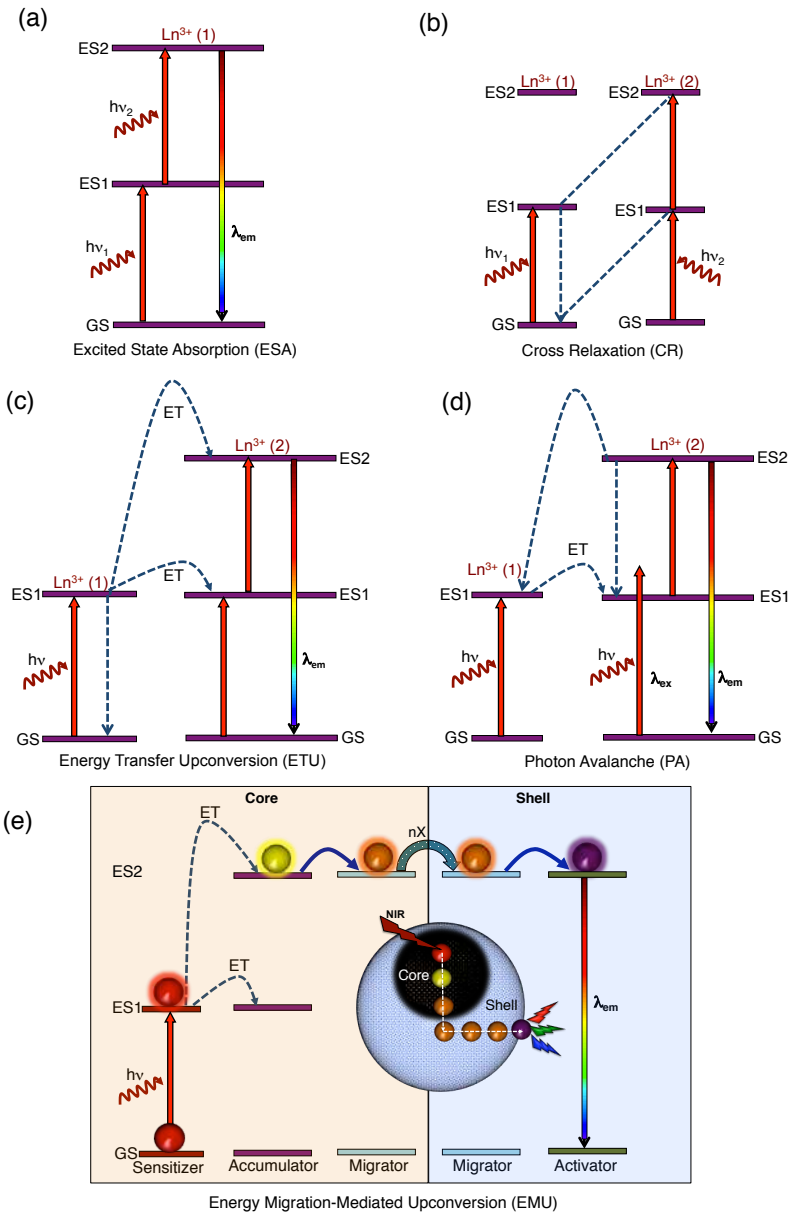

Figure 1.3. Schematic of upconversion luminescence mechanisms. a) Excited-State Absorption (ESA), b) Cross Relaxation (CR), c) Energy Transfer Upconversion (ETU), d) Photon Avalanche (PA), and e) Energy Migration Mediated Upconversion (EMU). GS, ES1, and ES2 represent ground state, intermediate state, and excited state, respectively. GS, ES, ET denote ground state, excited state and energy transfer, respectively.

1.3 General Synthetic Methods for Upconverting Nanoparticles

There have been different chemical methods used for the synthesis of UCNPs including co-precipitation, hydrothermal (solvothermal), sol-gel, and thermal decomposition.

1.3.1 Co-Precipitation Method

The co-precipitation synthetic method offers several advantages such as, simple operating procedure, fast synthesis, and mild reaction conditions. In addition, this method does not require any expensive laboratory setup [38]. Moreover, the size of the UCNPs can be readily controlled by using suitable surface ligands such as polyethyleneimine (PEI) [39], polyvinylpyrrolidone (PVP) [40], and by a strong hexadentate ligand, such as ethylenediaminetetraacetic acid (EDTA) [41] in the reaction mixture. Despite all these advantages, in some situations, the synthesis requires post heat treatment [42,43]. Moreover, the synthesis usually results in the formation of less efficient α-phase UCNPs. Since β-phase UCNPs have higher upconversion efficiency [44], it is imperative that calcination becomes necessary in order to obtain the β-phase. However, calcination can only be carried out at higher temperature and this poses a major problem for laboratory conditions [45].

1.3.2 Hydrothermal (Solvothermal) Method

The hydrothermal (solvothermal) method has been used to synthesize both α-phase and β-phase UCNPs. In this method the solubility of precursor materials can be increased under the hydrothermal or solvothermal conditions, which effectively increases the rate of the reaction [46-48]. This method produces UCNPs with excellent crystallinity, tunable size, and crystal morphology by controlling the reaction temperature, time, precursor concentration, as well as pH value [49-52]. In addition, this is a one-pot synthetic process and surface capping ligands can be used along with other precursors in a single reaction vessel [53,54]. Another distinct advantage is that

no post heat treatment is required. Like any other method, the hydrothermal (solvothermal) method has a few drawbacks; requirement of specialized reaction container (autoclave) and manipulation of the reactions under a set of reaction temperature as well as pressure conditions over a long period of time. In most of these reactions, water is a major solvent however in some situations other hydrophilic solvents could be used in order to improve the solubility of the precursor materials. Such reactions are known as solvothermal synthesis [55].

1.3.3 Sol-Gel Method

The sol-gel method is a typical wet-chemical process generally used for the synthesis of UCNPs. This method is distinct in the sense that the synthesis has been carried out by hydrolysis and polycondensation of metal alkoxide precursors and the nanoparticle growth is feasible in reverse micelle emulsions. Over the years, this method was extended to the synthesis of various UCNPs with mixed metal oxides such as Er^{3+}-doped TiO_2, ZrO_2, $BaTiO_3$, and YVO_4 [56-58]. Sivakumar *et al*. produced white light upconversion as well as red and green following NIR excitation using sol-gel based Ln^{3+}-doped UCNPs [59,60]. However, in spite of all these advantages, the nanoparticles synthesized by the sol-gel method find little or no applications in the development of biological assays due to particle aggregation and production of polydispersed nanoparticles [29].

1.3.4 Thermal Decomposition Method

The thermal decomposition method is by far the best method for the controlled synthesis of highly monodispersed and precisely defined UCNPs [27,31,61-65]. In this method, metal trifluoroacetate (TFA) precursors are dispersed in a high boiling, non-coordinating solvent such as octadecene and with a suitable capping ligand such as oleic acid, oleylamine, or trioctylphosphine (at temperatures between 250 °C and 330 °C. The presence of capping ligand/surfactant helps control the growth of the UCNPs in the solution mixture. Due to the high temperature and the sensitivity of UCNPs towards oxygen impurities, control over the reaction must be precise in order to produce good-quality monodispersed nanoparticles. Other factors such as pressure, capping ligand, precursor concentration and composition, rate of heating and cooling, reaction time,

solvent and reagent concentrations also play an important role in the crystalline size and morphology [66]. Since this method uses the air sensitive TFA precursors, toxic fluorinated and oxyfluorinated compounds are released as byproducts during the reaction hence this synthesis must be carried out in a well-ventilated fume hood. In addition, this method produces UCNPs, which are hydrophobic (oleate-capped) and hence further surface modification is required in order to make them water dispersible for biological applications [27].

1.4. Surface Modification of UCNPs

For targeted biological applications it is imperative that the synthesized UCNPs can be dispersed in aqueous media and bear specific functional groups amenable to biomolecules at their surface [67]. Hence, surface functionalization of UCNPs is needed for immunoassay [68-70], imaging [71-77], DNA encoding [78], cancer therapeutic [79-82] and biosensing [83-86] applications. In order to make the UCNPs water-dispersible and apply them successfully in biomedical research, suitable surface functionalization and bioconjugation chemistries are prerequisites. [87-89]

1.4.1 Surface Modification Strategies

Over the years, many different strategies have been developed to convert hydrophobic UCNPs into more water dispersible hydrophilic particles [90]. These strategies could be divided into four categories: (1) chemical modification of the hydrophobic surface ligand such as oleic acid and oleylamine (2) coating with dual layer molecules such as amphiphilic reagent and polymers, (3) formation of an additional layer on the surface of UCNPs (4) complete displacement of the original native hydrophobic ligand followed by the addition of hydrophilic ligand. These strategies will be discussed briefly in the following sections.

(i) Modification of the Capping Ligand

In this method, the hydrophobic molecule present on the surface of the UCNPs could be altered/modified by using a suitable reagent, however, it has been infrequently used. The carbon-carbon double bond present in the oleic acid or oleylamine capping ligands could be oxidized to form hydrophilic carboxyl or epoxy functional groups using

oxidizing agents such as the Lemieux-Von Rudloff reagent [91]. Other reagents such as ozone [92] and 3-chloroperoxybenzoic acid [93] have also been used to oxidize the surface ligand to incorporate appropriate functional groups that facilitate water dispersibility. Upon modification, these UCNPs could be attached to cancer drugs such as doxorubicin (DOX) to enable controlled drug delivery applications [94].

(ii) Coating with Amphiphilic Reagents

This method involves coating of the hydrophobic UCNPs with long alkyl chain molecules to form a dual layer at its surface. This layer is stabilized by Van-der-Waals attractive forces between the hydrophobic oleate moiety and the hydrophobic end of the amphiphilic reagent [95,96]. There are a few advantages of using amphiphilic molecules such as they (a) show strong Van-der-Waals interaction, (b) offer facile modification of surface charge, and (c) offer multiple layer formation thus protecting the UCNP surface from possible quenching effects. The attraction at the hydrophobic end results in the availability of hydrophilic functional groups directed outward and leads to the formation of a bilayer at the surface of the UCNPs making them well dispersible in water or any buffer solution for further bioconjugation. Another important class of amphiphilic reagent that is used to modify the surface of nanoparticles is the phospholipids. Phospholipid modified UCNPs could be promptly absorbed or internalized by cells [97] henceforth used for imaging purposes. For drug delivery applications, phospholipids have been widely used. Recently, Huang *et al*. developed green emitting UCNPs encapsulated in liposomes and loaded with DOX as a hybrid nanocomposite for drug delivery following 980 nm NIR excitation [98]. Different phospholipids such as maleimide or biotin are readily available commercially and their size could be engineered with different chain lengths or modified by adding poly(ethyleneglycol) (PEG) molecules, since PEG offers high biocompatibility [99,100]. In addition to UCNPs, other nanoparticles such as metal plasmonic AuNPs, quantum dots, or superparamagnetic iron oxide nanoparticles (SPIONs) have also been modified with amphiphilic polymers [101]. Other polymers such as poly(acrylic acid) with long alkyl chains could also be attached to the surface of hydrophobic oleate-capped UCNPs [102,103]. This endows negative charges on the surface of UCNPs due to the availability of carboxylic acid functional groups at neutral pH and thus will make the nanoparticles water dispersible. The PEG functional group

could also help conjugate the nanoparticles to diverse biomolecules [104]. Reports also show that UCNPs may be coated with amphiphilic chitosan in light triggered drug delivery application such as photodynamic therapy [105].

(iii) Silica Encapsulation (Shell Formation)

Hydrophobic UCNPs can be made water dispersible (hydrophilic) by forming a thin layer of shell on their surface. Silica (SiO_2) is the most commonly used shell material for this purpose. The formation of a SiO_2 shell on the surface of UCNPs is a useful method to bring in different functionalities as well as making them water or buffer dispersible. Strategies such as the Stöber method or the reverse microemulsion method have been used for uniform shell formation. In the Stöber method, the nanoparticles were directly coated with SiO_2 through a seeded polymerization technique using the tetraethyl orthosilicate (TEOS) precursor without the use of any stabilizer [106]. However, in the reverse microemulsion method, a surfactant known as Igepal CO-520 is widely used since it forms fairly stable reverse microemulsions for polymerization of the TEOS [107]. During the synthesis, ammonia is used as a catalyst since it causes the formation of silicic acid at a concentration above the nucleation concentration ensuring a steady growth of the SiO_2 shell on the surface of the UCNPs [108,109]. In spite of the many advantages of SiO_2 coating strategy, it does have a few disadvantages; SiO_2 coated UCNPs might lead to polydispersity and necking, which is undesirable for bioapplications. Incomplete formation of silica shell will be hard to predict and additionally they tend to aggregate quickly.

(iv) Replacement of the Capping Ligand

Ligand replacement or substitution is another important strategy for surface modification of UCNPs. This can be achieved by two methods. The first is the direct (or single step) replacement of the capping ligand and second is a two-step process in which, first the capping ligand is completely removed from the surface of the UCNPs followed by attachment of the new hydrophilic ligand on its surface.

(a) Single Step Replacement of Capping Ligand

In this single-step method, the capping hydrophobic organic ligand on the surface of the UCNPs is completely replaced by the incoming more polar ligand, which gives the UCNPs water dispersibility. The advantage of this method is that the process is fast and multiple functional groups could be made available at the surface. In a typical procedure, the UCNPs with its capping ligand (in most cases oleic acid) and the new ligand are stirred at a suitable temperature followed by multiple washings. The resultant hydrophilic nanoparticles could be dispersed either in water or in a buffer solution [110]. However, the main disadvantage is particle aggregation, and frequent sonication is required before suitable bioapplications [111].

(b) Two-Step Replacement of Capping Ligand

Bogdon *et al*. [112] have developed a method that involves the reaction of oleate-capped hydrophobic UCNPs with hydrochloric acid. This reaction with a strong acid, HCl, strips the surface capping ligand, leaving naked UCNPs making them water or buffer solution-dispersible. In the next step, the bare UCNPs were coated with suitable ligands for targeted applications.

CHAPTER 2 – APPLICATIONS OF UPCONVERTING NANOPARTICLES

2.1 Biosensing

Sensing is an analytical process, in which a target compound/analyte is being detected by means of a detectable change in the signal produced. Based on the signal obtained the sensing mechanism can further be classified as optical, electrical, mass, thermal, magnetic and pressure (Figure 2.1). In all of these sensing principles, the pool containing the target analyte is subjected to a molecular recognition event in which the analyte will aptly bind to a suitable receptor. This binding event produces a measurable change in the signal. The change in the signal is further processed and displayed on a display unit [113,114]. Based on the type of target analyte/compound the sensors can broadly be classified as biosensor and chemical sensor. If the target analyte is biological in nature, then the sensor is known as a biosensor. On the other hand, if the analyte is chemical in nature then it is called a chemical sensor.

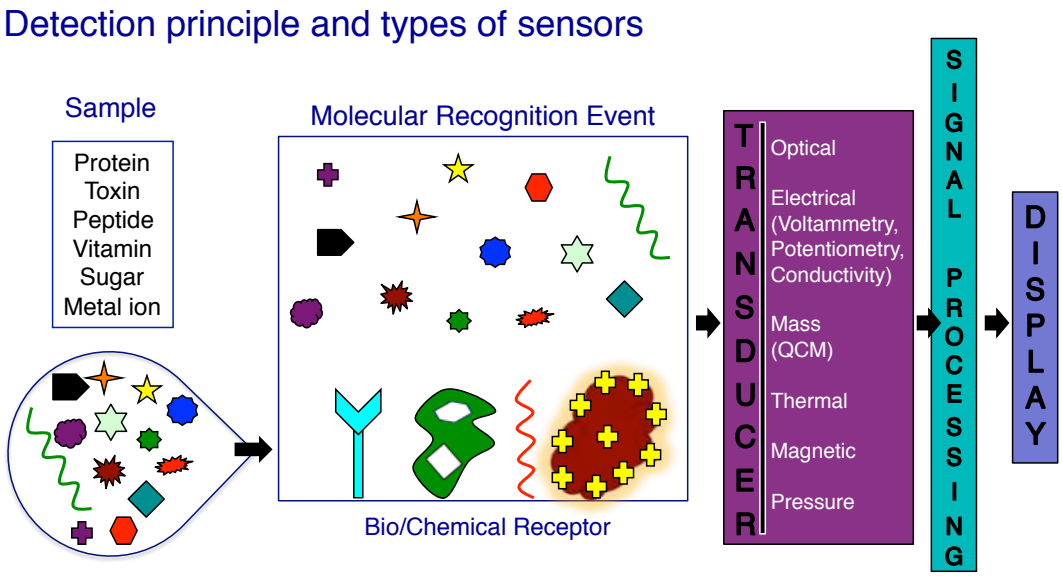

Figure 2.1 Basic principle and types of a sensor showing different components

The International Union of Pure and Applied Chemistry (IUPAC) defines the biosensor as a self-contained integrated receptor-transducer device that is capable of providing selective, quantitative or semi-quantitative analytical information using a biological recognition element [113]. Although biosensor development has been very rapid in

recent times, the significant challenge is the sensitive and selective signal production due to the biological recognition event (transduction) of the target analyte at the lowest concentrations [114].

2.1.1 DNA Biosensing

Recently, DNA biosensors that are based on the hybridization of nucleic acids have gained much interest [115,116]. To realize high sensitivity and selectivity, it is imperative that the DNA biosensors should be more robust. Recently efforts have been made to develop new DNA biosensors that use nanoparticles [117-119]. Using nanoparticles for DNA biosensor brings new advantages to this field. Firstly, since the biosensor depends on the size of the nanoparticles, more atoms are exposed as the size is reduced because of increased surface area. This enhances the available binding sites on the nanoparticle surface thus increasing the sensitivity many folds. Different types of nanoparticles have been employed in DNA biosensors including metal nanoparticles, such as gold or silver [118-120], semiconductor inorganic quantum dots [121-123] or carbon dots [124]. Although most of these nanoparticles are good candidates for DNA biosensing applications, inorganic semiconductor quantum dots possess inherent toxicity since most of the commonly used quantum dots contain toxic heavy metals thus limiting their applications in biological sciences. Also, they have blinking effects, which affects their application in long-term repetitive imaging. Most importantly, in many cases, inorganic quantum dots and carbon dots are excited under high energy UV light, which has limited penetration depths and increased scattering thereby reducing their sensitivity [125]. One of the most common mechanisms involved in nanoparticle-based sensing relies on the fluorescence resonance energy transfer (FRET) between the donor and acceptor. Use of FRET-based nanoparticles for sensing can have some drawbacks that must be taken into careful consideration such as inefficient energy transfer, uncertainty in the relative orientation of the donor-acceptor pair either before or after hybridization (Figure 2.2), reduced lifetime of the fluorophore, large background signals arising from the biological samples, and the requirement of labeling [126].

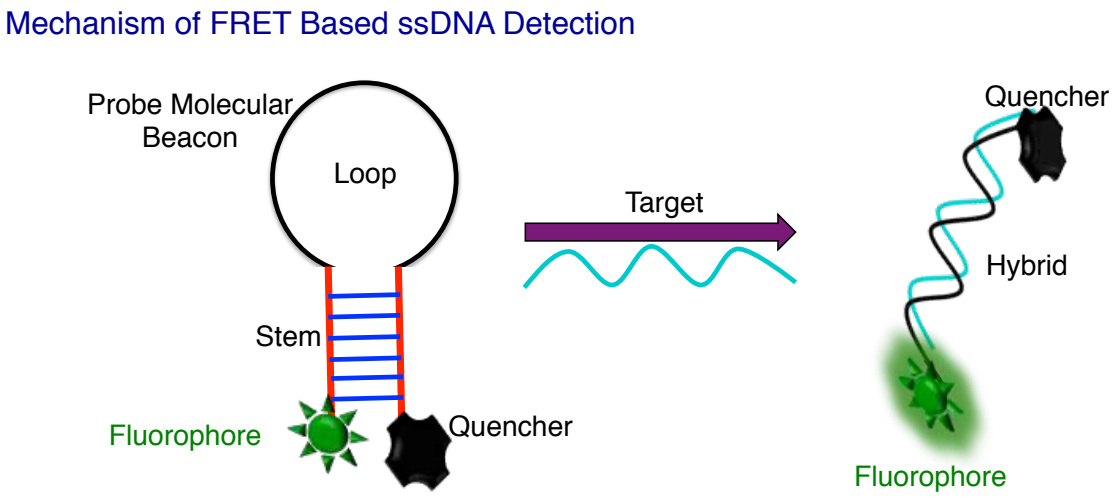

Figure 2.2 Mechanism for the detection of ssDNA target based on Fluorescence Resonance Energy Transfer (FRET).

In order to overcome some these undesirable properties, Ln^{3+} based UCNPs are beginning to gain attention in the field of biosensing. In our work, we intended to develop a new DNA nanobiosensor that uses, Ln^{3+} based UCNPs (see Chapter 3). Since these UCNPs could be excited at the biologically transparent near-infrared wavelength (980 nm), drawbacks such as background autofluorescence and scattering could be avoided. In addition, these UCNPs do not show any blinking, they have high chemical stability, reduced toxicity and the sharp emission wavelengths resulting from the intra 4*f*-4*f* transition could be effectively used in multiplexed detection of many target analytes [127].

2.2 Chemical Sensing

A chemical sensor, or a chemosensor, is a responsive material or a compound that shows an observable change in its physical property such as electrical, electronic, magnetic, or optical signal when it comes in contact with a target chemical analyte. Among many other sensors, fluorescent chemosensors offer significant advantages owing to their ease of development, sensitivity, and specificity and also, their response time can be easily monitored [128]. Heavy metal ions are considered as environmental pollutants, and due to their toxic nature, receptors that are capable of detecting a particular heavy metal ion in a complex mixture is of significant interest [129]. Furthermore, they also have potential implications in biological and living systems [130−132].

2.2.1 Cu^{2+} Chemical Sensing

Among all the heavy metal ions, Cu^{2+} ion has been a very special element since it plays a pivotal role in the human body and also in other living organisms [133,134]. Although Cu^{2+} plays an important role in human health, its presence in higher concentrations may cause serious health issues such as Alzheimer and Parkinson diseases [135-137] Additionally, Cu^{2+} is one of the most versatile heavy elements that is found in drinking water in many developing and developed countries. Hence, the detection of Cu^{2+} ions in the presence of other metal ions and impurities is of significant importance. Developing a suitable sensitive as well as selective material for Cu^{2+} detection has been a challenge. Research has been carried out to develop sensors for Cu^{2+} based on fluorescence methods [138-140]. Thus far, most of the reported sensors for Cu^{2+} use water-insoluble organic dye molecules, which are not suitable for detection in real biological samples and also in limited resource environment. Recently there has been an increase in interest to develop nanoparticle-based Cu^{2+} detection with high sensitivity and selectivity [141-143]. Most of the nanosensors are based on ligand functionalization of metal plasmonic nanoparticles such as silver, gold, quantum dots, carbon dots as well as polymer-based nanoparticles [144-152]. Although these nanoparticles have advantages of their own, they suffer from broad absorption and emission wavelengths, size, and shape dependent optical properties, which could alter the limit of detection (LOD) in the nanoparticle solution if polydispersed [153,154]. Use of toxic quantum dots with heavy metal ions either in its core or shell could compromise the sensing of the target metal ion analyte due to leaching effects. All these limitations have significantly hampered the development of practical nanosensors for Cu^{2+} detection. Henceforth, NIR based chemosensors have gained much attention to overcome all these deleterious effects. In one of the methods for the detection of Cu^{2+}, Zhang *et al.* [155] used green emitting Yb^{3+}/Er^{3+} co-doped $NaYF_4$ UCNPs as the energy donor following NIR excitation and an organic dye, rhodamine B hydrazide, as the acceptor through fluorescence resonance energy transfer. As mentioned previously, the reported organic dye used in this work has limited or no solubility in aqueous media hence affecting its LOD and makes the method not easily reproducible. In order to overcome all these limitations, in this thesis, we have successfully synthesized, characterized and proven

that the nanohybrid system composed of the highly biocompatible, natural product curcumin functionalized on the surface of UV to NIR emitting $LiYF_4$:Tm^{3+}, Yb^{3+} UCNPs can be used for sensitive detection of Cu^{2+} at NIR wavelengths following NIR excitation. The use of NIR as the detection wavelength increases its sensitivity and selectivity since most of the other metal ions, including toxic metal ions, do not absorb in the NIR region except for Cu^{2+} (see Chapter 4).

2.3 Reactive Oxygen Species

The term reactive oxygen species (ROS) is used to denote any molecular species or an ion derived from molecular oxygen with a free radical intermediate. Free radicals are species with a single or unpaired electron. The ground state of molecular oxygen has two single unpaired electrons (also called bi-radical) in its outermost orbital. Since these two electrons have the same spin in its ground state (triplet state), they remain stable and not reactive. In a situation where if one of the two single (odd) electrons gets excited to the upper energy level, which results in the electron having opposite spin then the resulting molecular oxygen species becomes highly reactive, called a singlet oxygen species [156]. Gerschman *et al.* suggested that molecular oxygen species with free radicals could have toxic effects for aerobic organisms [157]. Over the decades, the terms reactive oxygen species (ROS), reactive oxygen intermediates (ROI) and reactive nitrogen species (RNS) have been used to define any molecular species with different reactive intermediates. In general, these reactive species are endogenous and highly reactive molecules having either oxygen or nitrogen with an unpaired electron. When molecular oxygen species undergoes incomplete reduction, it could produce the superoxide radical anion ($O_2^{\cdot -}$) and hydroxyl radicals ($OH^{\cdot}$). The term ROS includes both reactive oxygen intermediate and also (O_3) and singlet oxygen ($^*{}^1O_2$) [158]. Sometimes the ROS defines species with more than one oxygen atom and includes the peroxy ($ROO^{\cdot}$), alkoxy ($RO^{\cdot}$), semiquinone anion ($SQ^{\cdot -}$) and carbonate anion ($CO_3^{\cdot -}$) radicals [159]. Research has concluded that ROS such as hydroxyl and peroxy radicals are responsible for oxidative damage to biomolecules such as DNA, fatty acids and many other cellular components [160] and overproduction of ROS is the major reason for many disorders [161]. The combined effect of ROS over production and reduced

antioxidant defenses is the cause of diseases such as cancer, cardiovascular, inflammatory, and neurological disorders such as such as Alzheimer and Parkinson's diseases [162-165]. For normal biological functions, ROS are essential to life in a normal cellular environment. In the field of biomedical research, development of new sensitive tools for the generation of ROS is in great demand. However, due to highly reactive nature and a short life-time of ROS pose a great challenge for applications in biomedical science. Among all the advantages of ROS, the most significant application is in its use in the field of photodynamic therapy (PDT) for cancer.

2.3.1 Generation of ROS at NIR Excitation

PDT is an emerging therapeutic modality for the treatment of both malignant and non-malignant cancer cells. Fundamentally there are two steps involved in the PDT treatment, first, a photosensitizing agent will be administered to the patient [166-168], and then the photosensitizer (drug) will be activated by light of specific wavelength [169,170]. Thus far, most of the reported photosensitizers are based on organic dye molecules, macrocyclic compounds such as porphyrins, phthalocyanines, and pyrrole based cyclic compounds [171-173]. These macrocyclic organic compounds show absorption in the visible red region of the electromagnetic spectrum and thus allowing deeper penetration depths for cancer therapeutic applications. These cyclic photosensitizers also show enhanced efficiency and photostability for PDT applications [174,175]. For cancer therapeutics, PDT has gained increased attention due to its cancer cell targeted applications. Since PDT uses light and light has directional property, the photosensitizers could be concentrated on the tumor cell through active or passive targeting methods [176]. Recently there has been an increase in interest in the use of transition metal complexes as probes and imaging reagents owing to their high photoluminescence property, tunable emission and cellular uptake [177,178]. However, there have been few disadvantages in using transition metal complexes that limit their biological applications such as their high cytotoxic nature and insignificant solubility in aqueous media [177,178]. To overcome the solubility problem, we have proposed to synthesize a highly photoluminescent, red emitting and water-soluble Ir complex with two polar carboxylic acid (-COOH) functional groups. The presence of –COOH makes

the Ir complex soluble in polar solvents such as water and ethanol. When it comes to the photo-triggered release of these Ir complexes, unfortunately, the absorption spectrum of Ir complexes is mainly located in the UV to visible region of the spectrum [179]. Since the penetration of UV and visible light is very small in the tissue region, the biological applications of Ir complexes, especially in PDT has not been explored significantly. One major strategy to overcome this problem is to use NIR wavelength in the region between 700 and 1100 nm since biological tissues are silent in this region [180-185]. Hence, we envisaged to use NIR excitable Ln^{3+}-doped UCNPs as delivery vehicles (nanocarriers) loaded with Ir complex for application in PDT. This nanohybrid material has the potential to overcome the solubility problem of the Ir complex photosensitizer since our Ir complex showed enhanced solubility in polar solvent such as water and also by attaching them to the UCNPs (see Chapter 5).

2.3.2 Generation of ROS with UV Excitation

In recent years, the use of superparamagnetic iron oxide nanoparticles (SPIONs) has gained increased attention in the field of biomedical science [186-188]. Multi-functional properties could be integrated by adding some additional applications onto a single SPION such as drugs, a targeting ligand and also by adding phototunable fluorophores for optical imaging or radionuclides for positron emission tomography (PET) imaging [189]. The nanocrystalline size, shape and its magnetism behavior could also be engineered to extract a targeted property from the SPION [190,191]. Although the field of PDT is less invasive and more preferred method for targeted cancer therapeutic applications, this technique still suffers from the lack of proper delivery systems for the photosensitizers to realize more effective PDT treatment. Tada *et al.* first reported the application of a dye (methylene blue) loaded silica coated SPIONs for PDT [192]. Loading of the photosensitizer into the silica matrix did not improve the efficiency of the singlet oxygen (ROS) generation, and this was attributed to the increased scattering from the SPIONs. Later, Lai *et al*. [193] synthesized an Ir complex loaded SPIONs and successfully generated ROS. A tri-modal nanoprobe was achieved by this nanohybrid material such as MRI from the SPIONs, photoluminescence from the Ir complex and ROS generation by excitation at UV for PDT [193]. However, in their method, the

synthesized Ir complex was hydrophobic in nature and hence effective ROS generation could not be achieved. In our work, we envisaged the use of hydrophilic Ir complex integrated into the silica matrix along with the SPIONs core thereby enhancing the overall beneficial effects of this tri-modal nanoprobe. In this thesis, the ROS generation by the Ir complex is also investigated and confirmed by forming an SPION/Ir complex nanocomposite under direct UV excitation (see Chapter 6).

2.4 References

1. Auzel, F. Upconversion and anti-stokes processes with f and d ions in solids. *Chem. Rev.* **2004**, *104*, 139-174.

2. Judd, B. R. Optical absorption Intensities of rare-earth ions. *Phys. Rev*. **1962**, *127*, 750-761.

3. Ofelt, G. S. Intensities of crystal spectra of rare-earth ions. *J. Chem. Phys*. **1962**, *37*, 511-520.

4. Vetrone, F.; Boyer, J. C.; Capobianco, J. A.; Speghini, A.; Bettinelli, M. Effect of Yb^{3+} codoping on the upconversion emission in nanocrystalline Y_2O_3:Er^{3+} *J. Phys. Chem. B* **2003,** *107*, 1107-1112.

5. Sivakumar, S.; Diamente, P. R.; Van Veggel, F. C. J. M. Silica-coated Ln^{3+}-doped LaF_3 nanoparticles as robust down and upconverting biolabels. *Chem. Eur. J.* **2006,** *12*, 5878-5884.

6. Binnemans, K.; Van Deun, R.; Görller-Walrand, C.; Adam, J. L., Spectroscopic properties of trivalent lanthanide ions in fluorophosphate glasses. *J. Non-Cryst. Solids* **1998,** *238*, 11-29.

7. Changqing, Y.; Liwei, Z.; Xiaomei, W.; Zuoqin, L. Photon upconversion: from two-photon absorption (TPA) to triplet–triplet annihilation (TTA) *Phys. Chem. Chem. Phys.* **2016**, *18*, 10818-10835.

8. Hans, U. G.; Markus, P. Near-infrared to visible photon upconversion processes in lanthanide doped chloride, bromide and iodide lattices. *J. Alloys Compd*. **2000**, *303–304*, 307–315.

9. Achatz, D. E.; Ali, R.; Wolfbeis, O. S. Luminescent chemical sensing, biosensing, and screening using upconverting nanoparticles. *Top. Curr. Chem*. **2011**, *300*, 29–50.

10. Wang, F.; Banerjee, D.; Liu, Y. S.; Chen, X. Y.; Liu, X. G. Upconversion nanoparticles in biological labeling, imaging, and therapy. *Analyst* **2010**, *135*, 1839–1854.

11. Heike, S. M.; Peter, K.; Sayed, M. S.; Otto, S. W. Upconverting luminescent nanoparticles for use in bioconjugation and bioimaging. *Curr. Opin. Chem. Biol*. **2010**, *14*, 582-596.

12. Nguyen, P. D.; Son, S.J.; Min, J. Upconversion nanoparticles in bioassays, optical imaging and therapy. *J. Nanosci. Nanotechnol*. **2014**, *14*, 157-174.

13. Qiuqiang, Z.; Baoju, W.; Xuanyuan, W.; Sailing, H. Controlling the excitation of upconverting luminescence for biomedical theranostics: neodymium sensitizing. *Opt. Mater. Express* **2016**, *6*, 1011-1023.

14. Xiaomin, L.; Fan Z.; Dongyuan Z. Highly efficient lanthanide upconverting nanoparticles: Progresses and challenges. *Nano Today* **2013**, *6*, 643–676.

15. Suyver, J. F.; Grimm, J.; Van V. M. K.; Biner, D.; Kramer, K. W.; Gudel, H. U. Upconversion spectroscopy and properties of $NaYF_4$ doped with Er^{3+}, Tm^{3+} and/or Yb^{3+}. *J. Lumin*. **2006,** *117*, 1-12.

16. Shan, J.; Chen, J.; Meng, J.; Collins, J.; Soboyejo, W.; Friedberg, J. S.; Ju,Y. Biofunctionalization, cytotoxicity, and cell uptake of lanthanide doped hydrophobically ligated $NaYF_4$ upconversion nanophosphors. *J. Appl. Phys*. **2008,** *104*, 094308-7.

17. Arppe, R.; Hyppanen, I.; Perala, N.; Peltomaa, R.; Kaiser, M.; Wurth, C.; Christ, S.; Resch- Genger, U.; Schaferling, M.; Soukka, T. Quenching of the upconversion luminescence of $NaYF_4$:Yb^{3+},Er^{3+} and $NaYF_4$:Yb^{3+},Tm^{3+} nanophosphors by water: the role of the sensitizer Yb^{3+} in non-radiative relaxation. *Nanoscale* **2015**, *7*, 11746-11757.

18. Feng, W.; Juan, W.; Xiaogang, L. Direct evidence of a surface quenching effect on size dependent luminescence of upconversion nanoparticles. *Angew. Chem. Int. Ed*. **2010**, *49*, 7456–7460.

19. Wang, C.; Meng, Q. The size confinement effect for Ln^{3+} (Ln = Tm or Eu) concentration quenching and energy transfer in Y_2O_3 nanocrystals. *J. Nanosci. Nanotechnol*. **2014**,*14*, 3893-3897.

20. Mai, H. X.; Zhang, Y. W.; Sun, L. D.; Yan, C. H. Highly efficient multicolor upconversion emissions and their mechanisms of monodisperse $NaYF_4$:Yb,Er core and core/shell-structured nanocrystals. *J. Phys. Chem. C* **2007**, *111*, 13721-13729.

21. Wang, F.; Liu, X. Recent advances in the chemistry of lanthanide-doped upconversion nanocrystals. *Chem. Soc. Rev*. **2009,** *38*, 976-989**.**

22. Feng, W.; Han, C.; Li, F. Upconversion-nanophosphor-based functional nanocomposites. *Adv. Mater*. **2013**, *25*, 5287-5303.

23. Chen, G.; Qiu, H.; Prasad, P. N.; Chen, X. Upconversion nanoparticles: design, nanochemistry, and applications in theranostics. *Chem. Rev*. **2014**, *114*, 5161-5214.

24. Yi, G. S.; Chow, G. M. Water-soluble $NaYF_4$:Yb,Er(Tm)/$NaYF_4$/polymer core/shell/shell nanoparticles with significant enhancement of upconversion fluorescence. *Chem. Mater*. **2007**, *19*, 341-343.

25. Qian, H. S.; Zhang, Y. Synthesis of hexagonal-phase core−shell $NaYF_4$ nanocrystals with tunable upconversion fluorescence. *Langmuir* **2008**, *24*, 12123-12125.

26. Yang, T.; Sun, Y.; Liu, Q.; Feng, W.; Yang, P.; Li, F. Cubic sub-20 nm $NaLuF_4$-based up conversion nanophosphors for high-contrast bioimaging in different animal species. *Biomaterials* **2012**, *33*, 3733-3742.

27. Mahalingam, V.; Vetrone, F.; Naccache, R.; Speghini, A.; Capobianco, J. A. Colloidal Tm^{3+}/Yb^{3+} doped $LiYF_4$ nanocrystals: Multiple luminescence spanning the UV to NIR regions via low-energy excitation. *Adv. Mater*. **2009**, *21*, 4025-4028.

28. Yin, A.; Zhang, Y.; Sun, L. Yan, C. Colloidal synthesis and blue based multicolor upconversion emissions of size and composition controlled monodisperse hexagonal $NaYF_4$:Yb,Tm nanocrystals. *Nanoscale* **2010**, *2*, 953-959.

29. Lin, M.; Zhao, Y.; Wang, S.; Liu, M.; Duan, Z, Chen, Y.; Li, F.; Xu, F.; Lu, T. Recent advances in synthesis and surface modification of lanthanide-doped upconversion nanoparticles for biomedical applications. *Biotechnol. Adv*. **2012**, *30*, 1551-1561.

30. Heer, S.; Kompe, K.; Gudel, H. U.; Haase, M. Highly efficient multicolour upconversion emission in transparent colloids of lanthanide-doped $NaYF_4$ nanocrystals. *Adv. Mater*. **2004**,*16*, 2102.

31. Boyer, J. C.; Vetrone, F.; Cuccia, L. A.; Capobianco, J. A. Synthesis of colloidal upconverting $NaYF_4$ nanocrystals doped With Er^{3+}, Yb^{3+} And Tm^{3+}, Yb^{3+} via thermal decomposition of lanthanide trifluoroacetate precursors. *J. Am. Chem. Soc*. **2006**, *128*, 7444-7445.

32. Dong, H.; Sun, L. D.; Yan, C. H. Energy transfer in lanthanide upconversion studies for extended optical applications. *Chem. Soc. Rev*. **2015**, *44*, 1608-1634.

33. Bloembergen N. Solid state infrared quantum counters. *Phys. Rev. Lett*. **1959**, *2*, 84–85.

34. Auzel F. E. Materials and devices using double-pumped phosphors with energy transfer. *Proc IEEE*. **1973**, *61*, 758-786.

35. Chivian J. S.; Case W. E.; Eden, D. D. The photon avalanche: a new phenomenon in Pr^{3+} based infrared quantum counters. *Phys. Rev. Lett*. **1979**, *35*, 124-125.

36. Chen, J.; Zhao, J. X. Upconversion nanoparticles: synthesis, mechanism, and applications in sensing. *Sensors* **2012**, *12*, 2414-2435.

37. Wang, F.; Deng, R.; Wang, J.; Wang, Q.; Han, Y.; Zhu, H.; Chen, X.; Liu, X. Tuning upconversion through energy migration in core–shell nanoparticles. *Nat. Mat*. **2011**,*10*, 968-973.

38. Du H. Y.; Zhang W. H.; Sun J. Y. Structure and upconversion luminescence properties of $BaYF_5$:Yb^{3+},Er^{3+} nanoparticles prepared by different methods. *J. Alloys Compd*. **2011**, *509*, 3413–3418.

39. Wang, F.; Chatterjee D. K.; Li Z. Q.; Zhang Y.; Fan X. P.; Wang M. Q. Synthesis of polyethyleneimine/$NaYF_4$ nanoparticles with upconversion fluorescence. *Nanotechnology* **2006**, *17*, 5786-5791.

40. Li, Z.; Zhang, Y. Monodisperse silica-coated polyvinylpyrrolidone/$NaYF_4$ nanocrystals with multicolor upconversion fluorescence emission. *Angew. Chem. Int. Ed*. **2006**, *118*, 7896–7899.

41. Yi, G.; Lu, H.; Zhao, S. Y.; Ge, Y.; Yang, W; Chen, D.; Guo, L. H. Synthesis, characterization, and biological application of size-controlled nanocrystalline $NaYF_4$:Yb,Er infrared-to-visible upconversion phosphors. *Nano Lett*. **2004**, *4*, 2191–2196.

42. Su, J.; Zhang, Q.L.; Shao, S.F.; Liu, W.P.; Wan, S.M.; Yin, S.T. Phase transition, structure and luminescence of Eu:YAG nanophosphors by co-precipitation method. *J. Alloys Compd*. **2009**, *470*, 306–310.

43. Xu, Z.; Li, C.; Cheng, Z.; Zhang, C.; Li, G.; Peng, C.; Lin, J. Self-assembled 3D architectures of lanthanide orthoborate: hydrothermal synthesis and luminescence properties. *CrystEngComm*. **2010**, *12*, 549-557.

44. Wang, F.; Han, Y.; Lim, C. S.; Lu, Y.; Wang, J.; Xu, J.; Chen, H.; Zhang, C.; Hong, M.; Liu, X. Simultaneous phase and size control of upconversion nanocrystals through lanthanide doping. *Nature* **2010**, *463*,1061-1065.

45. Li, X.; Zhang, F.; Zhao, D. Lab on upconversion nanoparticles: optical properties and applications engineering via designed nanostructure. *Chem. Soc. Rev*. **2015**, *44*, 1346-1378.

46. Chuai, X.; Zhang, D.; Zhao, D.; Zheng, K.; He, C.; Shi, F.; Wang, L.; Chen, H.; Qin, W. Synthesis and characterization of Yb^{3+},Tm^{3+}:Ba_2YF_7 nanocrystalline with efficient upconversion fluorescence. *Mater. Lett*. **2011**, *65*, 2368-2370.

47. Feng, S. H.; Xu, R. R. New materials in hydrothermal synthesis. *Acc. Chem. Res*. **2001**, *34*, 239-247.

48. Huang, P.; Chen, D. Q.; Wang, Y. S. Host-sensitized multicolor tunable luminescence of lanthanide ion doped one-dimensional YVO_4 nanocrystals. *J. Alloys Compd*. **2010**, *509*, 3375-3381.

49. Guo, H.; Li, Z.Q.; Qian, H. S.; Hu, Y.; Muhammad I. N. Seed-mediated synthesis of $NaYF_4$:Yb, Er/$NaGdF_4$ nanocrystals with improved upconversion fluorescence and MR relaxivity. *Nanotechnology* **2010**, *21*, 125602.

50. Niu, W. B.; Wu, S.; Zhang, S.F.; Li, J.; Li, L. Multicolor output and shape-controlled synthesis of lanthanide ion doped fluorides upconversion nanoparticles. *Dalton Trans*. **2011**, *40*, 3305–3314.

51. Yan, Z. G.; Yan, C. H.; Controlled synthesis of rare earth nanostructures. *J. Mater. Chem*. **2008**, *18*, 5046–5059.

52. Zhang, F.; Li, J.; Shan, J.; Xu, L.; Zhao, D. Shape, size, and phase-controlled rare-earth fluoride nanocrystals with optical upconversion properties. *Chem. Eur. J.* **2009**, *15*, 11010–11019.

53. Liu, Y. X.; Pisarski, W. A.; Zeng, S. J.; Xu, C. F.; Yang, Q. B. Tri-color upconversion luminescence of rare earth doped $BaTiO_3$ nanocrystals and lowered color separation. *Opt. Express*. **2009**,*17*, 9089–9098.

54. Wang, L. Y.; Zhang, Y.; Zhu, Y. Y. One-pot synthesis and strong near-infrared upconversion luminescence of poly(acrylicacid)-functionalized $YF_3:Yb^{3+}/Er^{3+}$ nanocrystals. *Nano Res*. **2010**, *3*, 317–325.

55. Wang, X.; Chen, J. T.; Zhu, H.; Chen, X.; Yan, X. P. One step solvothermal synthesis of targetable optomagnetic upconversion nanoparticles for in vivo bimodal imaging. *Anal. Chem*. **2013**, *85*, 10225-10231.

56. Yang, K.; Zheng, F.; Wu, R.; Li, H.; Zhang, X. Upconversion luminescent properties of $YVO_4:Yb^{3+}$, Er^{3+} nanopowder by sol-gel method. *J. Rare Earths* **2006**, *24*, 162–166.

57. Patra, A.; Friend, C.S.; Kapoor, R.; Prasad, P.N. Fluorescence upconversion properties of Er^{3+}-doped TiO_2 and $BaTiO_3$ nanocrystallites. *Chem. Mater*. **2003**, *15*, 3650–3655.

58. Patra, A.; Friend, C.S.; Kapoor, R.; Prasad, P.N. Upconversion in $Er^{3+}:ZrO_2$ nanocrystals. *J. Phys. Chem. B* **2002**, *106*, 1909–1912.

59. Sivakumar, S.; Van Veggel, F. C. J. M.; Raudsepp, M. Bright white light through up-conversion of a single NIR source from sol-gel-derived thin film made with Ln^{3+}-doped LaF_3 nanoparticles. *J. Am. Chem. Soc*. **2005**, *127*, 12464-12465.

60. Sivakumar, S.; Van Veggel, F. C. J. M.; Stanley, P. M. Near-infrared (NIR) to red and green up-conversion emission from silica sol−gel thin films made with $La_{0.45}Yb_{0.50}Er_{0.05}F_3$ nanoparticles, Hetero-Looping-Enhanced Energy Transfer (Hetero-LEET): A new up-conversion process. *J. Am. Chem. Soc.* **2007**, *129*, 620–625.

61. Li, Z.; Zhang, Y.; Jiang.; S. Multicolor core/shell-structured upconversion fluorescent nanoparticles. *Adv. Mater*. **2008**, *20*, 4765–4769.

62. Abel, K. A.; Boyer, J. C.; Van Veggel, F. C. J. M. Hard proof of the $NaYF_4$/$NaGdF_4$ nanocrystal core/shell structure. *J. Am. Chem. Soc*. **2009**, *131*, 14644–14645.

63. Li, Z.; Zhang, Y. An efficient and user-friendly method for the synthesis of hexagonal-phase $NaYF_4$:Yb, Er/Tm nanocrystals with controllable shape and upconversion fluorescence, *Nanotechnology* **2008**, *19*, 345606.

64. Li, C.; Lin, J. Rare earth fluoride nano-/microcrystals: Synthesis, surface modification and application, *J. Mater. Chem*. **2010**, *20*, 6831–6847.

65. Yi, G. S.; Chow, G. M. Synthesis of hexagonal-phase $NaYF_4$:Yb, Er and $NaYF_4$:Yb,Tm nanocrystals with efficient up-conversion fluorescence. *Adv. Funct. Mater*. **2006**, *16*, 2324–2329.

66. J. Shan, Y. Ju, A single-step synthesis and the kinetic mechanism for monodisperse and hexagonal phase $NaYF_4$:Yb, Er upconversion nanophosphors. *Nanotechnology* **2009**, *20*, 275603.

67. Kingshott, P.; Anderson, G.; McArthur, S. L.; Griesser, H. J. Surface modification and chemical surface analysis of biomaterials. *Curr. Opin. Chem. Biol*. **2011**, *15*, 667-676.

68. Niedbala, R. S.; Feindt, H.; Kardos, K.; Vail, T.; Burton, J.; Bielska, B.; Li, S.; Milunic, D.; Bourdelle, P.; Vallejo, R. Detection of analytes by immunoassay using up-converting phosphor technology. *Anal Biochem*. **2001**, *293*, 22–30.

69. Gaoshuang Hu, Wei Sheng, Yan Zhang, Junping Wang, Xuening Wu, Shuo Wang. Upconversion nanoparticles and monodispersed magnetic polystyrene microsphere-based fluorescence immunoassay for the detection of sulfaquinoxaline in animal-derived foods. *J. Agric. Food Chem.* **2016**, *64*, 3908–3915.

70. Huang, Z.; Wu, S.; Duan, N.; Hua, D.; Hu, Y.; Wang, Z. Sensitive detection of carcinoembryonic antigen with magnetic nanobead and upconversion nanoparticles-based immunoassay. *J. Pharm Biomed. Anal*. **2012**, *66*, 225-31.

71. Hu, H.; Xiong, L. Q.; Zhou, J.; Li, F. Y.; Cao, T. Y.; Huang, C. H. Multimodal-luminescence core–shell nanocomposites for targeted imaging of tumor cells. *Chem. Eur. J.* **2009**, *15*, 3577–3584.

72. Xiong, L.Q.; Chen, Z. G.; Yu, M. X.; Li, F. Y.; Liu, C.; Huang, C. H. Synthesis, characterization, and invivo targeted imaging of amine-functionalized rare-earth up-converting nanophosphors. *Biomaterials* **2009**, *30*, 5592–600.

73. Hemmer, E.; Nallusamy, V.; Hiroshi, H.; Akito, H.; Yoshie, E.; Hidehiro, K.; Kohei, S. Upconverting and NIR emitting rare earth based nanostructures for NIR-bioimaging. *Nanoscale* **2013**, *5*, 11339-11361.

74. Hemmer, E.; Antonio, B.; François, L.; Vetrone, F. Exploiting the biological windows: current perspectives on fluorescent bioprobes emitting above 1000 nm. *Nanoscale Horiz*. **2016**, *1*, 168-184.

75. Xiong, L. Q.; Yang, T. S.; Yang, Y.; Xu, C. J.; Li, F. Y. Long-term in vivo biodistribution imaging and toxicity of polyacrylic acid-coated upconversion nanophosphors. *Biomaterials* **2010**, *31*, 7078–7085.

76. Li, R.; Ji, Z.; Dong, J.; Chang, C. H.; Wang, X.; Sun, B.; Wang, M.; Liao, Y. P.; Zink, J. I.; Nei, A. E.; Xia. T. Enhancing the imaging and biosafety of upconversion nanoparticles through phosphonate coating. *ACS Nano* **2015**, *9*, 3293–3306.

77. Ang, L. Y.; Lim, M. E.; Ong, L. C.; Zhang, Y. Applications of upconversion nanoparticles in imaging, detection and therapy. *Nanomedicine* **2011**, *6*, 1273-1288.

78. Zhang, F.; Shi, Q. H.; Zhang, Y. C.; Shi, Y. F.; Ding, K. L.; Zhao, D. Y.; Stucky, G. D. Fluorescence upconversion microbarcodes for multiplexed biological detection: nucleic acid encoding. *Adv. Mater*. **2011**, *23*, 3775–3779.

79. Wang, C.; Tao, H.; Cheng, L.; Liu. Z. Near-infrared light induced in vivo photodynamic therapy of cancer based on upconversion nanoparticles. *Biomaterials* **2011**, *32*, 6145–6154.

80. Wang, C.; Cheng, L.; Liu, Z. Drug delivery with upconversion nanoparticles for multi-functional targeted cancer cell imaging and therapy. *Biomaterials* **2011**, *32*, 1110–1120.

81. Cheng, L.; Wang, C.; Liu, Z. Upconversion nanoparticles and their composite nanostructures for biomedical imaging and cancer therapy. *Nanoscale* **2013**, *5*, 23-37.

82. Liang, L.; Care, A.; Zhang, R.; Lu, Y.; Packer, N. H.; Sunna, A.; Qian, Y.; Zvyagin, A. V. Facile assembly of functional upconversion nanoparticles for targeted cancer imaging and photodynamic therapy. *ACS Appl. Mater. Interfaces* **2016**, *8*, 11945–11953.

83. DeRijke, V. F.; Zijlmans, H.; Li, S.; Vail, T.; Raap, A. K.; Niedbala, R. S. Up-converting phosphor reporters for nucleic acid microarrays. *Nat. Biotechnol*. **2001**, *19*, 273–276.

84. Han, G. M.; Li, H.; Huang, X. X.; Kong, D. M. Simple synthesis of carboxyl-functionalized upconversion nanoparticles for biosensing and bioimaging applications. *Talanta* **2016**, *147*, 207–212.

85. Wang, L.; Yan, R.; Huo, Z.; Wang, L.; Zeng, J.; Bao, J.; Wang, X.; Peng, Q.; Li, Y. Fluorescence resonant energy transfer biosensor based on upconversion-luminescent nanoparticles. *Angew. Chem. Int. Ed*. **2005**, *44*, 6054–6057.

86. Zhu, H.; Ding, Y.; Wang, A.; Sun, X.; Wu, X. C.; Zhu. J. J. A simple strategy based on upconversion nanoparticles for a fluorescent resonant energy transfer biosensor. *J. Mater. Chem. B* **2015**, *3*, 458-464.

87. Muhr, V.; Wilhelm, S.; Hirsch, T.; Wolfbeis, O. S. Upconversion nanoparticles: from hydrophobic to hydrophilic surfaces. *Acc. Chem. Res*. **2014**, *47*, 3481–3493.

88. Sedlmeier, A.; Gorris, H. H. Surface modification and characterization of photon upconverting nanoparticles for bioanalytical applications. *Chem. Soc. Rev*. **2015**, *44*, 1526-1560.

89. Wilhelm, S.; Kaiser, M.; Würth, C.; Heiland, J.; Carrion, C. C.; Muhr, V.; Wolfbeis, O. S.; Parak, W. J.; Genger, U. R.; Hirsch, T. Water dispersible upconverting nanoparticles: effects of surface modification on their luminescence and colloidal stability. *Nanoscale* **2015**, *7*, 1403-1410.

90. Erathodiyil, N.; Ying, J. Y. Functionalization of inorganic nanoparticles for bioimaging applications. *Acc. Chem. Res*. **2011**, *44*, 925-935.

91. Chen, Z.; Chen, H.; Hu, H.; Yu, M.; Li, F.; Zhang, Q.; Zhou, Z.; Yi, T.; Huang, C. Versatile synthesis strategy for carboxylic acid- functionalized upconverting nanophosphors as biological labels. *J. Am. Chem. Soc*. **2008**, *130*, 3023−3029.

92. Zhou, H.-P.; Xu, C.-H.; Sun, W.; Yan, C.-H. Clean and flexible modification strategy for carboxyl/aldehyde-functionalized upconversion nanoparticles and their optical applications. *Adv. Funct. Mater*. **2009**, *19*, 3892-3900.

93. Hu, H.; Yu, M.; Li, F.; Chen, Z.; Gao, X.; Xiong, L.; Huang, C. Facile epoxidation strategy for producing amphiphilic up-converting rare-earth nanophosphors as biological labels. *Chem. Mater*. **2008**, *20*, 7003-7009.

94. Dai, Y.; Yang, D.; Ma, P.; Kang, X.; Zhang, X.; Li, C.; Hou, Z.; Cheng, Z.; Lin, J. Doxorubicin conjugated $NaYF_4$:Yb^{3+}/Tm^{3+} nanoparticles for therapy and sensing of drug delivery by luminescence resonance energy transfer. *Biomaterials* **2012**, *33*, 8704-8713.

95. Yang, S.; Li, N.; Liu, Z.; Sha, W.; Chen, D.; Xu, Q.; Lu, J. Amphiphilic copolymer coated upconversion nanoparticles for near-infrared light-triggered dual anticancer treatment**.** *Nanoscale*, **2014**, *6*, 14903-14910.

96. Liras, M.; Béjar, M. G.; Peinado, E.; Soriano, L. F.; Prieto, J. P.; Garrido, I. Q.; García, O. Thin amphiphilic polymer-capped upconversion nanoparticles: enhanced emission and thermoresponsive properties. *Chem. Mater*. **2014**, *26*, 4014-4022.

97. Rieffel, J.; Chen, F.; Kim, J.; Chen, G.; Shao, W.; Shao, S.; Chitgupi, U.; Hernandez, R.; Graves, S. A.; Nickles, R. J.; Prasad, P. N.; Kim, C.; Cai, W.; Lovell, J. F. Hexamodal imaging with porphyrin-phospholipid-coated upconversion nanoparticles. *Adv. Mater*. **2015**, *27*, 1785–1790.

98. Huang, Y.; Hemmer, E.; Rosei, F.; Vetrone, F. Multifunctional liposome nanocarriers combining upconverting nanoparticles and anticancer drugs. *J. Phys. Chem. B* **2016**, *120*, 4992–5001**.**

99. Park, Y. I.; Kim, J. H.; Lee, K. T.; Jeon, K. S.; Na, H. B.; Yu, J. H.; Kim, H. M.; Lee, N.; Choi, S. H.; Baik, S. I.; Kim, H.; Park, S. P.; Park, B. J.; Kim, Y. W.; Lee, S. H.; Yoon, S. Y.; Song, I. C.; Moon, W. K.; Suh, Y. D.; Hyeon, T. Nonblinking and nonbleaching upconverting nanoparticles as an optical Imaging nanoprobe and T1 magnetic resonance imaging contrast agent. *Adv. Mater*. **2009**, *21*, 4467−4471.

100. Nam, S. H.; Bae, Y. M.; Park, Y. I.; Kim, J. H.; Kim, H. M.; Choi, J. S.; Lee, K. T.; Hyeon, T.; Suh, Y. D. Long-term real-time tracking of lanthanide ion doped upconverting nanoparticles in living cells. *Angew. Chem*. *Int. Ed*. **2011**, *123*, 6217−6221.

101. Pellegrino, T.; Manna, L.; Kudera, S.; Liedl, T.; Koktysh, D.; Rogach, A. L.; Keller, S.; Rädler, J.; Natile, G.; Parak, W. J. Hydrophobic nanocrystals coated with an amphiphilic polymer shell: A general route to water soluble nanocrystals. *Nano Lett*. **2004**, *4*, 703−707.

102. Jia, X.; Yin, J.; He, D.; He, X.; Wang, K.; Chen, M.; Li, Y. Polyacrylic acid modified upconversion nanoparticles for simultaneous pH-triggered drug delivery and release imaging. *J. Biomed. Nanotechnol*. **2013**, *9*, 2063-2072.

103. Xiong, L.; Yang, T.; Yang, Y.; Xu, C.; Li. F. Long-term in vivo biodistribution imaging and toxicity of polyacrylic acid-coated upconversion nanophosphors. *Biomaterials* **2010**, *31*, 7078-7085.

104. Cheng, L.; Yang, K.; Zhang, S.; Shao, M.; Lee, S.; Liu, Z. Highly-sensitive multiplexed in vivo imaging using PEG-ylated upconversion nanoparticles. *Nano Res*. **2010**, *3*, 722−732.

105. Cui, S.; Chen, H.; Zhu, H.; Tian, J.; Chi, X.; Qian, Z.; Achilefu, S.; Gu, Y. Amphiphilic chitosan modified upconversion nanoparticles for in vivo photodynamic therapy induced by near-infrared Light. *J. Mater. Chem*. **2012**, *22*, 4861−4873.

106. Mine, E.; Yamada, A.; Kobayashi, Y.; Konno, M.; Liz-Marzán, L. M. Direct coating of gold nanoparticles with silica by a seeded polymerization technique. *J. Colloid Interface Sci*. **2003**, *264*, 385–390.

107. Jalil, R. A.; Zhang, Y. Biocompatibility of silica-coated $NaYF_4$ Upconversion fluorescent nanocrystals. *Biomaterials* **2008**, *29*, 4122−4128.

108. Liu, S.; Zhan, H. L.; Liu, T. C.; Liu, B.; Cao, Y. C.; Huang, Z. L.; Zhao, Y. D.; Luo, Q. M. Optimization of the methods for introduction of amine groups onto the silica nanoparticle surface, *J. Biomed. Mater. Res. A*. **2007**, *80 A*, 752-757.

109. Corstjens, P. L. A. M.; Zuiderwijk, M.; Nilsson, M.; Feindt, H.; Niedbala, R. S.; Tanke, H. J. Lateral flow and up-converting phosphor reporters to detect single-stranded nucleic Acids in a sandwich hybridization assay, *Anal. Biochem*. **2003**, *312*, 191-200.

110. Dong, B.; Xu, S.; Sun, J.; Bi, S.; Li, D.; Bai, X.; Wang, Y.; Wang, L.; Song, H. Multifunctional$NaYF_4:Yb^{3+},Er^{3+}$@Ag core/shell nanocomposites: Integration of upconversion imaging and photothermal therapy. *J. Mater. Chem*. **2011**, *21*, 6193−6200.

111. Xia, L.; Kong, X.; Liu, X.; Tu, L.; Zhang, Y.; Chang, Y.; Liu, K.; Shen, D.; Zhao, H.; Zhang, H. An upconversion nanoparticle - Zinc phthalocyanine-based nanophotosensitizer for photodynamic therapy. *Biomaterials* **2014**, *35*, 4146−4156.

112. Bogdan, N.; Vetrone, F.; Ozin, G. A.; Capobianco, J. A. Synthesis of ligand-free colloidally stable water-dispersible brightly luminescent lanthanide-doped upconverting nanoparticles. *Nano Lett*. **2011**, *11*, 835−840.

113. Thevenot, D. R.; Toth, K.; Durst, R. A.; Wilson, G. S. Electrochemical biosensors: recommended definitions and classification. *Biosens. Bioelectron*. **2001**, *16*, 121–131.

114. Turner, A. P. F. Biosensors: sense and sensibility. *Chem. Soc. Rev*. **2013**, *42*, 3184-3196.

115. Sassolas, A.; Beatrice, D. Bouvier, L.; Blum. L. J. DNA biosensors and microarrays. *Chem. Rev*. **2008**, *108*, 109-139.

116. Tyagi, S.; Kramer, F. R. Molecular beacons: probes that fluoresce upon hybridization. *Nat. Biotechnol*. **1996**, *14*, 303-308.

117. Kalogianni, D. P.; Koraki, T.; Christopoulos, T.K.; Ioannou. P. C. Nanoparticle-based DNA biosensor for visual detection of genetically modified organisms. *Biosens. Bioelectron*. **2006**, *21*, 1069–1076.

118. Zhang, J.; Song, S.; Wang, L.; Pan, D.; Fan. C. A gold nanoparticle-based chronocoulometric DNA sensor for amplified detection of DNA. *Nat. Protoc.* **2007**, *2*, 2888-2895.

119. Möller, R.; Fritzsche, W. Metal nanoparticle-based detection for DNA analysis. *Curr. Pharm. Biotechnol*. **2007**, *5*, 274-285.

120. Jain, P. K.; Huang, X.; El-Sayed, I. H.; El-Sayed, M. A. Noble metals on the nanoscale: optical and photothermal properties and some applications in imaging, sensing, biology, and medicine. *Acc. Chem. Res*. **2008**, *12*, 1578-1586.

121. Zhang, C. Y.; Yeh, H. C.; Kuroki, M. T.; Wang. T. H. Single quantum dot based DNA nanosensor. *Nat. Mater*. **2005**, *4*, 826-831.

122. Wang, Y.; Hu, R.; Lin, G.; Roy, I.; Yong, K.T. Functionalized quantum dots for biosensing and bioimaging and concerns on toxicity. *ACS Appl. Mater. Interfaces* **2013**, *5*, 2786–2799.

123. Freeman, R.; Girsh, J.; Willner, I. Nucleic acid/quantum dots (QDs) hybrid systems for optical and photoelectrochemical sensing. *ACS Appl. Mater. Interfaces* **2013**, *5*, 2815-2834.

124. Loo, A. H.; Sofer, Z.; Bousa, D.; Ulbrich, P.; Bonanni, A.; Pumera, M. Carboxylic carbon quantum dots as a fluorescent sensing platform for DNA detection. *ACS Appl. Mater. Interfaces*, **2016**, *8*, 1951–1957.

125. Petryayeva, E.; Algar, W. R.; Medintz, I. L. Quantum dots in bioanalysis: a review of applications across various platforms for fluorescence spectroscopy and imaging. *Appl. Spectrosc*. **2013**, *67*, 215-252.

126. Selvin, P. R. Lanthanide-based resonance energy transfer. *IEEE J. Sel. Top. Quantum Electron*. **1996**, *4*, 1077-1087.

127. Béjar, M. G.; Soriano, L. F.; Prieto, J. P. Upconversion nanoparticles for bioimaging and regenerative medicine. *Front. Bioeng. Biotechnol*. **2016**, *4*, 1-9.

128. Xiang, Y.; Tong, A.; Jin, P.; Ju, Y. New fluorescent rhodamine hydrazone chemosensor for Cu (II) with high selectivity and sensitivity. *Org. Lett*. **2006**, *8*, 2863-2866.

129. Moon, S. Y.; Cha, N. R.; Kim, Y. H.; Chang. S. K. New Hg^{2+}-selective chromo- and fluoroionophore based upon 8-hydroxyquinoline. *J. Org. Chem*. **2004**, *69*, 181–183.

130. Taki, M.; Desaki, M.; Ojida, A.; Iyoshi, S.; Hirayama, T.; Hamachi, I.; Yamamoto, Y. Fluorescence imaging of intracellular cadmium using a dual-excitation ratiometric chemosensor. *J. Am. Chem. Soc*. **2008**, *130*, 12564−12565.

131. Huang, C.; Yang, Z.; Lee, K. H.; Chang, H. T. Synthesis of highly fluorescent gold nanoparticles for sensing Mercury (II). *Angew. Chem. Int. Ed*. **2007**, *46*, 6824−6828.

132. Kramer, R. Fluorescent chemosensors for Cu^{2+} ions: Fast, selective, and highly sensitive. *Angew. Chem. Int. Ed*. **1998**, *37*, 772−773.

133. Zhang, X. B.; Peng, J.; He, C. L.; Shen, G. L.; Yu, R. Q. A highly selective fluorescent sensor for Cu^{2+} Based on 2-(2′-hydroxyphenyl)benzoxazole in a poly(vinyl chloride) matrix. *Anal. Chim. Acta* **2006**, *567*, 189−195.

134. Sarkar, B. Metal ions in biological systems. *Marcel Dekker Ed*. New York, **1981**, *12*, 233.

135. Barnham, K. J.; Masters, C. L.; Bush, A. I. Neurodegenerative diseases and oxidative stress. *Nat. Rev. Drug Discov*. **2004**, *3*, 205−214.

136. Mare, S.; Penugonda, S.; Robinson, S. M.; Dohgu, S.; Banks, W. A.; Ercal, N. Copper complexing decreases the ability of amyloid beta peptide to cross the BBB and enter brain parenchyma. *Peptides* **2007**, *28*, 1424−1432.

137. Lee, J. C.; Gray, H. B.; Winkler, J. R. Copper (II) binding to α-Synuclein-the Parkinson's protein. *J. Am. Chem. Soc*. **2008**, *130*, 6898−6899.

138. Zhou, Y.; Wang, F.; Kim, Y.; Kim, S. J.; Yoon, J. Cu^{2+}-selective ratiometric and ″off-on″ sensor based on the rhodamine derivative bearing pyrene group. *Org. Lett*. **2009**, *11*, 4442−4445.

139. Khatua, S.; Choi, S. H.; Lee, J.; Huh, J. O.; Do, Y.; Churchill, D. G. Highly selective fluorescence detection of Cu^{2+} in water by chiral dimeric Zn^{2+} complexes through direct displacement. *Inorg. Chem*. **2009**, *48*, 1799−1801.

140. Lin, W.; Yuan, L.; Tan, W.; Feng, J.; Long, L. Construction of fluorescent probes via protection/deprotection of functional groups: A ratiometric fluorescent probe for copper. *Chem. Eur. J*. **2009**, *15*, 1030−1035.

141. Chan, Y. H.; Jin, Y.; Wu, C.; Chiu, D. T. Copper (II) and Iron (II) ion sensing with semiconducting polymer dots. *Chem. Commun*. **2011**, *47*, 2820−2822.

142. Kim, Y.; Johnson, R. C.; Hupp, J. T. Gold nanoparticle-based sensing of spectroscopically silent heavy metal ions. *Nano Lett*. **2001**, *1*, 165−167.

143. Meng, Q.; Zhang, X.; He, C.; He, G.; Zhou, P.; Duan, C. Multifunctional mesoporous silica material used for detection and adsorption of Cu^{2+} in aqueous solution and biological applications in-vitro and in-vivo. *Adv. Funct. Mater*. **2010**, *20*, 1903−1909.

144. Chen, W.; Tu, X.; Guo, X. Fluorescent gold nanoparticles-based fluorescence sensor for copper Ions. *Chem. Commun*. **2009**, 1736−1738.

145. Zhou, Y.; Zhao, H.; He, Y.; Ding, N.; Cao, Q. Colorimetric detection of Cu^{2+} Using 4-mercaptobenzoic acid modified silver nanoparticles. *Colloids Surf. A* **2011**, *391*, 179−183.

146. Chan, Y. H.; Chen, J.; Liu, Q.; Wark, S. E.; Son, D. H.; Batteas, J. D. Ultrasensitive copper (II) detection using plasmon-enhanced and photo-brightened luminescence of CdSe quantum dots. *Anal. Chem*. **2010**, *82*, 3671−3678.

147. Koneswaran, M.; Narayanaswamy, R. I. Cysteine-capped ZnS quantum dots based fluorescence sensor for Cu^{2+} Ion. *Sens. Actuators*, *B* **2009**, *139*, 104−109.

148. George, A.; Shibu, E. S.; Maliyekkal, S. M.; Bootharaju, M. S.; Pradeep, T. Luminescent, freestanding composite films of Au_{15} for specific metal ion sensing. *ACS Appl. Mater. Interfaces* **2012**, *4*, 639−644.

149. Wu, P. J.; Chen, J. L.; Chen, C. P.; Chan, Y. H. Photoactivated ratiometric copper (II) ion sensing with semiconducting polymer dots. *Chem. Commun*. **2013**, *49*, 898−900.

150. Yang, P.; Zhao, Y.; Lu, Y.; Xu, Q. Z.; Xu, X. W.; Dong, L.; Yu, S. H. Phenol formaldehyde resin nanoparticles loaded with CdTe quantum dots: A fluorescence resonance energy transfer probe for optical visual detection of copper (II) ions. *ACS Nano* **2011**, *5*, 2147−2154.

151. Salinas-Castillo, A.; Ariza-Avidad, M.; Pritz, C.; Camprubí-Robles, M.; Fernandez, B.; Ruedas-Rama, M. J.; Megia-Fernandez, A.; Lapresta-Fernandez, A.; Santoyo-Gonzalez, F.; Schrott-Fischer, A.; Capitan-Vallvey, L. F. Carbon dots for Cu^{2+} detection with down and upconversion fluorescent properties as excitation sources. *Chem. Commun*. **2013**, *49*, 1103−1105.

152. Zhang, J.; Yuan, Y.; Liang, G.; Arshad, M. N.; Albar, H. A.; Sobahi, T. R.; Yu, S. H. A Microwave-facilitated rapid synthesis of gold nanoclusters with tunable optical properties for sensing ions and fluorescent ink. *Chem. Commun*. **2015**, *51*, 10539−10542.

153. Weiss, E. A.; Chiechi, R. C.; Geyer, S. M.; Porter, V. J.; Bell, D. C.; Bawendi, M. G.; Whitesides, G. M. Size-dependent charge collection in junctions containing single-size and multi-size arrays of colloidal CdSe quantum dots. *J. Am. Chem. Soc*. **2008**, *130*, 74−82.

154. Walker, B. J.; Nair, G. P.; Marshall, L. F.; Bulovic, V.; Bawendi, M. G. Size-dependent charge collection in junctions containing single-size and multi-size arrays of colloidal CdSe quantum dots. *J. Am. Chem. Soc*. **2009**, *131*, 9624−9625.

155. Zhang, J.; Li, B.; Zhang, L.; Jiang, H. An optical sensor for Cu (II) detection with upconverting luminescent nanoparticles as an excitation source. *Chem. Commun*. **2012**, *48*, 4860−4862.

156. Turrens, J. F. Mitochondrial formation of reactive oxygen species. *J. Physiol*. **2003**, *552*, 335-344.

157. Gerschman, R.; Gilbert, D. L.; Nye, S. W.; Dwyer, P.; Fenn. W. O. Oxygen poisoning and x-irradiation: mechanism in common. *Science* **1954**, *119*, 623-626.

158. Ding, N. C. A SnapShot: Reactive Oxygen Intermediates (ROI). *Cell* **2010**, *140*, 951-951.

159. Halliwell, B. Oxidative stress and neurodegeneration: where are we now? *J. Neurochem*. **2006**, *97*, 1634–1658.

160. Halliwell, B.; Gutteridge, J. M. C. Free radicals in biology and medicine. **2015**, Ed. *5*. Oxford University Press, Oxford, United Kingdom.

161. Finkel, T.; Holbrook, N. J. Oxidants, oxidative stress and the biology of aging. *Nature*, **2000**, *408*, 239-247.

162. Dickinson, B. C.; Chang, C. J. Chemistry and biology of reactive oxygen species in signaling or stress responses. *Nat. Chem. Biol*. **2011**, *7*, 504-511.

163. Dröge, W. Free Radicals in the physiological control of cell function. *Physiol. Rev*. **2002**, *82*, 47- 95.

164. Barnham, K. J.; Masters, C. L.; Bush, A. I. Neurodegenerative diseases and oxidative stress. *Nat. Rev. Drug Discov*. **2004**, *3*, 205-214.

165. Finkel, T.; Serrano, M.; Blasco, M. A. The common biology of cancer and aging. *Nature* **2007**, *448*, 767-774.

166. Mroz, P.; Huang, Y.Y.; Szokalska, A.; Zhiyentayev, T.; Janjua, S.; Nifli, A.P.; Sherwood, M.E.; Ruzie, C.; Borbas, K.E.; Fan, D.; Krayer, M.; Balasubramanian, T.; Yang, E.; Kee, H.L.; Kirmaier, C.; Diers, J.R.; Bocian, D.F.; Holten, D.; Lindsey, J.S.; Hamblin, M.R. Stable synthetic bacteriochlorins overcome the resistance of melanoma to photodynamic therapy. *FASEB. J*. **2010**, *24*, 3160-3170.

167. Mroz, P.; Bhaumik, J.; Dogutan, D.K.; Aly, Z.; Kamal, Z.; Khalid, L.; Kee, H.L.; Bocian, D.F.; Holten, D.; Lindsey, J.S.; Hamblin, M.R. Imidazole metalloporphyrins as photosensitizers for photodynamic therapy: Role of molecular charge, central metal and hydroxyl radical production. *Cancer Lett*. **2009**, *282*, 63-76.

168. Mroz, P.; Pawlak, A.; Satti, M.; Lee, H.; Wharton, T.; Gali, H.; Sarna, T.; Hamblin, M.R. Functionalized fullerenes mediate photodynamic killing of cancer cells: Type I versus Type II photochemical mechanism. *Free Radic. Biol. Med*. **2007**, *43*, 711-719.

169. Henderson, B.W.; Dougherty, T.J. How does photodynamic therapy work? *Photochem. Photobiol*. **1992**, *55*, 145-157.

170. Vrouenraets, M.B.; Visser, G.W.; Snow, G.B.; Van Dongen, G.A. Basic principles, applications in oncology and improved selectivity of photodynamic therapy. *Anticancer Res*. **2003**, *23*, 505-522.

171. DeRosa M. C.; Crutchley, R. J. Photosensitized singlet oxygen and its applications. *Coord. Chem. Rev*. **2002**, *233-234*, 351-371.

172. Detty, M. R.; Gibson, S. L.; Wagner, S. J. Current clinical and preclinical photosensitizers for use in photodynamic therapy. *J. Med. Chem*. **2004**, *47*, 3897-3915.

173. Yuan, A.; Wu, J.; Tang, X.; Zhao, L.; Xu, F.; Hu, Y. Application of near-infrared dyes for tumor imaging, photothermal, and photodynamic therapies. *J. Pharm. Sci*. **2013**, *102*, 6-28.

174. Josefsen, L. B.; Boyle, R. W. Photodynamic therapy and the development of metal-based photosensitizers. *Met. Based Drugs* **2008**, *276*, 1-24.

175. Ethirajan, M.; Chen, Y.; Joshi, P, Pandey, R. K. The role of porphyrin chemistry in tumor imaging and photodynamic therapy. *Chem. Soc. Rev*. **2011**, *40*, 340-362.

176. Verma, S.; Watt, G.M.; Mai, Z.; Hasan, T. Strategies for enhanced photodynamic therapy effects. *Photochem. Photobiol*. **2007**, *83*, 996-1005.

177. Lo, K. K. W.; Choi, A. W. T.; Law, W. H. T. Applications of luminescent inorganic and organometallic transition metal complexes as biomolecular and cellular probes. *Dalton Trans*. **2012**, *41*, 6021-6027.

178. Zhao, Q.; Huang, C.; Li, F. Phosphorescent heavy-metal complexes for bioimaging. *Chem. Soc. Rev*. **2011**, *40*, 2508-2524.

179. Stacey, O. J.; Pope, S. J. A. New Avenues in the design and potential application of metal complexes for photodynamic therapy. *RSC Adv*. **2013**, *3*, 25550−25564.

180. Zhang, M.; Murakami, T.; Ajima, K.; Tsuchida, K.; Sandanayaka, A. S. D.; Ito, O.; Iijima, S.; Yudasaka, M. Fabrication of ZnPc/protein nanohorns for double photodynamic and hyperthermic cancer phototherapy. *Proc. Natl. Acad. Sci. USA* **2008**, *105*, 14773−14778.

181. Zhang, P.; Steelant, W.; Kumar, M.; Scholfield, M. Versatile photosensitizers for photodynamic therapy at infrared excitation. *J. Am. Chem. Soc*. **2007**, *129*, 4526−4527.

182. Gao, D.; Agayan, R. R.; Xu, H.; Philbert, M. A.; Kopelman, R. Nanoparticles for two-photon photodynamic therapy in living cells. *Nano Lett*. **2006**, *6*, 2383−2386.

183. Gorman, A.; Killoran, J.; O'Shea, C.; Kenna, T.; Gallagher, W. M.; O'Shea, D. F. In-vitro demonstration of the heavy-atom effect for photodynamic therapy. *J. Am. Chem. Soc*. **2004**, *126*, 10619−10631.

184. Kalluru, P.; Vankayala, R.; Chiang, C. S.; Hwang, K. C. Photosensitization of singlet oxygen and in-vivo photodynamic therapeutic effects mediated by PEGylated $W_{18}O_{49}$ nanowires. *Angew. Chem. Int. Ed*. **2013**, *52*, 12332−12336.

185. Idris, N. M.; Gnanasammandhan, M. K.; Zhang, J.; Ho, P. C.; Mahendran, R.; Zhang, Y. In-vivo photodynamic therapy using upconversion nanoparticles as remote-controlled nano transducers. *Nat. Med*. **2012**, *18*, 1580−1585.

186. Jun, Y. W.; Seo, J.W.; Cheon, J. Nanoscaling laws of magnetic nanoparticles and their applicabilities in biomedical sciences. *Acc. Chem. Res*. **2008**, *41*, 179-189.

187. Lee, N.; Yoo, D.; Ling, D.; Cho, M. H.; Hyeon, T.; Cheon. Iron oxide based nanoparticles for multimodal imaging and magnetoresponsive therapy. *Chem. Rev*. **2015**, *115,* 10637-10689.

188. Lee, H.; Shin, T. H.; Cheon, J.; Weissleder. R. Recent developments in magnetic diagnostic systems. *Chem. Rev*. **2015**, *115*, 10690-10724.

189. Huang, P.; Li, Z.; Lin, J.; Yang, D.; Gao, G.; Xu, C.; Bao, L.; Zhang, C.; Wang, K.; Song, H.; Hu, H.; Cui. D. Photosensitizer-conjugated magnetic nanoparticles for in vivo simultaneous magnetofluorescent imaging and targeting therapy. *Biomaterials* **2011**, *32*, 3447-3458.

190. Yen, S. K.; Padmanabhan, P.; Selvan. S. T. Multifunctional iron oxide nanoparticles for diagnostics, therapy and macromolecule delivery. *Theranostics* **2013**, *3*, 986–1003.

191. Reddy, L. H.; Arias, J. L.; Nicolas, J.; Couvreur. P. Magnetic nanoparticles: Design and characterization, toxicity and biocompatibility, pharmaceutical and biomedical applications. *Chem. Rev*. **2012**, *112*, 5818-5878.

192. Tada, D. B.; Vono, L. L. R.; Duarte, E. L.; Itri, R.; Kiyohara, P. K.; Baptista, M. S.; Rossi. L. M. Methylene blue-containing silica-coated magnetic particles: a potential magnetic carrier for photodynamic therapy. *Langmuir* **2007**, *23*, 8194–8199.

193. Lai, C. W.; Wang, Y. H.; Lai, C. H.; Yang, M. J.; Chen, C. Y.; Chou, P. T.; Chan, C. S.; Chi, Y.; Chen, Y. C.; Hsiao. J. K. Iridium complex functionalized Fe_3O_4/SiO_2 core/shell nanoparticles: A facile three-in-one system in magnetic resonance imaging, luminescence imaging, and photodynamic therapy. *Small* **2008**, *4*, 218–224.

AIM OF THE THESIS

The major aim of the thesis is to synthesize blue emitting Tm^{3+}/Yb^{3+} co-doped UCNPs and find novel applications in the field of bio and chemical nanosensing. Since the emission intensity and wavelength of the UCNPs are very much dependent on the local crystal environment, different host crystal shapes (cubic, tetragonal) were synthesized to engineer the local crystal symmetry around the optically active lanthanide dopants. The photophysical and morphological characterizations of the synthesized UCNPs were undertaken using different spectroscopic and surface characterization methods. The synthesized UCNPs were successfully applied in the field of bio/chemo sensing and also for the generation of reactive oxygen species.

More specifically the aims of the thesis is summarized below;

1. To synthesize and apply the blue emitting $NaYF_4$:Yb^{3+},Tm^{3+} UCNPs as the donor for luminescence resonance energy transfer (LRET) based sensitive detection of ssDNA (biosensor) up to picomolar level.

2. To synthesize and apply UV-to-NIR emitting $LiYF_4$:Yb^{3+},Tm^3 UCNPs decorated with the highly photoluminescent natural product, curcumin, for sensitive detection of Cu^{2+} (chemosensor) at NIR excitation wavelengths.

3. To synthesize and apply UV-to-NIR emitting $LiYF_4$:Yb^{3+},Tm^3 UCNPs decorated with an organoiridium complex for the generation of reactive oxygen species (ROS).

4. To synthesize Ir (III) decorated magnetic iron oxide (Fe_3O_4) nanoparticles and apply the nanohybrid for the generation of reactive oxygen species (ROS).

Contributions to Thesis Chapters

In each chapter of this thesis (and hence published/submitted work), I devised all the experiments, synthesized the studied materials and carried out all photophysical, chemical and morphological characterization. I wrote the first drafts of the manuscripts for publication and subsequently made any necessary revisions.

CHAPTER 3 - SENSITIVE DETECTION OF ssDNA USING AN LRET-BASED UPCONVERTING NANOHYBRID MATERIAL

3.1 Abstract

Water-dispersible, optical hybrid nanoparticles are preferred materials for DNA biosensing due to their biocompatibility. Upconverting nanoparticles are highly desirable optical probes in sensors and bioimaging owing to their sharp emission intensity in the visible region. We herein report a highly sensitive ss-DNA detection based on an energy transfer system that uses a nanohybrid material synthesized by doping $NaYF_4$:Tm^{3+}/Yb^{3+} UCNPs on silica coated polystyrene-*co*-acrylic acid (PSA) nanoparticles (PSA/SiO_2) as the donor, and AuNPs decorated with Ir complex as the acceptor. UCNPs tagged on PSA/SiO_2 and the Ir(III)/AuNP conjugates were then linked through the ss-DNA sequence. Sequential addition of the target DNA to the probe molecular beacon complex resulted in the separation of the optical nanohybrid material and the quencher, leading to a measurable increase in the blue fluorescence emission intensity. Our results have shown a linear relationship between the fluorescence intensity and target DNA concentration down to the picomolar.

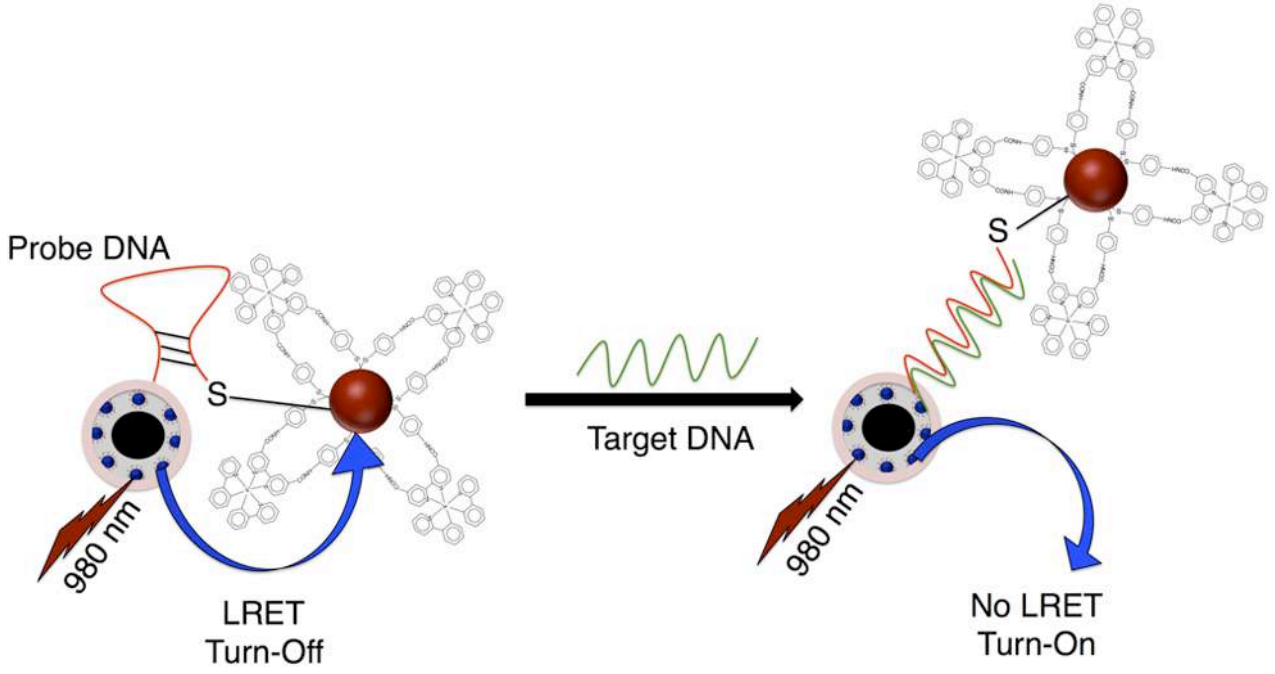

3.2 Introduction

Advancements in pharmacogenomics research, drug discovery, genetics and infectious diseases, as well as the rapid development in DNA research, fuel the need to find more efficient fluorescent labels with improved characteristics. A wide range of fluorescent quantum dots (QDs) were developed and successfully applied in biological analyses [1] and in FRET-based optical detection [2]. However, the use of QDs for detection of biomolecules has certain limitations due to their potential toxicity and high background signal in the presence of interfering fluorescent biomolecules. This problem is common with many other luminescent labels, such as organic dyes or AuNPs, since to get an efficient luminescent signal, they have be excited in the ultraviolet or visible region of the electromagnetic spectrum [3]. A strategy to minimize the background signal is to move the excitation wavelength to the near-infrared (NIR) region. In this range, most organic molecules, as well as water, are transparent, thereby increasing the contrast of the luminescent signal since the excitation wavelength is specific to the optical probe. Recently, nanoparticles doped with Ln^{3+} ions (most commonly Er^{3+}, Tm^{3+}, Yb^{3+} and Ho^{3+}) have gained attention as functional nanoparticles for a variety of biological applications due to their sharp *f–f* emission peaks and long photoluminescence (PL) lifetimes [4-6]. In particular, when added as dopants to transparent host crystals, they provide the possibility of having UV, visible, and even NIR emissions after NIR excitation. This light transformation, known as upconversion (UC), is related to the presence of energy states energetically distributed in a way that several NIR photons can be sequentially absorbed to be emitted in one single step in the form of one higher-energy photon. Since those intermediate states are real electronic states of the ions, this excitation scheme can be carried out using low-cost, continuous wave near-infrared diode lasers. Furthermore, the Ln^{3+} ions are inherently resistant to blinking, photo-bleaching and photo-chemical degradation, which gives them an additional advantage over organic dye markers and quantum dots for bio-labeling and bioassays [7]. For luminescence resonance energy transfer (LRET)-based sensors, the use of upconverting nanoparticles (UCNPs) also guarantees that donor and acceptor will not be excited at the same wavelength since the excitation of the UCNPs takes place at 980 nm NIR wavelength and hence reduces the possibility of autofluorescence and

background interference. This also eliminates the disadvantage of spectral cross-talk signals or other possible errors during the measurement. For this reason, several LRET-based biosensors using UCNPs have been proposed recently, using different strategies and quenchers such as dyes, carbon dots, or AuNPs [8-13]. As excellent luminescent quenchers, AuNPs open new perspectives to detect biomolecules with high sensitivity in FRET systems due to their high extinction coefficients as well as broad absorption spectrum within the visible light range that overlaps with the emission wavelengths of common energy donors [14-17]. Hairpin shaped molecular beacons labeled with AuNPs for DNA bio-sensing through fluorescence resonance energy transfer (FRET) have also been studied [18]. Up to single base DNA mismatch detection was successfully undertaken through the formation of a self-assembled nanostructure that uses AuNPs and a fluorophore through conformational change mechanism [19]. UCNPs-AuNPs donor–acceptor pairs has attracted increasing attention as nanobiosensors for rapid and sensitive detection of virus [20]. Until recently, only bare AuNPs have been used as quenchers in the green spectral range since they show a strong absorbance related to the size-dependent plasmon resonance of the material around the 520 nm region. This limits the use of that donor-acceptor pair to the use of Er^{3+} ions as emitters due to their strong luminescence at green wavelengths, but the work range of UCNPs in LRET can be extended to different colors, which would provide the possibility of simultaneously using different sensing channels. The system proposed in this work uses UCNPs based on Tm^{3+} as activator ion, which is advantageous owing to its upconverted blue emission, a possibility that has not been explored in detail for LRET sensing until now. For this purpose, a more effective AuNP that would absorb most of the donor emissions to enhance the sensitivity of the detection had to be developed. Ir complexes have attracted significant interest due to their strong electrochemiluminescent property. Recently a water-soluble Ir complex with sugar appended ligands for the determination of antibiotics has also been reported [21]. Turn-on FRET-based luminescent Ir(III) probes have also been developed for the detection of cysteine and homocystein [22], and very recently Li and co-workers have developed a DNA biosensor based on Ir(III) and applied successfully for cancer cell detection [23]. The Ir complex offers many advantages such as high stability in the solution state, high photoluminescence and

water-solubility, which makes it suitable for bio-analysis. In the present work, we have developed a highly sensitive biosensor for the detection of target DNA sequence using $NaYF_4$:Tm^{3+}, Yb^{3+} UCNPs on PSA/SiO_2 nanohybrids as donors and Ir-bipyridyl complex immobilized on AuNPs as quenchers. Additionally, to the best of our knowledge there has been no report on the use of UCNPs as an optical biosensor in conjugation with a Ir(III)-AuNP complex as quencher for the detection of *ss*DNA.

3.3 Results and Discussion

The proposed UCNP - LRET biosensor is based on the quenching of the visible emissions produced by $NaYF_4$:Tm^{3+}, Yb^{3+} UCNPs following excitation with 980 nm light. The efficiency of this quenching, as it usually happens in LRET processes, will be dependent on the distance between the donor (UCNPs), and the $[(ppy)_2Ir(dcbpy)]^+PF_6^-$-AuNP conjugates as energy acceptors.

3.3.1 Morphological Characterization

For the donor nanostructures, PSA nanoparticles were synthesized from their corresponding monomers. The Transmission Electron Microscopic (TEM) (Figure 3.1) shows monodispersed spheres with an average size of 300 nm.

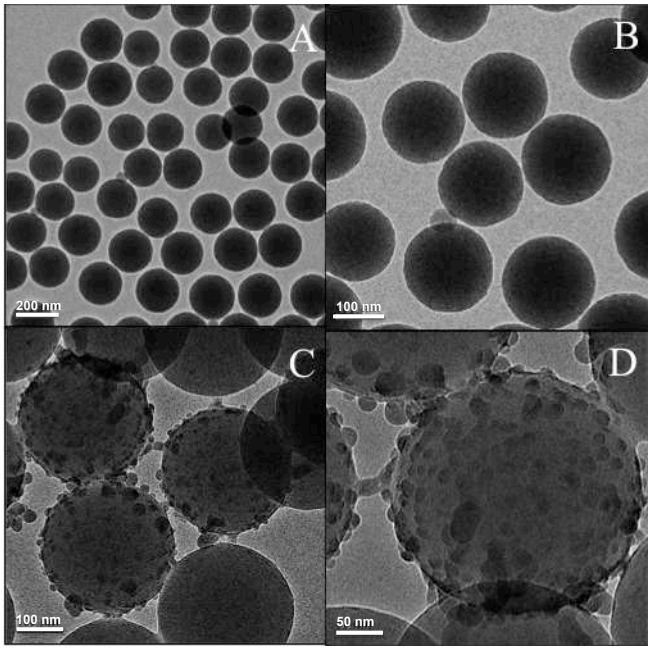

Figure 3.1 TEM images of A) The as synthesized polystyrene-*co*-acrylic acid (PSA) nanoparticles, B) Silica coated PSA NPs (PSA/SiO_2), C) $NaYF_4$:Tm^{3+}/Yb^{3+} tagged PSA/SiO_2 nanoparticle D) HRTEM of $NaYF_4$:Tm^{3+}/Yb^{3+} tagged PSA/SiO_2 nanoparticle.

Small sized $NaYF_4$:Tm^{3+}, Yb^{3+} UCNPs were then synthesized through a thermal decomposition method as described by Boyer *et al*. [24]. The TEM image shows that the synthesized $NaYF_4$:Tm^{3+}, Yb^{3+} UCNPs were cubic in shape and that the average diameter of the cubic phase nanoparticles was approximately 20 nm. The XRD pattern of the nanocrystals (Figure 3.2) against the standard (JCPDS:06-0342) confirmed the cubic phase of the nanoparticles and the positions of the peaks in the XRD with reference to the standard are in excellent correlation thereby confirming the absence of any other phases or impurities. The intensity of the peaks on XRD confirmed the highly crystalline nature of the as-synthesized UCNPs. To confirm the particle size TEM measurements were made and the average crystallite size of the nanoparticles was calculated according to Scherrer's equation. $D = K\lambda/\beta \cos\theta$; where; K = 0.89, D is the crystallite size (in nm), λ is the wavelength of Cu Kα radiation, β is the corrected half-width of the diffraction peak and θ is the Bragg's diffraction peak angle.

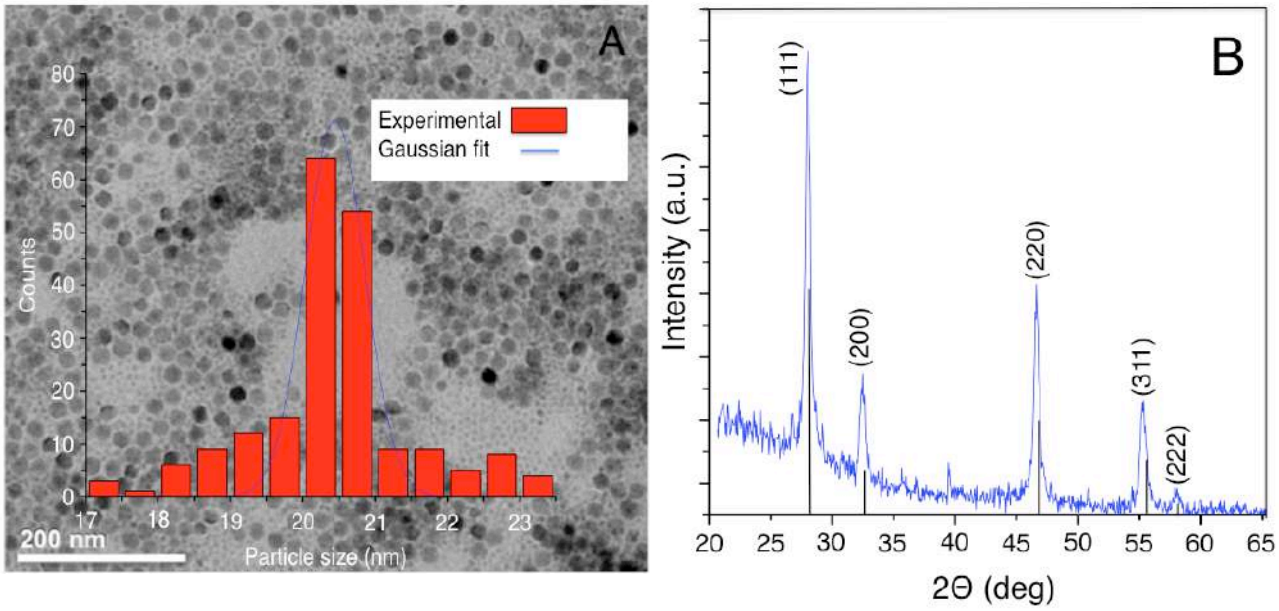

Figure 3.2 TEM (A) and XRD (B) analysis of as-synthesized $NaYF_4$:Tm^{3+}, Yb^{3+} UCNPs.

According to Scherrer's equation, the average crystallite size of the upconversion nanocrystals was found to be 20 nm, which is in excellent agreement with the TEM results. The hydrophobic oleate-capped UCNPs were rendered hydrophilic through a ligand exchange procedure using the hydrophilic citrate ligand. Subsequently, the

hydrophilic UCNPs were then incubated with PSA/SiO_2 nanostructure to form the nanohybrid PSA/SiO_2/UCNPs material (Figure 3.1 C, D).

3.3.2 Surface Characterization

The surface of the composite material was then grafted with (3-Glycidyloxypropyl)trimethoxysilane (GPTMS) to endow it with epoxy functional groups for ssDNA conjugation at a later stage. The surface functionalization of this composite material has also been confirmed using FTIR spectroscopy (Figure 3.3). The analysis for the parent PSA nanoparticles was performed, and various peaks were observed. Specifically, the peak at 3078 cm^{-1} was attributed to the aromatic CH stretching vibration while the intense sharp peaks at 1483 cm^{-1}, 1498 cm^{-1} and 1597 cm^{-1} were ascribed to the aromatic C-C stretching frequencies. Following the growth of silica, these intensities were observed to be considerably weaker for the PSA/SiO_2 nanoparticles. Moreover, peak broadening was observed between 1000 cm^{-1} and 1250 cm^{-1} and was due to the extensive silica coating on the surface of PSA nanoparticles. The Si-OH stretching vibration has been confirmed by the peak at 978 cm^{-1}.

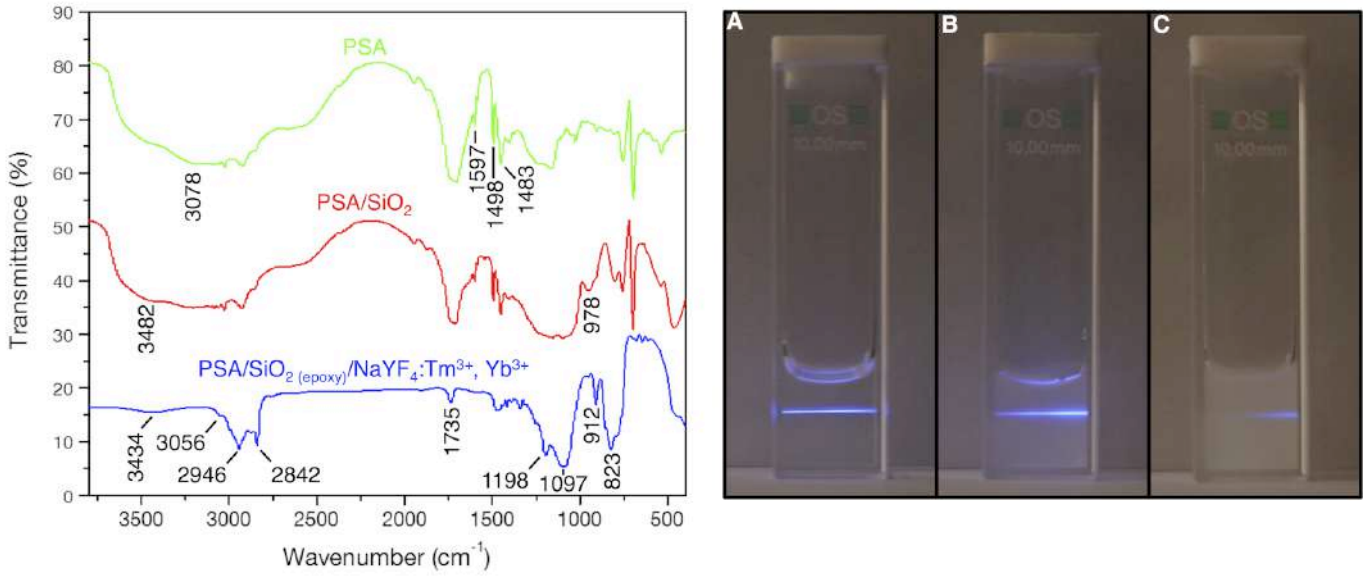

Figure 3.3 Left: FTIR spectra of PSA nanoparticles, PSA/SiO_2 and PSA/$SiO_{2\ (epoxy)}$/$NaYF_4$:Tm^{3+}, Yb^{3+}; Right: Optical upconversion emission images of (A) as-synthesized $NaYF_4$:Tm^{3+},Yb^{3+} in hexane, (B) citrate stabilized $NaYF_4$:Tm^{3+},Yb^{3+} in water, (C) $NaYF_4$:Tm^{3+},Yb^{3+} decorated PSA/SiO_2 nanohybrid.

As stated previously, the hydrophobic $NaYF_4$:Tm^{3+}, Yb^{3+} UCNPs were rendered hydrophilic using the citrate ligand to assemble the hybrid structure. The final

$PSA/SiO_{2(epoxy)}/NaYF_4{:}Tm^{3+}$, Yb^{3+} (citrate stabilized) structure was analyzed using FTIR spectroscopy and peaks at 2842 cm^{-1} and 2946 cm^{-1} confirmed the C-H stretching vibrations of the citrate-capped UCNPs present on the PSA/SiO_2 nanohybrids. Two characteristic absorptions of the epoxide ring, owing to the subsequent GPTMS functionalization, were also observed. The first one at 912 cm^{-1} was attributed to the C-O deformation of the epoxide group while the second band, located at 3056 cm^{-1}, was attributed to the C-H stretching of the methylene group of the epoxy ring. The peak at 1735 cm^{-1} was due to the carbonyl stretching vibration of the carboxyl group of citric acid and the peaks at 1097 cm^{-1} and 1198 cm^{-1} were associated with the symmetrical and asymmetrical stretching vibrations respectively of the citric acid carboxylic functional groups bound to the surface of the UCNPs. The peak at 823 cm^{-1} was attributed to the $Si\text{-}O\text{-}CH_3$ stretching vibration from the GPTMS reagent for epoxy functionalization. The successful deposition of the UCNPs on the surface of $PSA@SiO_2$ has been confirmed by the EDX and XPS spectra as shown in Figure 3.4. Both EDX and XPS identified all the Ln^{3+} dopants at the surface of the nanohybrid.

In another synthesis, the $[(ppy)_2Ir(dcbpy)]^+PF_6^-$ complex was prepared and functionalized on the surface of AuNPs using 4-aminobenzenethiol (4-ABT) as a linker. These $[(ppy)_2Ir(dcbpy)]^+PF_6^-$-AuNP conjugates and the as-prepared PSA/SiO_2/UCNP hybrid structure were linked through the probe ssDNA sequence as described in the experimental section.

Upconversion in thulium ions is a third order process [25] (at least, three excitation NIR photons are needed to emit one high energy blue photon). Therefore, to have a good signal/noise ratio of the luminescence intensity, we increased the amount of UCNPs on the donor side of the sensor. The use of PSA/SiO_2/UCNPs nanohybrids was considered to be an attractive option due to their excellent optical properties, biocompatibility, as well as the available large surface area, which makes it possible for the development of real-time analysis of multiple analytes with multimodal optical probes.

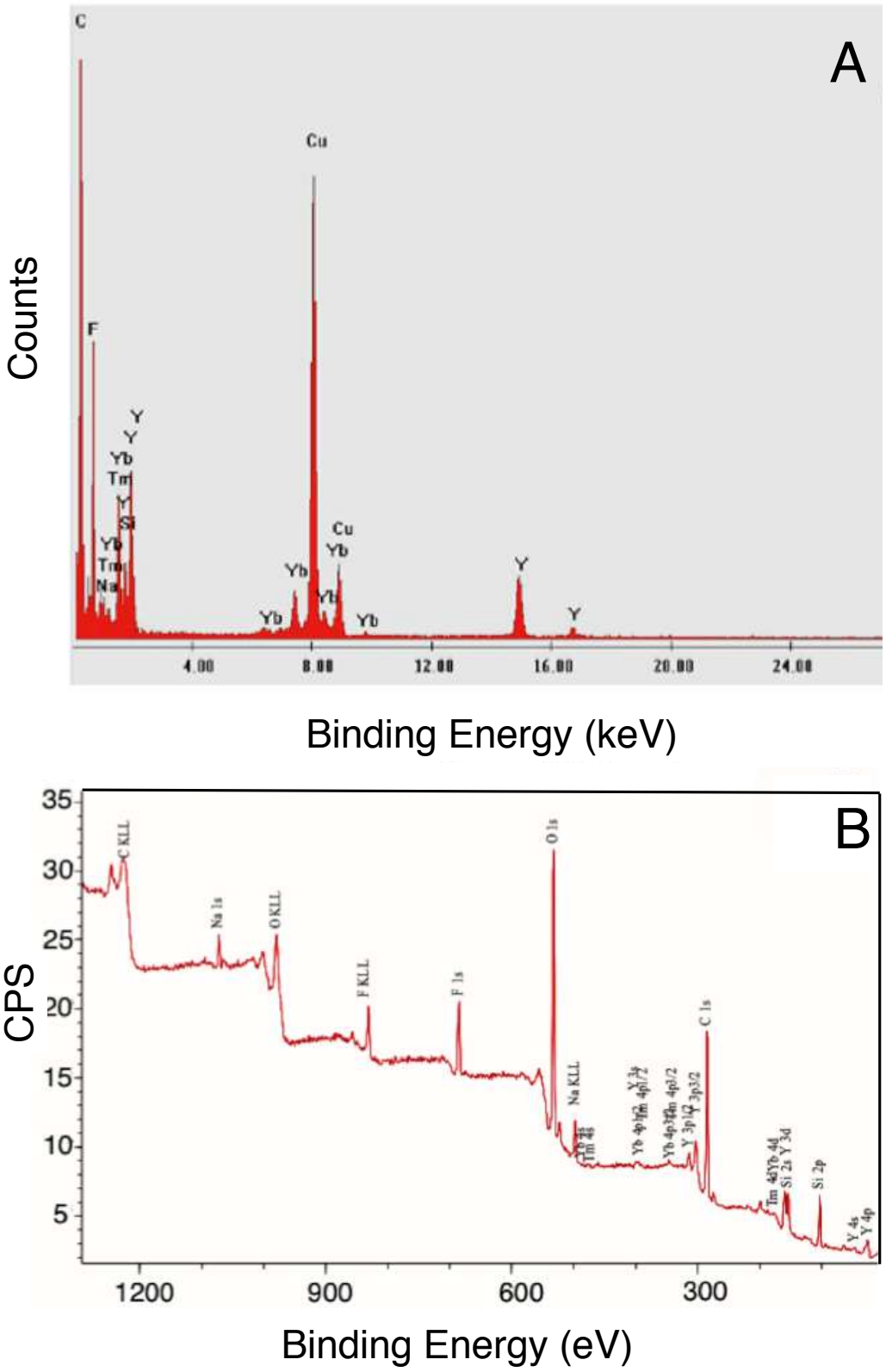

Figure 3.4 Representative (A) EDX and (B) XPS of $NaYF_4$:Tm^{3+}, Yb^{3+} decorated PSA/SiO_2 nanoparticles. Both EDX and XPS confirmed the presence of dopant ions (Tm^{3+}, Yb^{3+}) of the $NaYF_4$ host crystal lattice on the PSA/SiO_2 nanoparticles.

This nanohybrid also acts as a platform for biomolecular reaction to take place on its surface. We used $[(ppy)_2Ir(dcbpy)]^+PF_6^-$ anchored AuNPs as effective quenchers in the LRET-based optical detection since the Ir metal complex on the surface of AuNPs offers good stability and biocompatibility. The presence of carboxyl functional groups on the $[(ppy)_2Ir(dcbpy)]^+PF_6^-$ complex makes it water soluble and thus amenable to bioconjugation. The carboxyl functional groups of the $[(ppy)_2Ir(dcbpy)]^+PF_6^-$ complex was attached to the $–NH_2$ end of the 4-ABT using EDC-NHS conjugation chemistry and its –SH end was directly attached to the surface of the AuNPs. To synthesize the nanohybrid, AuNPs were first synthesized and subsequently attached to the 4-ABT thiol linker. The UV-Vis absorption spectrum of the thiolated AuNPs showed a red shift with absorption maximum centered at 544 nm thus confirming the attachment of 4-ABT linker molecule and the Ir complex on the AuNP surface [26] (Figure 3.5A). Attachment of the Ir complex on the surface of AuNPs through the 4-ABT thiol linker molecule through EDC/NHS conjugation chemistry was also confirmed by the X-ray photoelectron spectroscopy (XPS) and UV-visible absorption measurements. Investigation of XPS spectrum (Figure 3.5B) showed the presence of all the elements from the Ir complex at their respective binding energy values. On the other side of the nanoparticle assembly the available epoxy functional groups on the surface of the UCNP decorated PSA/SiO_2 nanohybrids were attached to the amino end of the probe ssDNA sequence and its thiol end was connected to the $[(ppy)_2Ir(dcbpy)]^+PF_6^-$ modified AuNP leading to the formation of $PSA/SiO_2/NaYF_4{:}Tm^{3+},Yb^{3+}$//*ss*DNA//$[(ppy)_2Ir(dcbpy)(4\text{-}ABT)_2]$/AuNP. The synthesized AuNPs possess a plasmon resonance peak at 520 nm (Figure 3.5A, black solid line). When the AuNPs were decorated with $[(ppy)_2Ir(dcbpy)]^+PF_6^-$ complex, the plasmon resonance of the $[(ppy)_2Ir(dcbpy)]^+PF_6^-$-AuNP conjugates showed a red shift and the entire absorption spectrum extended from 500 to 800 nm with an absorption maximum appearing at above 700 nm (Figure 3.5A, blue line).

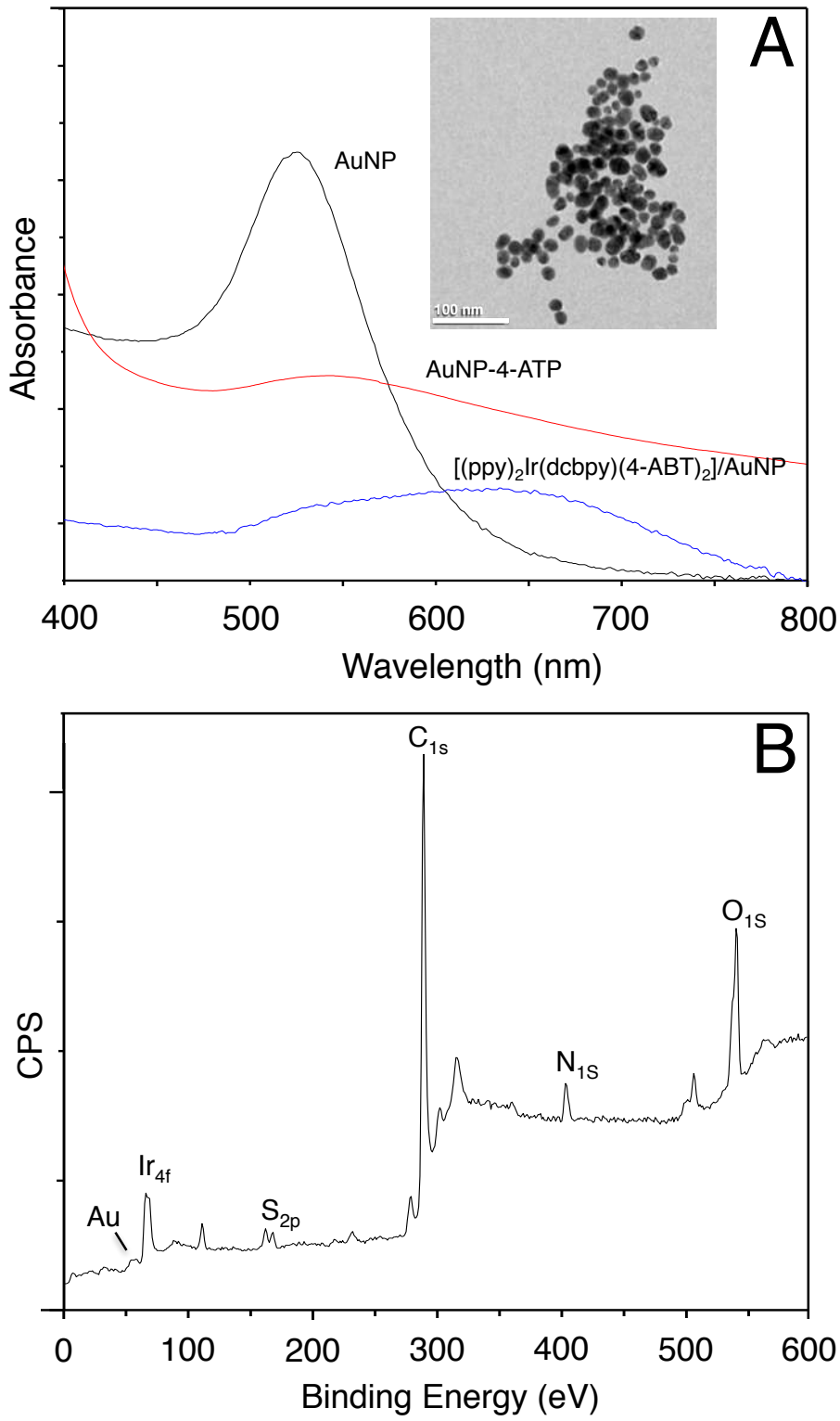

Figure 3.5 (A) Comparison of UV absorptions of AuNPs, 4-ABT modified AuNP and Ir(III) attached AuNPs through thiol linker 4-ABT (inset: TEM of AuNPs) and (B) XPS of Ir (III) decorated AuNPs through 4-ABT linker.

3.3.3 Photophysical Characterization

The as-synthesized Ir complex showed a strong absorption in the UV with an absorption maximum at the 290 nm due to $\pi \rightarrow \pi^*$ transition and a shoulder peak at 380nm due to the metal-ligand charge transfer (MLCT) transition (shown below). Upon UV excitation at 360 nm the Ir complex showed intense reddish orange emission at 620 nm (Figure 3.6).

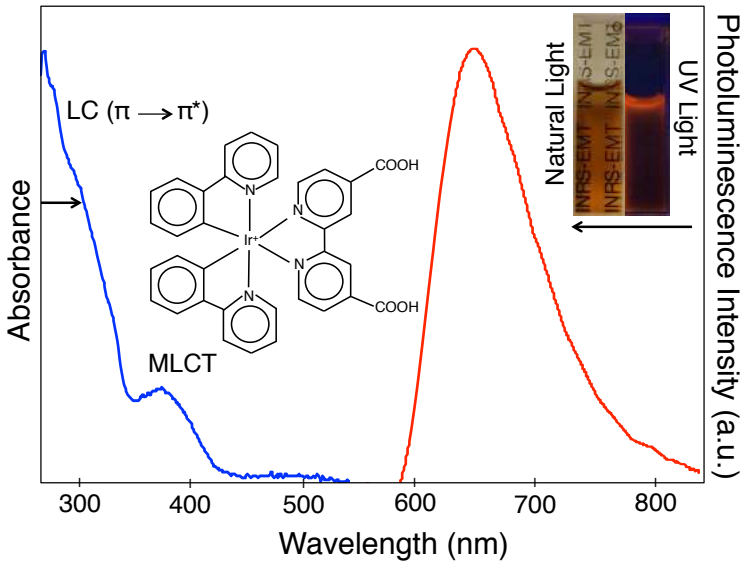

Figure 3.6 Photophysical properties of the synthesized Ir complex, $[(ppy)_2Ir(dcbpy)]^+PF_6^-$ (the structure and optical images of Ir complex under natural and UV light are shown in the inset).

However, when immobilized on the surface of AuNPs, the Ir complex showed a broad absorption from 300 to 800 nm, making $[(ppy)_2Ir(dcbpy)]^+PF_6^-$/AuNP conjugates excellent quenchers for LRET-based optical detection. LRET biosensor based on UCNPs, offers an additional advantage: instead of directly quenching the probe signal, in this case, the blue emission, it would affect the base of the upconverting process, thus reinforcing the separation between light coming from the donor and possible emissions coming from the acceptor. The presence of a large number of conjugated double bonds in the cyclic aromatic ligands in the Ir complex on the surface of the AuNPs promotes the multiphonon relaxation process at the intermediate levels in the upconversion mechanism and hence quenches more effectively the visible emission of the donor UCNPs.

3.3.4 Luminescence Resonance Energy Transfer and ssDNA Sensing

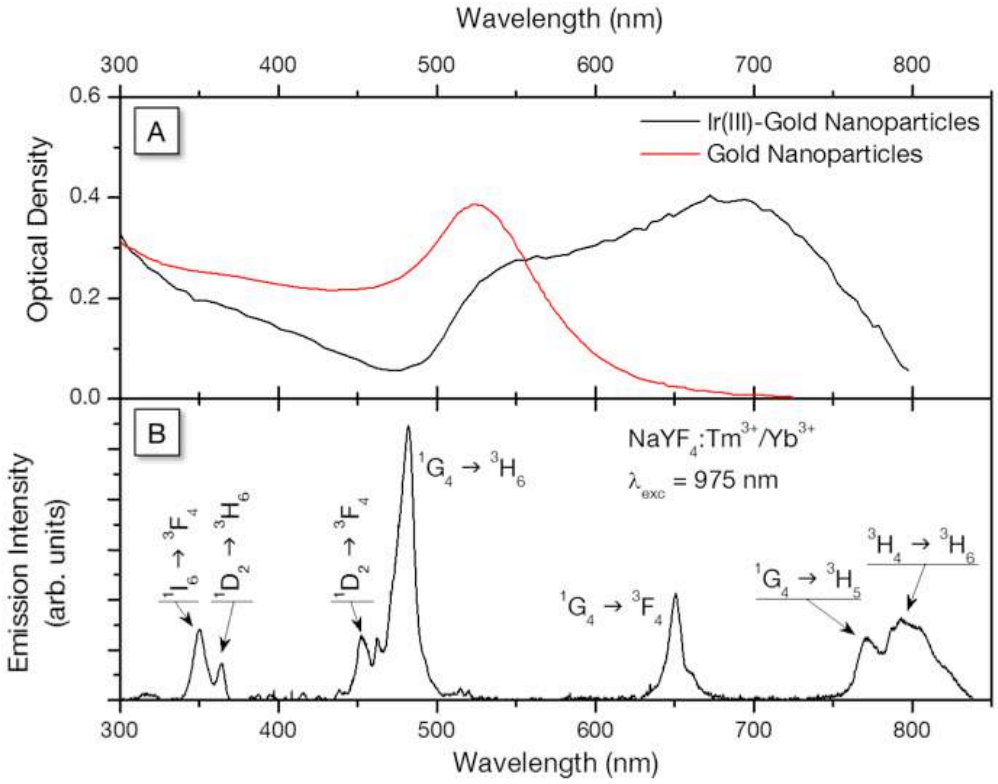

Figure 3.7 (A) UV-Vis absorption spectrum of the AuNPs (red line) and Ir complex $[(ppy)_2Ir(dcbpy)(4\text{-}ABT)_2]$ immobilized on AuNPs (black line). (B) Upconversion emission spectrum of $NaYF_4$:Tm^{3+}, Yb^{3+} in hexane with corresponding energy level transitions following excitation with 975 nm.

The various energy level transitions (Figure 3.7B) involved within the UCNPs overlap with the Ir(III) anchored AuNPs making it an excellent quenching material for LRET technique. The quenching of the visible emission from $NaYF_4$:Tm^{3+}, Yb^{3+} by the Ir(III)-AuNP conjugates has been possible via two different processes such as radiative and non-radiative. In the radiative energy transfer (re-absorption), the photons emitted by the UCNPs at each wavelength are absorbed by the quencher. Thus, this process takes place at every wavelength where the UCNPs are emitting (Figure. 3.7B), and the Ir(III) decorated AuNPs are absorbing (Figure. 3.7A).

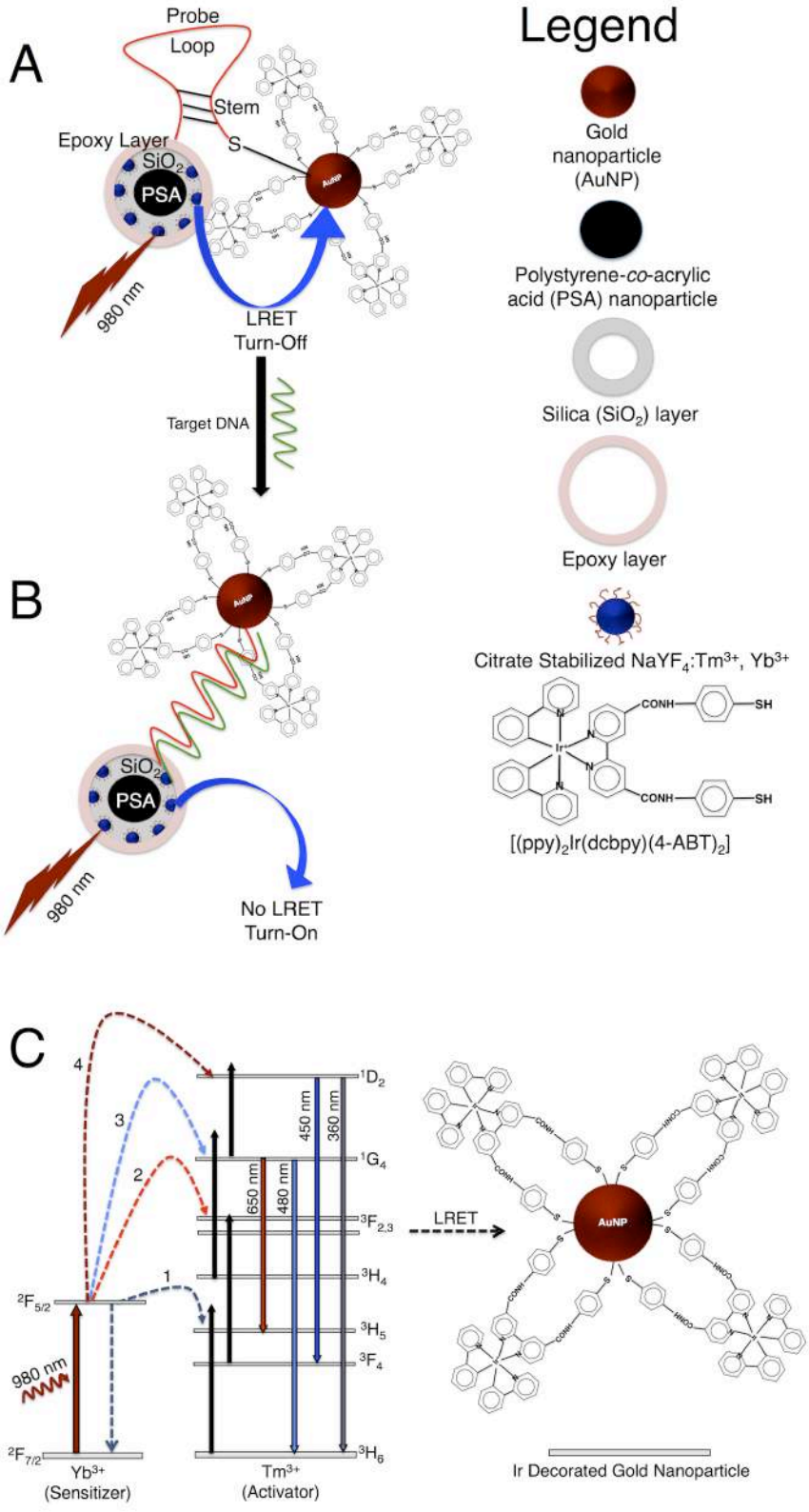

Scheme 3.1 (A) and (B) Proposed LRET-based detection of *ss*DNA using UCNP decorated PSA/SiO_2 nanohybrids, and Ir(III)-AuNPs and (C) Plausible luminescent resonant energy transfer from UCNP to Ir decorated AuNP.

On the other hand, the non-radiative energy transfer is an exchange interaction that takes place faster than the emission of photons by the UCNPs. Consequently, it will take place when the UCNPs (donors) and the quencher (acceptor) transitions are characterized by the same energy.

It is evident that broadening of absorption of the quencher resulted due to the surface functionalization of AuNPs by the Ir complex. The broadening of the absorption spectrum of the quencher is a favorable characteristic feature in two ways. Firstly, from the radiative energy transfer point of view, more emissions are affected by the quencher. Secondly from the non-radiative point of view, absorption of the Ir decorated AuNPs is now resonant both with $^3F_{2,3} \rightarrow {}^3H_6$ and $^1G_4 \rightarrow {}^3F_4$ transitions of the Tm^{3+} ions. As a result, such acceptors would likely interrupt the usual upconverting path, consequently quenching the visible emissions related to the higher-energy excited states. The principle of the LRET based nanosensor is shown in Scheme 3.1A, B. The scheme showed a hairpin shaped molecular beacon with an UCNP-decorated PSA/SiO_2 nanohybrids as donor at one end and the [$(ppy)_2$Ir(dcbpy)(4-ABT)$_2$]/AuNPs conjugate as an acceptor at the other end. The presence of Ir(III) modified AuNPs quenches the emission intensity of UCNPs (turn-off) when excited at 980 nm (Scheme 3.1A). When the complementary DNA sequence is added to the complex, both nanoparticle assemblies moved further due to the formation of elongated hybridized double helical structure. In turn, the probability of luminescent energy transfer between them is reduced, thereby restoring the emission intensity (turn-on) of the donor UCNPs (Scheme 3.1B). To calibrate the sensitivity of the prepared complex, the luminescence emission of the samples with the same concentration of probe DNA complexes were titrated against different concentrations of target DNA down to 1 pM. The addition of negative control to the probe molecular beacon connected nanohybrids, PSA/SiO_2 nanoparticles/ $NaYF_4$:Tm^{3+},Yb^{3+}//*ss*$DNA_{(Probe)}$// Ir(III)-AuNP showed almost no change in the upconversion emission intensity thus confirming the sensitivity of our method (Figure 3.8D). The emission intensity (Figure 3.8A) is proportional to the concentration of target DNA sequence in the sample, as a consequence of hybridized elongated double-helical DNA structure which resulted in the increased distance between the [$(ppy)_2$Ir(dcbpy)(4-ABT)$_2$]/AuNP and the UCNP decorated PSA/SiO_2 nanohybrids. It is

clear from the Figure 3.8A that the high signal/background contrast in the whole concentration range is considered, especially taking into account that no background or baseline has been removed from the spectrum. This clearly demonstrates the reliability and simplicity of the proposed technique. For calibration purposes, the area under the emission bands (Figure 3.8A) has been plotted against the target DNA concentration (Figure 3.8B). From Figure 3.8B, it is evident that both magnitudes are related through a linear dependency in a semi-logarithmic plot, which provides the sensitivity curve for the ssDNA nanobiosensor. The fact that the dependency between both magnitudes is not linear can be attributed to the non-linear nature of upconversion processes. In particular, for Tm^{3+}, Yb^{3+} co-doped UCNPs after 980 nm excitation, the upconversion mechanism necessary to emit blue light is at least a third order process. In the proposed quenching strategy, the luminescence is being blocked from the NIR-emitting level that works as an intermediate step for the upconversion, instead of directly quenching the blue emission. This indicates the sensitivity of the biosensor, i.e. the difference in intensity for two different concentrations ($\Delta I/\Delta[DNA]$), will be higher at lower concentrations. Figure 3.8C showed an excellent linear coefficient value of the nanohybrid against target DNA concentration ranging from nanomolar to picomolar confirming the sensitivity of the nanosensor. To confirm the selectivity of our nanosensor, we titrated the probe DNA conjugated nanohybrids with a single base mismatch. Measurement of upconversion emission proved that the blue emission remained almost quenched (Figure 3.8D) upon excitation at 980nm thus confirming the highly selective nature of the proposed nano-biosensor down to 1pM.

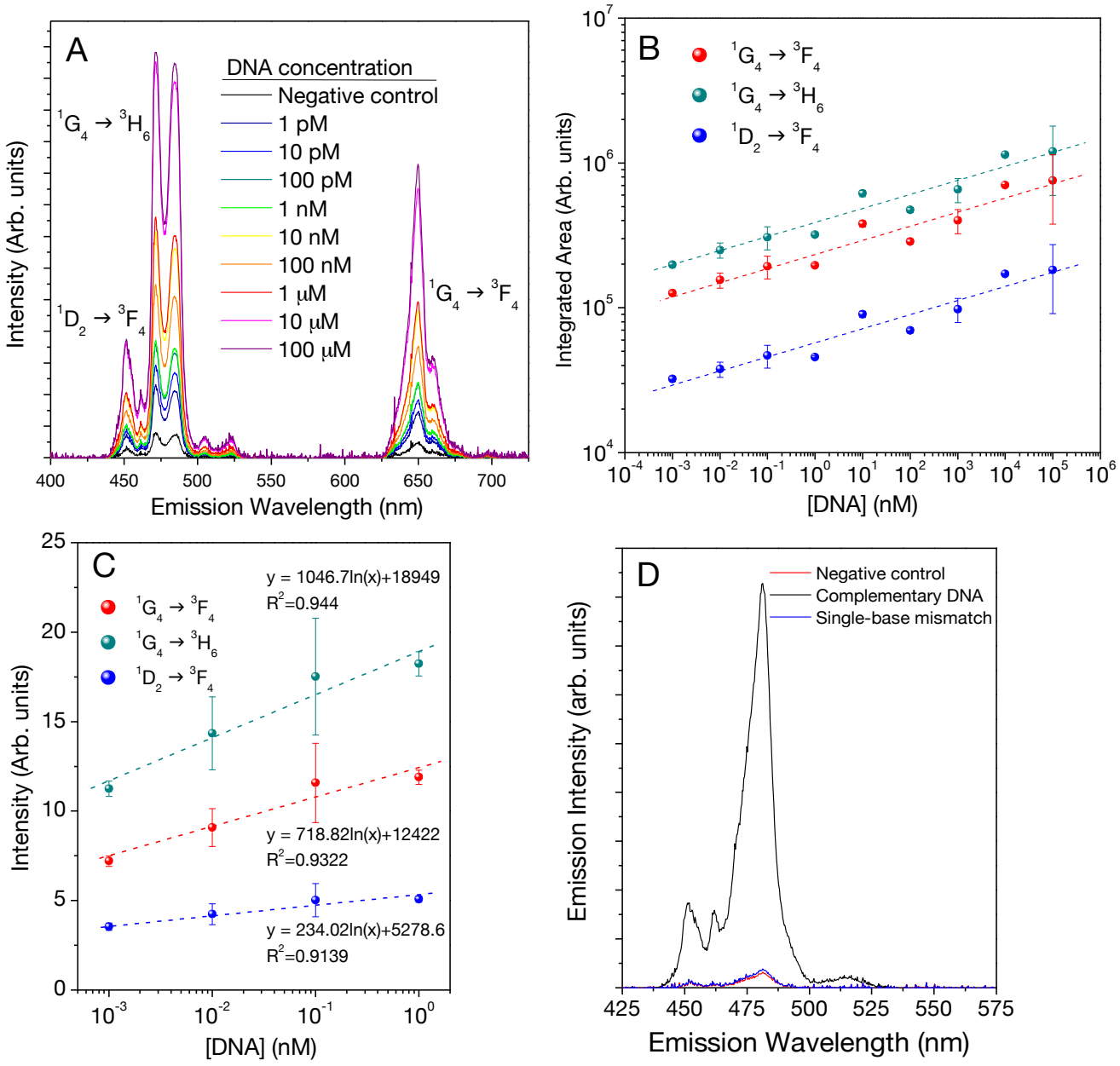

Figure 3.8 (A) Integrated area under the blue emission vs. concentration of complementary DNA sequence (B) Upconversion spectra in the blue region of the sensor upon adding different concentrations of target *ss*DNA sequence. (C) Linear dependence of emission intensity at the lower target DNA concentration levels. (D) Comparison of luminescent emission intensities of complementary, negative control and single base mismatch DNA sequences.

Thus, in that range where the signal is normally weaker, even for small target DNA changes, the difference in luminescence intensity will be considerably high. Initial optical measurements showed non-linear behavior for the higher target DNA concentrations. This may be attributed to the precipitation of the nanohybrids upon hybridization with the target DNA (Figure 3.9E). At higher concentrations, DNA hybridization leads to induced aggregation, which resulted in the precipitation (shown below).

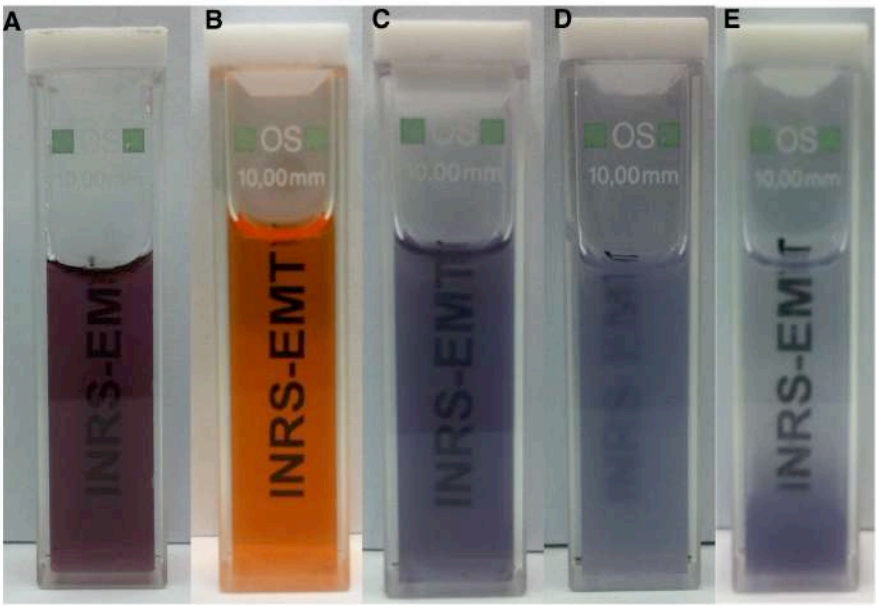

Figure 3.9 Optical images of (A) as-synthesised AuNPs, (B) $[(ppy)_2Ir(dcbpy)]^+$ PF_6^- in Ethanol, (C) PSA/SiO_2 $/NaYF_4{:}Tm^{3+},Yb^{3+}//ssDNA_{(Probe)}//Ir(III)$-AuNP, (D) PSA/SiO_2 $/NaYF_4{:}Tm^{3+},Yb^{3+}//dsDNA_{(Probe+Complementary)}//Ir(III)$-AuNP, before precipitation, (E) $PSA/SiO_2/NaYF_4{:}Tm^{3+},Yb^{3+}//dsDNA_{(Probe+Complementary)}//Ir(III)$-AuNP after precipitation.

3.4 Experimental Section

3.4.1 Chemicals

Styrene (St) and acrylic acid (AA) were purchased from Aldrich and distilled under reduced pressure. Potassium persulfate (KPS) was recrystallized from deionized water before use. Aqueous ammonia solution ($NH_3{\cdot}H_2O$, 28%), 4-aminobenzenethiol (4-ABT > 98%), tetraethoxysilane (TEOS >98%), anhydrous ethanol, and 3-aminopropyltriethoxysilane (APTES), (3-Glycidyloxypropyl)trimethoxysilane (GPTMS),

and chloroauric acid tetrahydrate ($HAuCl_4 \cdot H_2O$), 2-phenylpyridine, $IrCl_3 \cdot 3H_2O$, 2-ethoxyethanol, 2,2'-bipyridine-4,4'-dicarboxylic acid, sodium acetate, ammonium hexafluorophosphate, trisodium citrate, were purchased from Aldrich. Y_2O_3, Yb_2O_3, Tm_2O_3, trifluoracetic acid, sodium trifluoroacetate, oleic acid, octadecene, citric acid were obtained from Alfa Aesar. Triton X-100 (TX-100), n-hexanol, methanol, hexane, toluene, ethanol, dichloromethane, acetone, anhydrous N,N-dimethylformamide (DMF), ammonia solution (25%, w/w), 1-ethyl-3-(3-dimethylaminopropyl) carbodiimide hydrochloride (EDC), N-hydroxysulfosuccinimide (sulfo-NHS), and succinic anhydride (>97%) were purchased from Fluka (USA). Ultrapure water (Millipore) of resistivity greater than 18.0 MΩ cm was used in all experiments. All chemicals were used as received unless specified.

All chemicals were used as received unless specified. DNA oligonucleotides with a concentration of 100 nM were purchased from Integrated DNA Technologies (IDT), and the sequences are listed as follows:

Sequence Description: B1-NH_2-thiol

Sequence: 5'- /5AmMC6/GC GAG AAG TTA AGA CCT

ATG CTC GC/3ThioMC3-D/ -3'

Complementary: 5'- CAT AGG TCT TAA CTT -3'

Single-base mismatch: 5'- CAT AG*T* TCT TAA CTT -3'

Negative control:5'- AAA AAA AAA AAA AAA -3'

The stem DNA sequences have been underlined. Single-base mismatch is *italicized*.

3.4.2 Instrumentation

The FTIR was recorded on a Thermoscientific Nicolet Spectrometer using FTIR grade KBr as background. Transmission Electron Microscopy (TEM) images were obtained with a Philips CM200 High-Resolution TEM (HRTEM). The morphology and size distribution of the UC, gold and polymer nanoparticles were observed on carbon-coated copper grid. Prior to analysis, a 10 mg UCNP sample was dispersed in 10 g of hexane and sonicated for 1h. A drop of the resulting solution was evaporated on a formvar/carbon film supported on a 300 mesh copper grid (3 mm in diameter). For the

PSA, PSA/SiO_2 and UCNP tagged PSA/SiO_2 nanoparticles respective ethanolic solutions have been dropped on the TEM grid.

^{1}H NMR spectra were recorded on a Bruker 400 MHz instrument using $CDCl_3$ solvent. ^{13}C NMR spectra were recorded on a Varian S-500 instrument at 125 MHz using deuterated acetone solvent. XPS was recorded on a VG Escalab 220i XL instrument equipped with 6 channeltrons using unmonochromated Mg K X-ray source (1253.6eV). The phase identification was done from the X-Ray Diffraction (XRD) patterns recorded using a Bruker D8 Advance Diffractometer for powder samples with Cu KR radiation at λ = 0.154 nm operating at 45kV and 40mA.

The upconversion emission spectra were obtained using a Thorlabs fiber-coupled 975 nm laser diode (maximum power of 330 mW) as the excitation source. For the OA-capped hydrophobic UCNPs the sample (1 wt% in hexane) were placed in 10 mm path-length quartz cuvettes (Hellma, QS). For PSA, PSA/SiO_2 and UCNP doped PSA/SiO_2 nanoparticles, DNA tagged UCNPs doped nanohybrids their ethanol solutions were used. The emission light was collected by a lens in a 90^o configuration, and then transferred to a spectrophotometer (Avaspec-2048L-USB2) using an optical fiber. All along the experiments, the cuvette had been placed in a fixed sample holder that guarantees a comparable laser focalization over the sample for every sample, and thus, the possibility to compare intensities between different samples. To check that, every spectrum has been recorded removing and placing the same sample again, demonstrating an experimental error generally lower than 5%.

3.4.3 Synthesis of precursor complex $[(ppy)_2Ir(\mu\text{-}Cl)]_2$ The Ir complex was synthesized according to the literature procedure with a slight modification [27]. Briefly, a mixture of 2-phenylpyridine (0.34 g, 2.2 mmol), $IrCl_3 \cdot 3H_2O$ (0.34g, 1 mmol) in a mixed solvent of 2-ethoxyethanol (15 mL) and water (5 mL) was stirred under N_2 at 120 ^{o}C for 20 h. The precipitate was then cooled to room temperature and collected by filtration and washed with water, ethanol, acetone respectively, and subsequently dried under vacuum to give the $[(ppy)_2Ir(\mu\text{-}Cl)]_2$ dimer complex.

^{1}H NMR (500 MHz, $CDCl_3$) δ: 9.26 (d, J = 5.5 Hz, 1H), 7.96 (d, J = 8 Hz, 1H), 7.82 (t, J = 7.5 Hz, 1H), 7.58 (d, J = 7.5 Hz, 1H), 6.85 (m, 2H), 6.63 (t, J = 7.5 Hz, 1H), 5.89 (d, J

= 8 Hz, 1H). ^{13}C NMR (125 MHz, acetone-d6) δ: 168.2 151.8 143.5 144.1 135.7 132.4 129.7 126.8 121.8 121.6 119.8 ppm. Calcd for $C_{44}H_{32}Cl_2Ir_2N_4$: C, 49.29; H, 3.01; N, 5.23. Found: C, 49.32; H, 3.07; N, 5.24. ESI-MS: 1072 [M^+]

3.4.4 Synthesis of $[(ppy)_2Ir(dcbpy)]^+ PF_6^-$ $[(ppy)_2Ir\ (\mu\text{-}Cl)]_2$ (0.21 g, 0.2 mmol) was prepared as a solution in dichloromethane (15 mL) and added to a suspension of 2,2'-bipyridine-4,4'-dicarboxylic acid (0.098 g, 0.4 mmol) in methanol (20 mL). The reaction mixture was then heated to reflux with stirring for 4 h. To this solution, sodium acetate (excess) in methanol (5 mL) was added, and the mixture was stirred for a further 45 min. The solvent was then removed under reduced pressure, hydrochloric acid (1 M, 10 mL) was added, and the suspension was stirred for 20 min. The product was then filtered, washed with water (2 × 25 mL), vacuum dried, and the solid was then dissolved in methanol. A saturated solution of ammonium hexafluorophosphate in methanol (5 mL) was then added, and the mixture was stirred for a further 45 min. The solvent was removed under reduced pressure, and the residue was extracted with dichloromethane and filtered. The solvent was removed under reduced pressure to yield $[(ppy)_2Ir(dcbpy)]^+ PF_6^-$ as a dark-red powder. The crude product was flash chromatographed on silica gel using CH_2Cl_2 as an eluent to afford the desired Ir(III) complex. (0.16 g, 69%).

^{1}H NMR (500 MHz, $CDCl_3$) *δ*: 6.32 (d, *J* = 5.9 Hz, 2H), 6.24 (t, *J* = 7.22 Hz, 2H), 6.54 (m, 2H), 6.64 (t, *J* = 7.46Hz, 2H), 7.22 (t, *J* = 7.34Hz, 2H), 7.52 (d, *J* = 7.50Hz, 2H), 7.48 (t, *J* = 7.50Hz, 2H), 7.58 (t, *J*=7.56Hz, 2H), 7.83(m, 2H), 8.46 (d, *J* = 5.52 Hz, 2H), 9.38 (s, 2 H). ^{13}C NMR (125 MHz, acetone-d6) δ: 121.08, 123.85, 124.77, 125.77, 126.07, 129.29, 131.53, 132.6, 139.91, 142.41, 145.05, 150.59, 150.82, 152.83, 157.77, 165.56, 168.65 ppm. mp (^{o}C): 194.5 Calcd for $C_{34}H_{24}F_6N_4O_4IrP$: C, 45.87; H, 2.69; N, 6.31. Found: C, 46.13; H, 2.84; N, 6.74. IR (KBr): *v* 2934 (s, OH), 1726 (s, CO), 852 (s, PF) cm^{-1}. ESI-MS: 745 [M^+]

3.4.5 Synthesis of activated $[(ppy)_2Ir(dcbpy)]$–Sulfo-NHS ester. EDC (0.17g, 1.11 mmol) and Sulfo-NHS (0.119 g, 1.035 mmol) were dissolved in acetonitrile (2 mL) with stirring and cooled in an ice bath. The $[(ppy)_2Ir(dcbpy)]^+PF_6^-$ solution in acetonitrile (100 μL, 4.3 x 10^{-4} M) was added to the EDC-NHS mixture. The solution was stirred for 3 h at

room temperature to form the $[(ppy)_2Ir(dcbpy)]$-sulfo-NHS ester. This ester (2.69×10^{-5} M) was kept at 4 ^{o}C for further use.

3.4.6 Synthesis of AuNPs. Prior to the synthesis of AuNPs, all glassware used was cleaned in a bath of freshly prepared 3:1 $HCl:HNO_3$ and rinsed thoroughly with water before using. Typically, 99 mL triple distilled water and 1 mL 1% $HAuCl_4$ solution were added into a round-bottom flask equipped with a reflux condenser under vigorous stirring. The flask was subsequently incubated in an oil bath to reflux under stirring. Under the boiling solution, 5 mL of 1% trisodium citrate solution was quickly added to the flask, and the reaction was allowed to reflux for another 20 min. The color of the solution changed from pale yellow to deep red and the solution was cooled to room temperature and then stored at 4 ^{o}C in the refrigerator for further use. The average diameter of the synthesized gold nanoparticle was 24nm.

3.4.7 Attachment of activated $[(ppy)_2Ir(dcbpy)]$-NHS ester to AuNPs to form Ir(III)-gold nanoparticle conjugates. 1 mol of the $(ppy)_2Ir(dcbpy)]$-NHS ester was added to a 2 mol ethanol solution of 4-ABT and the mixture was stirred at room temperature for 2 h resulting in the formation of $[(ppy)_2Ir(dcbpy)(4\text{-}ABT)_2]$. To this mixture, 1 mL of the gold colloid was added and the mixture was stirred for another 2 h for the attachment of the –SH functional group from the 4-ABT linker molecule in the Ir complex on to the surface of AuNPs. The resultant solution was then centrifuged and the supernatant was removed. The precipitate containing Ir(III)-AuNP conjugates was then washed several times with ethanol and finally dispersed in water for further use.

^{1}H NMR (500 MHz, $(CD_3)_2SO$ δ: 6.6-7.2 (m, Ar-*H*), 2.2 (RCON*H*), 3.2-3.8 (b, Au-S)

3.4.8 Synthesis of poly(styrene-*co*-acrylic acid) (PSA) nanoparticles. PSA nanoparticles were prepared according to the method described here. 1.6 g of styrene, 0.4 g of acrylic acid (AA) and 100 mL of H_2O were added into a three-necked flask, which was equipped with a mechanical stirrer and a condenser. The solution was purged with nitrogen to remove oxygen for 30 min and then heated to 80 ^{o}C. Subsequently, 0.06 g of KPS dissolved in 2 ml of H_2O was injected into the reaction mixture to initiate the polymerization under stirring and this reaction system continued

heating for 10 h. The resulting PSA nanoparticles were washed with ultrapure water by centrifugation several times and then dispersed in water for further use.

3.4.9 Synthesis of PSA/SiO_2 nanostructures. The as-prepared PSA nanoparticles were encapsulated in silica. Typically, PSA nanoparticles were dispersed in a mixture of 9 mL of water, 40 mL of ethanol, and 1 mL of ammonia solution by sonication for 20 min. TEOS was added to the mixture, and the sonication was continued at 0 ^{o}C for another 2 h. The obtained products were washed repeatedly with ethanol and water to eliminate excess TEOS. Finally the sample was dispersed in water for further use.

3.4.10 Synthesis of oleate-capped $NaYF_4$:Tm^{3+}, Yb^{3+} co-doped upconverting nanoparticles (UCNPs). Caution: This high temperature reaction involves liberation of very toxic and corrosive fluoro compounds, hence proper care must be taken and the reaction must be carried out in a well-ventilated fume hood. $NaYF_4$:Tm^{3+}, Yb^{3+} UCNPs were synthesized via the thermal decomposition method reported earlier [24]. Briefly, the metal (Y^{3+}, Tm^{3+} and Yb^{3+}) trifluoroacetates (prepared by reacting Y_2O_3 (1 mmol), Yb_2O_3 (0.27 mmol), Tm_2O_3 (0.005 mmol), and refluxing the corresponding oxides in 50/50 v/v CF_3COOH/H_2O at 80 ^{o}C) were mixed with CF_3COONa (2.5 mmol), oleic acid (20 mL) and 1-octadecene (20 mL). The resulting mixture was heated to 110 ^{o}C with constant stirring under vacuum. After 30 min, the temperature of the mixture was increased to 330 ^{o}C at a rate of 5 ^{o}C per minute under Ar flow. At this final temperature, the mixture remained for 1 h, after which it was allowed to cool to 70 ^{o}C prior to precipitation with absolute ethanol. The nanocrystals were then separated via centrifugation and further purified by dispersing in hexane followed by precipitation with ethanol.

3.4.11 Synthesis of hydrophilic $NaYF_4$:Tm^{3+}, Yb^{3+} UCNPs. The as-synthesized oleate-capped hydrophobic UCNPs were made water dispersible by a ligand exchange method. Briefly, 0.1 g of citric acid was mixed with 10 mL of ethanol. To this, 5 mL of chloroform containing 0.05 g of the oleate-capped UCNPs was added. The mixture was sonicated for 1 h and left stirring overnight at room temperature. The solution was then centrifuged at 8000 RPM for 1 h and the pellet was washed several times with ethanol and water. Finally the citrate-capped UCNPs were dispersed in water for further use.

3.4.12 Synthesis of $NaYF_4$:Tm^{3+}, Yb^{3+} decorated PSA/SiO_2 nanohybrids. 1 mL of Tm^{3+}, Yb^{3+} co-doped hydrophilic $NaYF_4$ UCNPs was added to 1 mL of PSA/SiO_2 nanohybrids in a centrifuge tube. The mixture was incubated at room temperature for overnight. To this resultant sample solution 10 mL of dry ethanol was added and the mixture was sonicated for 1 h. The solution was then centrifuged at 8000 RPM for 20 min and the supernatant was removed. The precipitate containing the $NaYF_4$:Tm^{3+}, Yb^{3+} decorated PSA/SiO_2 nanohybrids was washed with water and dispersed in ethanol.

3.4.13 Surface modification $NaYF_4$:Tm^{3+}, Yb^{3+} decorated PSA/SiO_2 nanohybrids with epoxy groups. GPTMS is a silane-coupling agent and can covalently bind to the surface of silica spheres by condensation of the methoxysilane groups (Si–O–CH_3) and silanol groups (Si–OH) of the silica surfaces. To accomplish this, 15 mg of the $NaYF_4$:Tm^{3+}, Yb^{3+} decorated PSA/SiO_2 nanohybrids were dispersed in 70 mL of ethanol by sonication, and then a 0.1 mL of GPTMS was added to the mixture with magnetic stirring. After the reaction mixture was refluxed for 5 h at 120 ^oC, the resulting product was centrifuged several times with ethanol to remove excess reactants and redispersed in ethanol.

3.4.14 Conjugation of epoxy modified $NaYF_4$:Tm^{3+}, Yb^{3+} decorated PSA/SiO_2 nanohybrids with probe oligonucleotides. 2 mg of the $NaYF_4$:Tm^{3+}, Yb^{3+} decorated epoxy modified PSA/SiO_2 nanohybrids were dispersed in 5.0 mL of 0.1 mol L^{-1} phosphate buffer (pH 7.0) by ultrasonication and a homogenous dispersion was obtained. An amount of 25 mg of succinic anhydride was added to the solution, and then the mixture solution was allowed to react for 2 h under stirring. After reaction, the as-prepared mixture solution was centrifuged and washed with phosphate buffer (pH 7.0), and then re-dispersed in 5.0 mL of 0.05 M Tris-HCl buffer containing 0.02 M NaCl (pH 7.2). 1.2 mg of EDC and 1.8 mg of NHS were added to the solution and the reaction was allowed to react for 30 min under stirring. 50 μL of ssDNA was then added, and the reaction was incubated for 12 h. The resulting solution was centrifuged and washed with 0.05 M Tris-HCl, the particles were re-suspended in 5.0 mL of 0.05 M Tris-HCl buffer containing 0.02 M NaCl (pH 7.2), and therefore the PSA/SiO_2 conjugated with oligonucleotide nanohybrid probe was obtained.

3.4.15 Conjugation of Ir(III)-AuNPs nanohybrid with UCNP-decorated PSA/SiO_2//ssDNA-Probe. The conjugation of Ir(III)-AuNPs with the oligonucleotide was accomplished according to the following procedure. 1.0 mL of the as-prepared Ir(III)-AuNPs was transferred into a microcentrifugation tube and centrifuged for 15 min. The nanohybrids were re-suspended in 1.0 mL of 10 mM phosphate buffer (pH 7.0). 20 mL of the $NaYF_4$:Tm^{3+}, Yb^{3+} decorated PSA/SiO_2//ssDNA-probe was added to the 1.0 mL of Ir(III)-AuNPs dispersoid, and the mixture solution was allowed to react for 16 h at 50 ^oC. Then saline phosphate buffer (10 mM phosphate buffer containing 2 M NaCl, pH 7.0) was added dropwise to the solution to reach a final salt concentration of 0.1 M NaCl, and then the reaction continued for 40 h. The solution was centrifuged and re-suspended several times. After centrifuging, the nanohybrids were dispersed in 10 mM phosphate buffer containing 0.1 M NaCl (pH 7.0), and thus PSA/SiO_2//ssDNA(Probe)//Ir(III)-AuNP were obtained.

3.4.16 DNA hybridization assay for LRET measurements. For the LRET measurements, sample solutions containing 0.05 mg/mL of the PSA/SiO_2//ssDNA(Probe)//Ir(III)-AuNP in phosphate buffer were incubated with different concentrations of target ssDNA sequences at 35 ^oC for 1h. Then LRET upconversion measurements were done on all these solutions at 980 nm excitation.

3.5 Conclusion

In conclusion, we have developed a new LRET-based DNA sensor that uses ssDNA functionalized PSA/SiO_2/UCNPs nanohybrids as the energy donor and water soluble [$(ppy)_2$Ir(dcbpy)$(4\text{-ABT})_2$]-AuNP conjugates as efficient quenchers, and its efficiency has been demonstrated down to the picomolar level. Since our LRET sensor is based on the use of UCNPs the signal contrast has been excellent and offers other advantages such as the absence of autofluorescence and light scattering making it an ideal optical biosensor. Also, the broad separation between the excitation wavelength and acceptor absorption, as well as between acceptor emissions and donor absorptions, eliminates the mixed signals or spectral cross-talk. The efficiency of Tm^{3+}, Yb^{3+} co-doped UCNPs as donors has been demonstrated, and opens the door for the possibility of making multi-channel sensors in combination with other Ln3+s, like the most commonly used Er^{3+} ions. Also the use of PSA nanoparticles that can be easily functionalized with

different donor particles is an advantage in that regard. In addition, the high fluorescence quenching efficiency of $[(ppy)_2Ir(dcbpy)(4\text{-}ABT)_2]$/AuNP conjugates on PSA/$SiO_2$/UCNPs was also shown as the fluorescence is quenched from the root of the upconversion process instead of directly absorbing the emitted light from the UCNPs. Therefore, our results confirmed that PSA/SiO_2/UCNP//$[(ppy)_2Ir(dcbpy)(4\text{-}ABT)_2]$/AuNP conjugates could be an effective tool in a LRET-based assay and could be successfully applied in the development of more efficient optical sensors for the detection of various biomolecules. Our results have also provided a LRET system that is sensitive and simple to use in biological analyses. Further studies may pave the way to extend the applications of this new detection scheme in ultrasensitive multiplexed detection of wide range of biomolecular analytes.

3.6 References

1. Jaiswal, J. K.; Mattoussi, H.; Mauro, J. M.; Simon, S. M. Long-term multiple color imaging of live cells using quantum dot bioconjugates. *Nat. Biotechnol*. **2002**, *21*, 47-51.

2. Medintz, I. L.; Clapp, A. R.; Mattoussi, H.; Goldman, E. R.; Fisher, B.; Mauro, J. M. Self-assembled nanoscale biosensors based on quantum dot FRET donors. *Nat. Mater*. **2003**, *2*, 630-638.

3. Maestro, L.M.; Martín Rodríguez, E.; Vetrone, F.; Naccache, R.; Loro Ramírez, H.; Jaque, D.; Capobianco, J.A.; García Solé, J. Nanoparticles for highly efficient multiphoton fluorescence bioimaging. *Opt. Exp*. **2010**, *23*, 23544-23553.

4. Ju, Q.; Luo, W. Q.; Liu, Y. S.; Zhu, H. M.; Li, R. F.; Chen, X. Y. Poly(acrylic acid) capped Ln^{3+}-doped BaFCl nanocrystals: synthesis and optical properties. *Nanoscale* **2010**, *2*, 1208-1212.

5. Wang, F.; Wang, J.; Liu, X. Direct evidence of a surface quenching effect on size-dependent luminescence of upconversion nanoparticles. *Angew. Chem*. *Int. Ed*. **2010**, *122*, 7618-7622.

6. Wang, F.; Liu, X. Recent advances in the chemistry of Ln^{3+}-doped upconversion nanocrystals. *Chem. Soc. Rev*. **2009**, *38*, 976-989.

7. Louis, U.; Bazzi, R.; Marquette, C.A.; Bridot, J.L.; Roux, S.; Ledoux, G.; Mercier, B.; Blum, L.; Perriat, P.; Tillement, O. Nanosized hybrid particles with double luminescence for biological labeling. *Chem. Mater*. **2005**, *17*, 1673-1682.

8. Wang, L.Y.; Yan, R.X.; Huo, Z.Y.; Wang, L.; Zeng, J.H.; Bao, J.; Wang, X.; Peng, Q.; Li, Y.D. Fluorescence resonant energy transfer biosensor based on upconversion-luminescent nanoparticles. *Angew. Chem. Int. Ed*. **2005**, *44*, 6054-6057.

9. Zhang, P.; Rogelj, S.; Nguyen, K.; Wheeler, D. Design of a highly sensitive and specific nucleotide sensor based on photon upconverting particles. *J. Am. Chem. Soc*. **2006**, *128*, 12410-12411.

10. Chen, Z.G.; Chen, H.L.; Hu, H.; Yu, M.X.; Li, F.Y.; Zhang, Q.; Zhou, Z.G.; Yi, T.; Huang, C.H. Versatile synthesis strategy for carboxylic acid−functionalized upconverting nanophosphors as biological labels. *J. Am. Chem. Soc*. **2008**, *130*, 3023-3029.

11. Peng, J.H.; Wang, Y.H.; Wang, J.L.; Zhou, X.; Liu, Z.H. A New biosensor for glucose determination in serum based on up-converting fluorescence resonance energy transfer. *Biosens. Bioelectron*. **2011**, *28*, 414-420.

12. Wang, Y.H.; Bao, L.; Liu, Z.H.; Pang, D.W. Aptamer biosensor based on fluorescence resonance energy transfer from upconverting phosphors to carbon nanoparticles for thrombin detection in human plasma. *Anal. Chem.* **2011**, *83*, 8130-8137.

13. Yuan, Y.X.; Liu, Z.H. An effective approach to enhanced energy-transfer efficiency from up-converting phosphors and increased assay sensitivity. *Chem. Comm.* **2012**, *48*, 7510-7512.

14. Wang, M.; Hou, W.; Mi, C. C.; Wang, W. X.; Xu, Z. R.; Teng, H. H.; Mao, C. B.; Xu, S. K. Immunoassay of goat antihuman immunoglobulin G antibody based on luminescence resonance energy transfer between near-infrared responsive $NaYF_4$:Yb, Er upconversion fluorescent nanoparticles and gold nanoparticles. *Anal. Chem*. **2009**, *81*, 8783-8789.

15. Chen, S. J.; Chang, H. T. Nile red-adsorbed gold nanoparticles for selective determination of thiols based on energy transfer and aggregation. *Anal. Chem*. **2004**, *76*, 3727-3734.

16. Wargnier, R.; Baranov, A.V.; Maslov, V.G.; Stsiapura, V.; Artemyev, M.; Pluot, M.; Sukhanova, A.; Nabiev, I. Energy transfer in aqueous solutions of oppositely charged CdSe/ZnS core/shell quantum dots and in quantum dot−nanogold Assemblies. *Nano Lett*. **2004**, *4*, 451-457.

17. Fan, C. H.; Wang, S.; Hong, J. W.; Bazan, G. C.; Plaxco, K. W.; Heeger, A. J. Beyond superquenching: Hyper-efficient energy transfer from conjugated polymers to gold nanoparticles. *Proc. Natl. Acad. Sci*. *USA.* **2003**, *100*, 6297-6301.

18. Dubertret, B.; Calame, M.; Libchaber, A. J. Single-mismatch detection using gold-quenched fluorescent oligonucleotides. *Nat. Biotechnol*. **2001**, *19*, 365-370.

19. Maxwell, D. J.; Taylor, J. R.; Nie, S. Self-assembled nanoparticle probes for recognition and detection of biomolecules. *J. Am. Chem. Soc*. **2002**, *124*, 9606-9612.

20. Ye, W. W.; Tsang, M. K.; Liu, X.; Yang, M.; Hao, J. Upconversion luminescence resonance energy transfer (LRET)-based biosensor for rapid and ultrasensitive detection of Avian Influenza virus H7 subtype. *Small* **2014**, *10*, 2390-2397.

21.Li, M. J.; Jiao, P. C.; Lin, M.; He, W. W.; Chen, G. N.; Chen. X. High electrochemiluminescence of a new water-soluble Ir (III) complex for determination of antibiotics. *Analyst* **2011**, *136*, 205-210.

22. Shiu, H. Y.; Wong, M. K.; Che, C. M. Turn-on FRET-based luminescent Ir (III) probes for the detection of cysteine and homocysteine. *Chem. Commun.* **2011**, *47*, 4367-4369.

23. Li, C. X.; Lin, J.; Guo, Y. S.; Zhang, S. S. A Novel electrochemiluminescent reagent of Ir complex-based DNA biosensor and its application in cancer cell detection. *Chem. Commun*. **2011**, *47*, 4442-4444.

24. Boyer, J. C.; Vetrone, F.; Cuccia, L. A.; Capobianco, J. A. Synthesis of colloidal upconverting $NaYF_4$ nanocrystals doped with Er^{3+}, Yb^{3+} and Tm^{3+}, Yb^{3+} via thermal decomposition of Ln^{3+} trifluoroacetate precursors. *J. Am. Chem. Soc*. **2006**, *128*, 7444-7445.

25. Simpson, D. A.; Gibbs, W. E.; Collins, S.; Blanc, W.; Dussardier, B.; Mannom, G.; Peterka, P.; Baxter, G.W. Visible and near infrared up-conversion in Tm^{3+}/Yb^{3+} co-doped silica fibers under 980 nm excitation. *Opt. Express* **2008**, *16*, 13781-13799.

26. Shi, W.; Sahoo, Y.; Swihart, M.T. Gold nanoparticles surface-terminated with bifunctional ligands. *Colloids and Surfaces A: Physicochem. Eng. Aspects* **2004**, *246*, 109-113.

27. Bandini, M.; Bianchi, M.; Valenti, G.; Piccinelli, F.; Paolucci, F.; Monari, M.; Umani-Ronchi, A.; Marcaccio, M. Electrochemiluminescent functionalizable thiophene-based Ir(III) complexes. *Inorg. Chem*. **2010**, *49*,1439.

CHAPTER 4 – DIRECT NEAR-INFRARED SENSING OF Cu^{2+} IONS USING CURCUMIN TAGGED $LiYF_4$:Tm^{3+}, Yb^{3+} UPCONVERTING NANOHYBRID MATERIAL

4.1 Abstract

A UV-to-near-infrared (NIR) emitting optical nanosensor based on NIR perturbable $LiYF_4$:Tm^{3+}, Yb^{3+} UCNPs functionalized with an organic natural product, curcumin constitute a preferred material for the sensitive detection of Cu^{2+}. This NIR excited inorganic/organic nanohybrid material showed high selectivity, sensitivity, and excellent Stern-Volmer features. Energy transfer between the donor UCNPs and the locally decorated curcumin as an acceptor or reporter molecule is a key feature in sensing of Cu^{2+}. This has been achieved by careful synthesis of monodispersed UV-to-NIR emitting $LiYF_4$:Tm^{3+}, Yb^{3+} UCNPs followed by coating with a thin layer of SiO_2 in order to render them water dispersible. These SiO_2-coated UCNPs act as suitable donor material when functionalized with biocompatible curcumin (energy acceptor) leading to the formation of the inorganic/organic nanohybrid, which has been proven to be an excellent material for sensing of Cu^{2+} ions with high selectivity. The detection limit of this nanohybrid has been found to be 4.75 nM, which is far below than the allowed Cu^{2+} limit for drinking water established by the United States Environmental Protection Agency. The presence of curcumin on the surface of SiO_2-coated UCNPs gives this nanohybrid material additional fluorescent property for future *in-vivo* imaging applications.

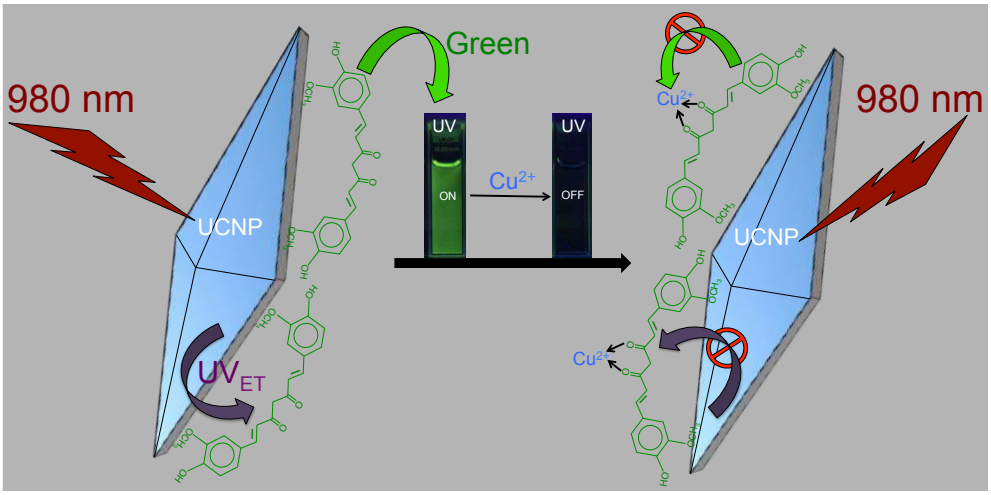

4.2 Introduction

Copper is an indispensable element for living organisms playing, for example, a very significant role as catalysts in a number of biological processes and structural roles in proteins [1]. Copper is the third most abundant metal in the human body and is a co-factor required for the normal functioning of many enzymes involved in physiological processes such as respiration, immune response and wound repair in humans [2]. Cell proliferation and tumor angiogenesis are caused by Cu^{2+} [3-5], and disturbance of Cu^{2+} homeostasis could lead to some serious neurodegenerative diseases, including Alzheimer's, Parkinson's, Prion's and Wilson's disease [6-17]. However, an excess of Cu^{2+} is cytotoxic and can lead to serious consequences. For example, studies have reported that high amounts of Cu^{2+} were found in certain tumor tissues, most likely caused by the interaction of copper with superoxide radicals leading to the formation of hydroxyl radicals causing damage to proteins, RNA, and DNA [18-19]. Moreover, widespread use of Cu^{2+} is also toxic to microorganisms in submicromolar concentration levels [20].

Owing to its potential toxic effects, detection of Cu^{2+} ions has gained significant attention in disease control. Over the years many methods have been developed for the selective determination of Cu^{2+} that exploit the colorimetric [21-22], optical [23-25] and electrochemical [26-28] properties of various molecules. However, these methods may require cumbersome sample pre-treatment as well as multistep synthetic procedures involving toxic chemicals and they may also be limited by an unstable detection signal. Many advanced instrumental methods have also been used for the detection or imaging of Cu^{2+} including atomic absorption spectroscopy (AAS), inductively coupled plasma-mass spectrometry (ICP-MS) and inductively coupled plasma atomic emission spectroscopy (ICP-AES) [29-32]. Although these methods offer good limits of detection (LODs) and wide working concentration ranges, these techniques require the use of expensive equipment and may be unsuitable for on-site or field monitoring. In addition use of these instruments involve very complex sample preparation methods and are also time-consuming typically requiring a trained professional.

Here, we propose the use of a more facile optical method for the detection of Cu^{2+} ions at near-infrared (NIR) emission wavelength by exploiting NIR perturbable upconverting nanoparticles (UCNPs), which through a multiphoton absorption process, are capable of (up)converting the NIR excitation light to higher energies spanning the UV-visible-NIR spectral regions [33]. As a result of these interesting and unusual optical properties, UCNPs have been explored for a number of biomedical applications ranging from cell labeling and tracking [34], *in vivo* imaging [35], controlled drug and payload delivery [36], *in situ* photodynamic therapy [37], and nanothermometry/thermal imaging [38]. Since the donor Ln^{3+} based UCNPs are luminescent, they can transfer their energy to the acceptor, which can either be fluorescent or quencher [39]. This unique property has been advantageous for biosensing [40-46] and chemical sensing [47] applications and offers many advantages over conventional fluorophores.

In this work a reusable Cu^{2+} nanosensor has been realized using UV-to-NIR emitting $LiYF_4$:Tm^{3+}, Yb^{3+} UCNPs as the energy donor while for the acceptor, on the other hand, a biocompatible organic natural product, curcumin was chosen. Most reported FRET/LRET based biosensors use toxic and expensive fluorophores as the energy acceptors. Hence, in this work, we have opted for curcumin as the energy acceptor. The use of curcumin in the form of turmeric powder derived from the plant *curcuma longa* as energy acceptor offers unprecedented advantages such as enhanced biocompatibility, no toxicity, excellent fluorescent properties, as well as multifunctionality such as, its ability to be used in photodynamic therapy [48-50]. Curcumin is also known to have potential anti-inflammatory and anti-cancer properties [51-58]. Thus, the nanosensor reported here completely eliminates the use of any toxic and more expensive organic fluorophores. Furthermore, many of the commercially available organic fluorophores typically used as energy acceptors suffer from high bleach rate and the requirement for direct UV excitation, which ultimately increases scattering and reduces penetration depth in biological media. UV excitation also increases their propensity to undergo photolysis reactions which lead to the disintegration of the molecules and possible reaction with other impurities [59]. In the proposed nanohybrid system the ratiometric detection of Cu^{2+} takes places at both visible and NIR wavelengths. The presence of curcumin at the surface of the UCNPs acts as an energy acceptor both at the visible

and the NIR wavelengths upon NIR wavelength excitation of the UCNPs. Additionally, Cu^{2+} alone shows strong absorption at the NIR wavelength which overlaps with the NIR emission from the UCNPs thus proving a great opportunity to sense Cu^{2+} with enhanced sensitivity and selectivity in the NIR region.

4.3 Results and Discussion

4.3.1 Morphological Characterization

Monodispersed, bipyramidal shaped $LiYF_4$:Tm^{3+}, Yb^{3+} UCNPs were synthesized using the previously reported thermal decomposition method [60]. The X-ray diffraction (XRD) pattern of the UCNPs confirmed the formation of the pure tetragonal phase, with reference to the standard JCPDS card no-01-077-0816 (Figure 4.1).

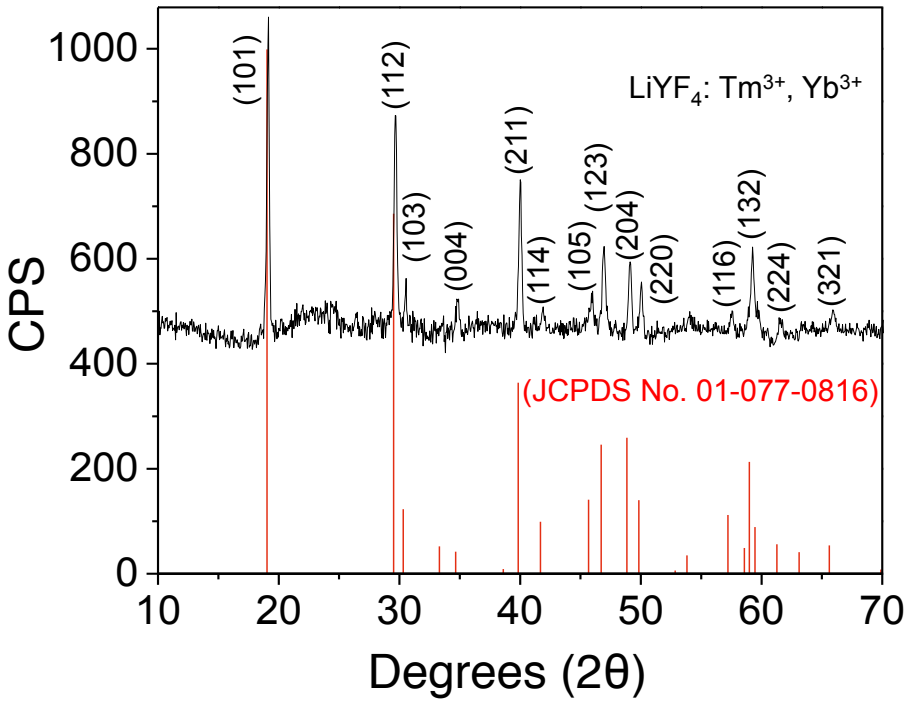

Figure 4.1 XRD spectrum of oleic acid capped UCNPs (black), with reference to the standard (red) $LiYF_4$ crystals (JCPDS No. 01-077-0816).

The transmission electron microscopy (TEM) micrograph shows that the synthesized UCNPs were uniform in size with a very narrow particle size distribution (Figure 4.2C). As seen in the TEM image in Figure 4.2A, the $LiYF_4$:Tm^{3+},Yb^{3+} UCNPs crystallized with a square bipyramidal morphology possessing a mean particle size of approximately 62

nm (in width) and 105 nm (in length) with an aspect ratio of 1.69 (Figure 4.2C). The synthesized UCNPs were highly dispersible in the major organic non-polar solvents such as toluene and hexane. However, since this work aims to detect Cu^{2+} ion in aqueous media, it is crucial to make the UCNPs dispersible in water. Hence, the synthesized UCNPs, with hydrophobic oleic acid as capping ligands, were surface modified with a thin layer of SiO_2 on their surface. The TEM image (Figure 4.2B) confirms the homogeneity and the thickness of the SiO_2 shell around the UCNPs.

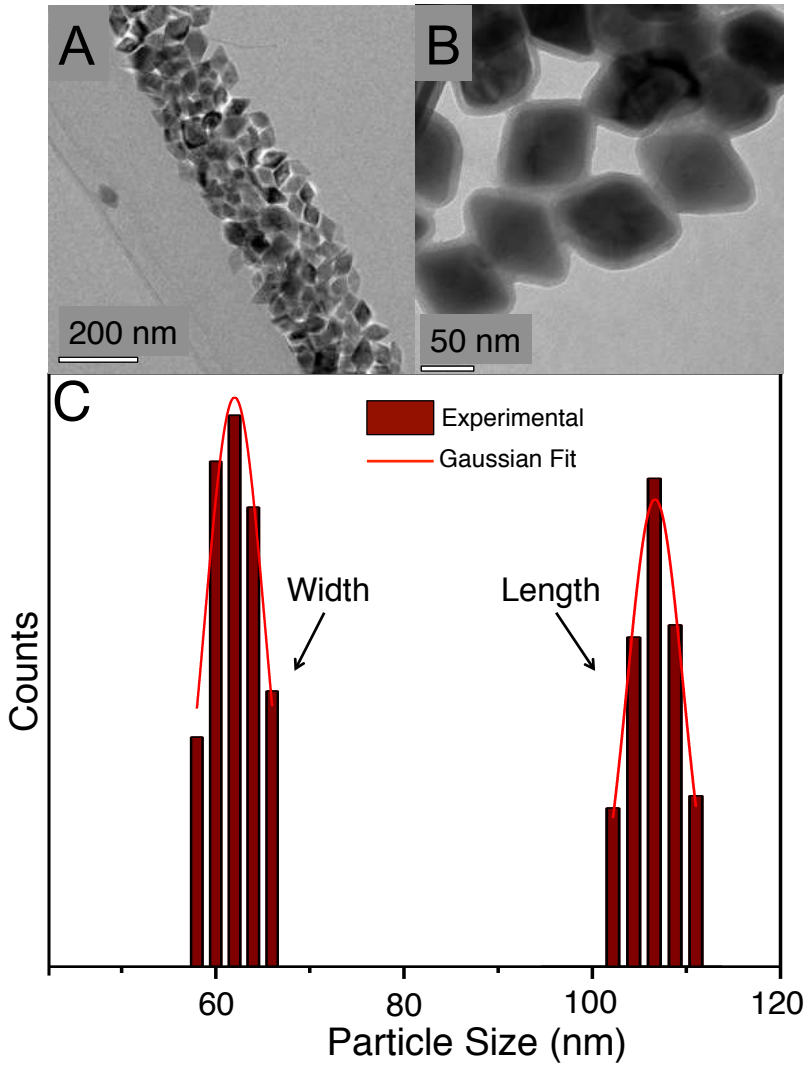

Figure 4.2 Transmission electron microscopic image of the synthesized (A) oleate-capped $LiYF_4:Tm^{3+}$, Yb^{3+} (B) silica coated UCNPs (C) Particle size distribution of the oleate-capped UCNPs for length and width.

4.3.2 Surface Characterization

The Fourier Transform Infrared Spectroscopy (FTIR) (Figure 4.3) confirms the presence of oleic acid on the hydrophobic UCNP surface (blue line). The peaks at 1467 and 1563 cm^{-1} are due to carboxylate symmetrical and asymmetrical stretching vibrations, respectively. Also, the strong absorption bands at 2856 and 2927 cm^{-1} are due to the symmetrical and asymmetrical C–H stretching vibrations of the aliphatic chain of the oleate capping ligand. Furthermore, the band at 3448 cm^{-1} is due to the O-H stretching vibration [40,41,60]. The peak at 1712 cm^{-1} is due to the carbonyl stretching vibration of carboxyl group of oleic acid. Following surface modification of the $LiYF_4$:Tm^{3+}, Yb^{3+} UCNPs with the silica shell (black line), the intensities of C-H symmetrical and asymmetrical vibrations were reduced. However, a broad peak appears at 1122 cm^{-1} is attributed to the Si-O-Si stretching vibration and the peak at 916 cm^{-1} is the result of the Si-O-Si bending vibration. Finally, the peak 1461 cm^{-1} is due to O-H bending vibration [60].

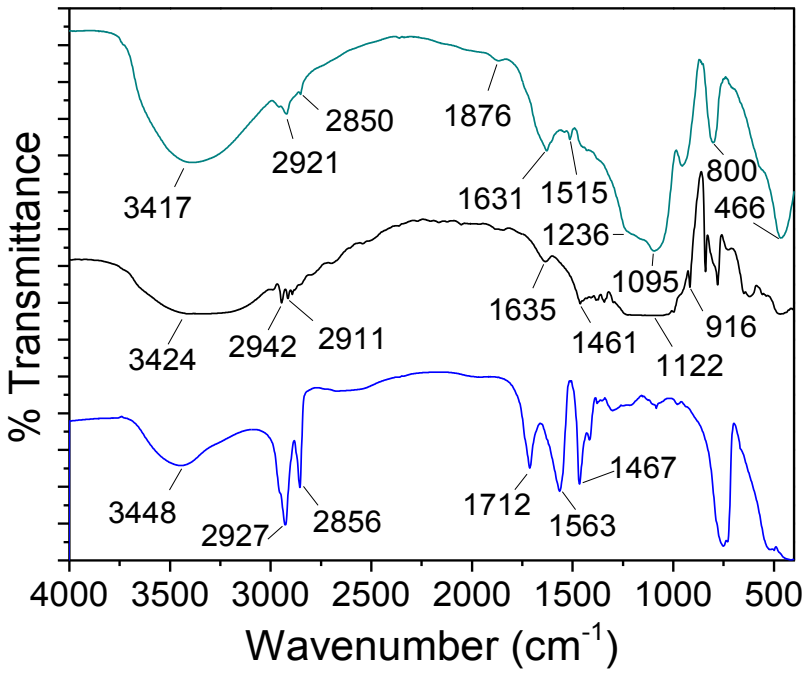

Figure 4.3 FTIR spectra of oleate-capped $LiYF_4$:Tm^{3+}, Yb^{3+} UCNPs (blue), SiO_2 coated UCNPs, $LiYF_4$:Tm^{3+}, Yb^{3+}@SiO_2 (black) and curcumin functionalized SiO_2 coated UCNPs, $LiYF_4$:Tm^{3+}, Yb^{3+}@SiO_2-curcumin (green).

The peak at 1635 cm^{-1} is the result of the C-C bending vibration, and another notable change is that the carbonyl peak at 1712 cm^{-1} ascribed to the oleic acid capping ligand is completely reduced thus confirming the successful silica coating. The FTIR spectrum of the UCNP@SiO_2-curcumin–Cu^{2+} complex showed a slightly broadened carbonyl (C=O) band at 1631 cm^{-1}, which differs from the uncoordinated carbonyl band that typically appears around 1715 cm^{-1}. The reduction in the wavenumber clearly confirms the coordination of the carbonyl functional groups of curcumin to the Cu^{2+} ion. The Cu^{2+}-curcumin complex also showed a symmetrically large broadband at 3417 cm^{-1} due to O-H stretching indicating a symmetrical structure of complex compound [63]. The peaks 2850 cm^{-1} and 2921 cm^{-1} are due to the symmetrical and asymmetrical C-H stretching vibrations of the curcumin ligand. Also, the peaks at 1515, 1236, 1095 and 800 cm^{-1} are attributed to the curcumin ligand, specifically the aromatic C=C stretching vibration, the C-O stretching of the phenolic functional group, the $–OCH_3$ stretching and the C-H bending vibration of the aromatic rings, respectively [63]. The reasonably sharp peak at 466 cm^{-1} confirms the metal [Cu^{2+}←O] oxygen coordinate bond. This confirmed the complexation of curcumin to Cu^{2+} and using β-diketone part as the binding site [61, 63] (Scheme 4.1). The $LiYF_4$:Tm^{3+}, Yb^{3+}@SiO_2-curcumin UCNPs were prepared by incubation with various concentrations of curcumin with the $LiYF_4$:Tm^{3+}, Yb^{3+}@SiO_2 UCNPs and the amount of functionalized curcumin was determined by UV-vis absorption spectroscopy.

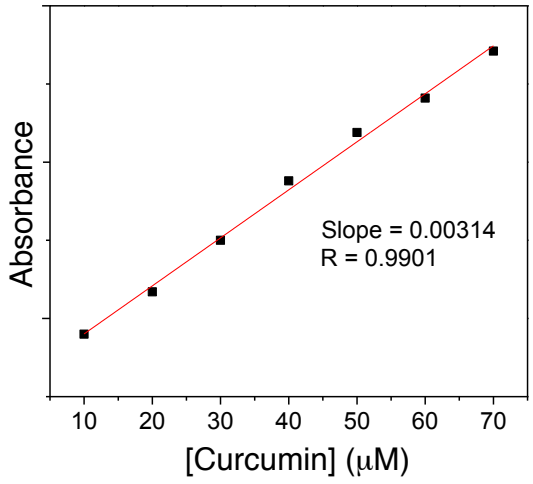

Figure 4.4 Loading of curcumin on the $LiYF_4$:Tm^{3+}, Yb^{3+}@SiO_2 UCNPs determined by UV-Vis absorption.

Thus, by comparing the absorption intensities of the curcumin loaded nanoparticle solutions, the curcumin loading on the hydrophilic SiO_2 layer of the UCNPs was determined to be approximately 66% (Figure 4.4). The addition of increased concentrations of curcumin changed the colorless SiO_2 coated UCNP colloid to a dark yellow color.

4.3.3 Photophysical Characterization

Prior to any Cu^{2+} sensing experiments, a thorough photophysical study was carried out. Figure 4.5 shows the upconversion emission spectrum of the $LiYF_4$:Tm^{3+}, Yb^{3+}@SiO_2 UCNPs following 980 nm excitation (black curve). The upconverted UV emissions at 345 and 360 nm were assigned to the $^1I_6 \rightarrow {}^3F_4$ and $^1D_2 \rightarrow {}^3H_6$ transitions, respectively, while the blue upconversion emission bands at 450 and 480 nm were assigned to the $^1D_2 \rightarrow {}^3F_4$ and $^1G_4 \rightarrow {}^3H_6$ transitions, respectively. At lower energies, the green emission centered at 510 nm was assigned to the $^1D_2 \rightarrow {}^3H_5$ transition, the red emission centered at 650 nm was ascribed to the $^1G_4 \rightarrow {}^3F_4$ transition while the NIR emission at 800 nm resulted from the $^3H_4 \rightarrow {}^3H_6$, $^1G_4 \rightarrow {}^3H_5$ transitions. Moreover, Figure 4.5 also shows the UV/Vis absorption (blue curve) and emission spectra following UV excitation (green curve) of curcumin in the curcumin functionalized $LiYF_4$:Tm^{3+}, Yb^{3+}@SiO_2 UCNPs. For comparison purposes, the UV/vis absorption of the Cu^{2+} ion is also shown in Figure 4.5. This figure shows that the curcumin has an absorbance in the UV - blue region with an absorption maximum centered at 425 nm. This absorbance partially overlaps with the UV emissions of the $LiYF_4$:Tm^{3+}, Yb^{3+}@SiO_2 UCNPs at 345 and 360 nm (from the $^1I_6 \rightarrow {}^3F_4$ and $^1D_2 \rightarrow {}^3H_6$ transitions, respectively) and has maximum overlap with the blue emission band at 450 nm (from the $^1D_2 \rightarrow {}^3F_4$ transition). Given the favorable spectral overlap between the emission of the energy donor (UCNPs) and the absorption of the energy acceptor (curcumin), energy transfer (either radiative or non-radiative) has been envisaged between the UCNPs and curcumin for sensing of Cu^{2+} ion. Here, curcumin acts as a coordinating ligand for Cu^{2+} at the surface of the UCNPs. It is interesting to note that since the surface functionalized curcumin does not absorb in the NIR region where the upconverted NIR emission of $LiYF_4$:Tm^{3+}, Yb^{3+} UCNPs occurs, and hence curcumin could be more effectively used as a coordinating Cu^{2+} capturing ligand and helps with the efficient energy transfer between the UCNPs and Cu^{2+}. Curcumin can

also be taken as a reference to allow for ratiometric detection of Cu^{2+} in the visible region as well. Another interesting fact about this nanosensor is that, since only Cu^{2+} ion absorbs strongly in the NIR region, sensing of Cu^{2+} directly at the NIR wavelength has been possible.

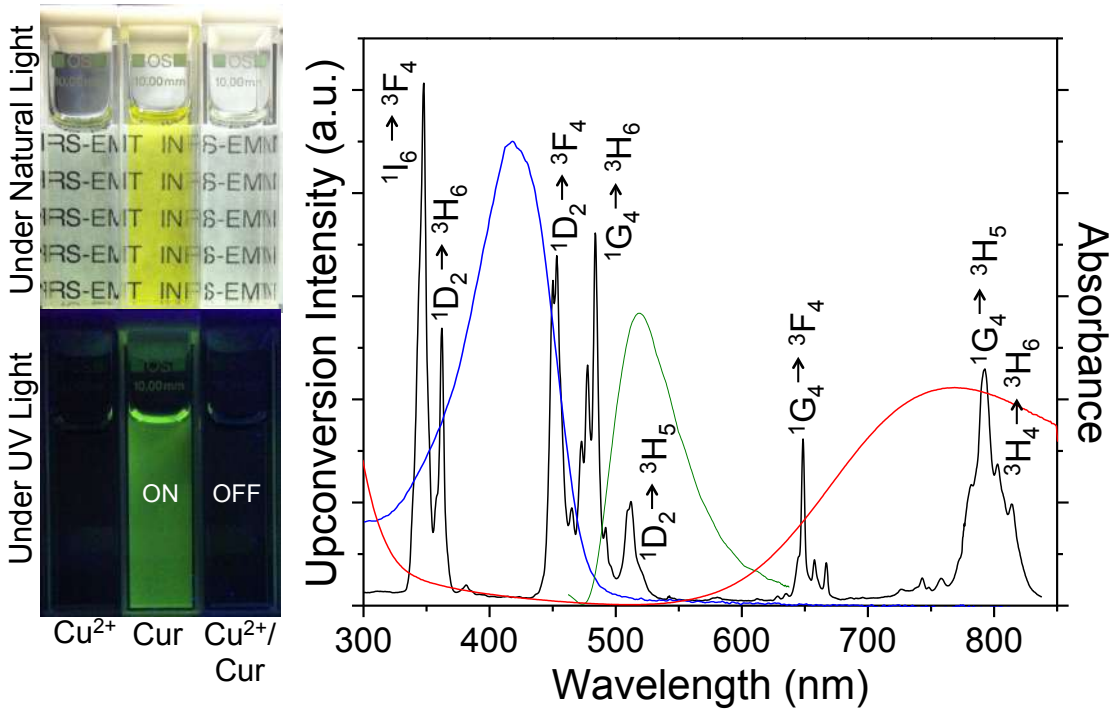

Figure 4.5 Photophysical properties of curcumin, UCNPs, and Cu^{2+} ion. Upconversion emission spectrum of $LiYF_4:Tm^{3+}$, Yb^{3+}@SiO_2 (black) with their respective energy level transitions; UV-vis absorption spectrum curcumin (blue); emission spectrum of curcumin (green, λ_{exc}=360 nm); UV-vis absorption spectrum Cu^{2+} (red).

4.3.4 Energy Transfer from the UCNPs to the surface tagged curcumin at 980 nm NIR excitation

It is evident from Figure 4.5 that the photophysical properties of curcumin, overlap with the emission spectrum of the $LiYF_4:Tm^{3+}$, Yb^{3+} UCNPs. Curcumin showed strong UV absorption ranging from 300 nm to 480 nm. Upon UV absorption it emits strongly at 510 nm in the green region. Since our $LiYF_4:Tm^{3+}$, Yb^{3+} UCNPs have a unique strong UV emission, we envisaged UV energy transfer from the UCNPs (at 980 nm excitation) to curcumin and enhancement of UCNP emission at 510 nm due to curcumin. This was indeed the case when the $LiYF_4:Tm^{3+}$, Yb^{3+} UCNPs were loaded with curcumin in the

silica shell. At the same time, the UCNP emission from UV to blue, especially between wavelengths 300 and 450 nm, completely were quenched due to the surface tagged curcumin, which absorbs strongly in this region. The weak emission of UCNPs at 510 nm was indeed enhanced upon NIR excitation, due to the radiative energy transfer from the curcumin to the $^1D_2 \rightarrow {}^3H_5$ transition of UCNPs as depicted below (Scheme 4.1) in the energy level diagram of UCNP-curcumin nanohybrid.

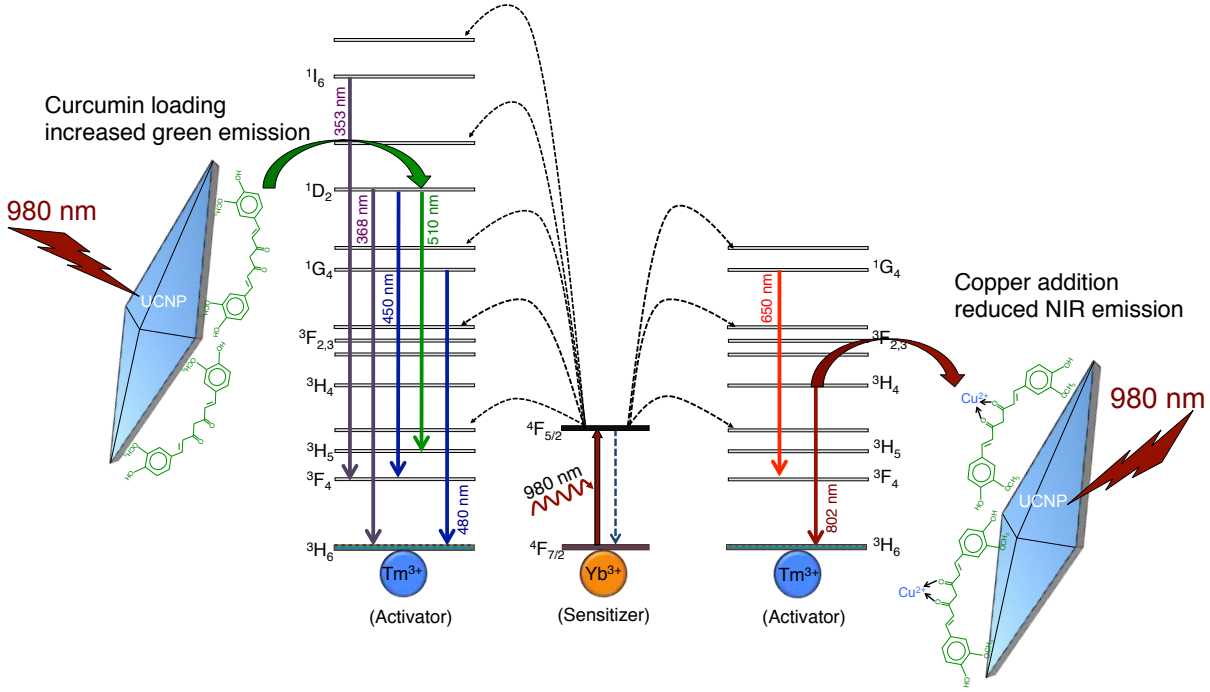

Scheme 4.1 Energy level transitions in the $LiYF_4$:Tm^{3+}, Yb^{3+} UCNPs and the plausible LRET between the UCNPs and surface functionalized organic natural product, curcumin.

Upconversion luminescence measurements were carried out on the $LiYF_4$:Tm^{3+}, Yb^{3+}@SiO_2-curcumin UCNPs and from Figure 4.6A, it is evident that increased concentrations of curcumin on the surface of the UCNPs showed increased luminescence quenching in the UV at 345 and 360 nm corresponding to the $^1I_6 \rightarrow {}^3F_4$ and $^1D_2 \rightarrow {}^3H_6$ transitions (Figure 4.6B) as well as in the blue at 450 nm assigned to the $^1D_2 \rightarrow {}^3F_4$ transition (Figure 4.6C). This confirmed the energy transfer from the UCNPs to the locally functionalized curcumin. Moreover, due to the overlapping curcumin emission, the green Tm^{3+} emission due to the $^1D_2 \rightarrow {}^3H_5$ transition (510 nm) showed a slight increase in luminescence at this wavelength as shown in Figure 4.6D indicative again of energy transfer from curcumin back to Tm^{3+} ion of the UCNPs.

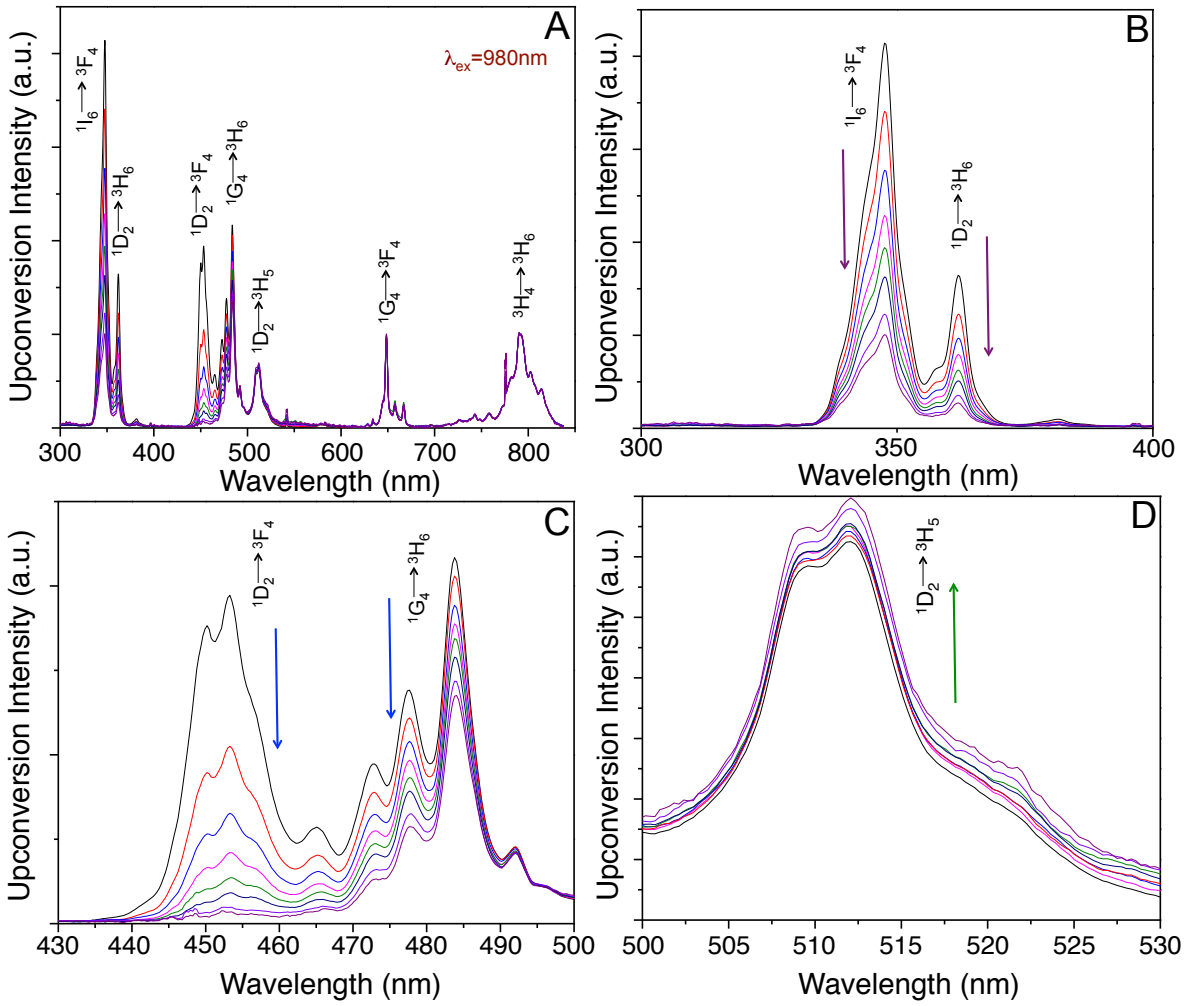

Figure. 4.6 (A) UV to NIR UC Luminescence spectra of the curcumin-loaded $LiYF_4$:Tm^{3+}, Yb^{3+}@SiO_2 UCNPs. (B) A gradual decrease in the UV emission intensity of UCNP upon successful loading of curcumin. (C) Decrease in the blue emission of Tm^{3+} in the UCNP due to strong absorption by the surface tagged curcumin. (D) Increase in the green emission at 510 nm due to the LRET from the curcumin to the UCNP.

4.3.5 Sensing of Cu^{2+} at the Visible Wavelength

The detection of Cu^{2+} depends on the energy transfer from the UCNPs to the Cu^{2+} and the efficiency of this process, in turn, depends on the distance between the UCNPs and Cu^{2+}-curcumin complex. To study the effect of Cu^{2+} ions on the upconversion luminescence, increased concentrations of Cu^{2+} were titrated into the aqueous solution containing the $LiYF_4$:Tm^{3+}, Yb^{3+}@SiO_2-curcumin UCNPs. Following each addition, the solution was excited at 980 nm, and the upconversion luminescence spectrum was

recorded (Figure 4.7A). It was observed that the addition of Cu^{2+} ion to the UCNP/curcumin nanohybrid reduced the upconversion luminescence at 510 nm corresponding to the $^1D_2 \rightarrow {}^3H_5$ transition of the UCNPs. This reduction in upconversion luminescence intensity upon increased loading of Cu^{2+} was due to the coordination complex formation between the ligand curcumin (electron donor) and the Cu^{2+} (electron acceptor).

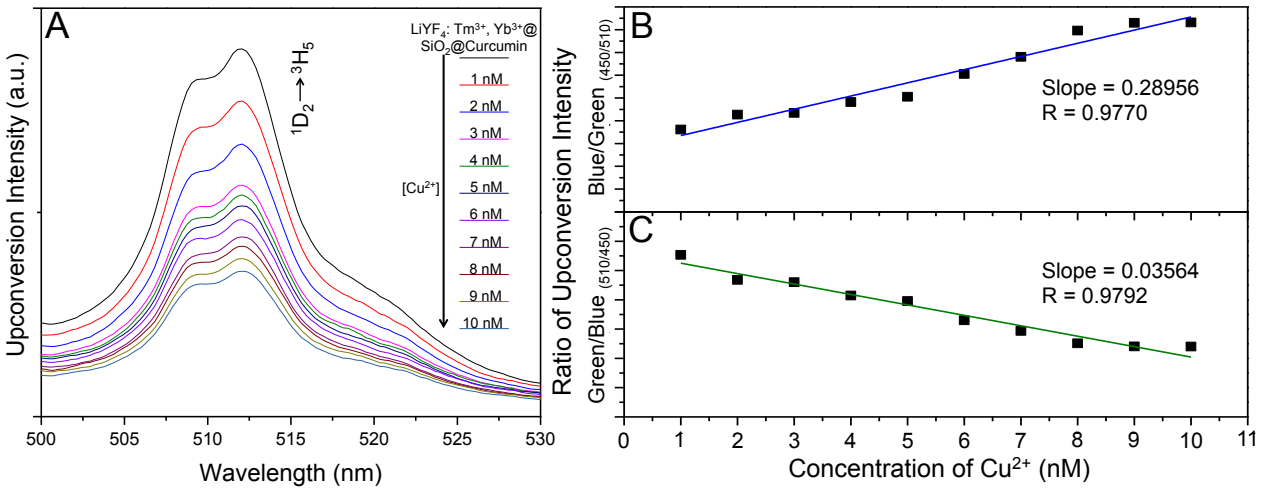

Figure 4.7 (A) Gradual decrease in the upconverted green luminescence intensity of the $LiYF_4$:Tm^{3+}, Yb^{3+}@SiO_2-curcumin UCNPs upon successful titration of various concentrations of Cu^{2+} ions. (B) Decrease in the upconverted green emission intensity with reference to the upconverted blue emission confirming the absence of energy transfer due to the presence of increased Cu^{2+} concentrations. (C) Increase in the upconverted blue emission intensity at 450 nm with reference to the upconverted green emission at 510 nm also confirms the absence of energy transfer between curcumin and the UCNPs.

This coordination complex does not absorb in the UV or blue region hence the UV and blue emission from the UCNPs are not perturbed with respect to the concentration of Cu^{2+}. The increased addition of Cu^{2+} ion to the UCNP/Curcumin nanohybrid reduces the concentration of free curcumin at the surface of the UCNPs, which eventually reverses the energy transfer between the UCNP and curcumin and hence the green emission due to $^1D_2 \rightarrow {}^3H_5$ transition decreases (Figure 4.7C) with reference to the UV or blue (Figure 4.7B). In this case, the blue transition at $^1D_2 \rightarrow {}^3F_4$ (450 nm) is considered against the green $^1D_2 \rightarrow {}^3H_5$ transition because only 450 nm showed complete quenching due to increased curcumin loading. Hence, it is reasonable to evaluate the

ratio of upconversion emission intensities between 450 and 510 nm wavelengths. The ratio of emission intensities of blue and green against various concentrations of Cu^{2+} showed excellent linear regression values.

4.3.6 Sensing of Cu^{2+} at the NIR Wavelength

The Figure 4.8A shows that the NIR emission intensity of the UCNPs was gradually quenched with increasing concentrations of Cu^{2+}. The quenching followed the Stern–Volmer equation:

$$I/I_0 = 1+K_{sv}\,[Q] \qquad (1)$$

where " I_0 " and " I " are the luminescence emission intensities of UCNPs at 980 nm excitation in the absence and presence of quencher [Cu^{2+}], respectively while K_{sv} is the Stern–Volmer quenching constant. The Stern–Volmer plot was linear in the concentration range of 1 to 1 x 10^{-8} mol/L, as shown in Figure 4.8B, which exhibits excellent linear coefficient of 0.9957 and the Stern–Volmer quenching constant was found to be 6.52 x 10^7. These results show a single static quenching mechanism when mixing oppositely charged curcumin tagged UCNPs and Cu^{2+} due to their coordination [24].The binding constant (K_b) and binding stoichiometry (n) for static quenching can be determined by the following equation:

$$\log\,[(I_0-I)/I] = \log K_b + n\,\log\,[Q] \qquad (2)$$

when curcumin molecules on the surface of the UCNPs bind independently to the Cu^{2+} ion, where, I_0 and I are the upconversion luminescence intensities in the absence and presence of the quencher [Cu^{2+}] respectively, K_b is the binding constant, and *n* is the binding stoichiometry. The values of K_b and *n* were obtained from the intercept and slope of the double logarithmic plot of log [$(I_0-I)/I$] against log [Cu^{2+}] (Figure 4.8C). The binding constant (K_b) and binding stoichiometry (n) have been calculated to be 3.69 x 10^7 M^{-1} and 1.2, respectively. The high value of binding constant confirms the strong interaction between the curcumin and the quencher, Cu^{2+} at the surface of UCNPs and enhances the energy transfer. The binding stoichiometry (*n*) is about 1.2, which indicates the coordination complex formation between the curcumin and Cu^{2+}.

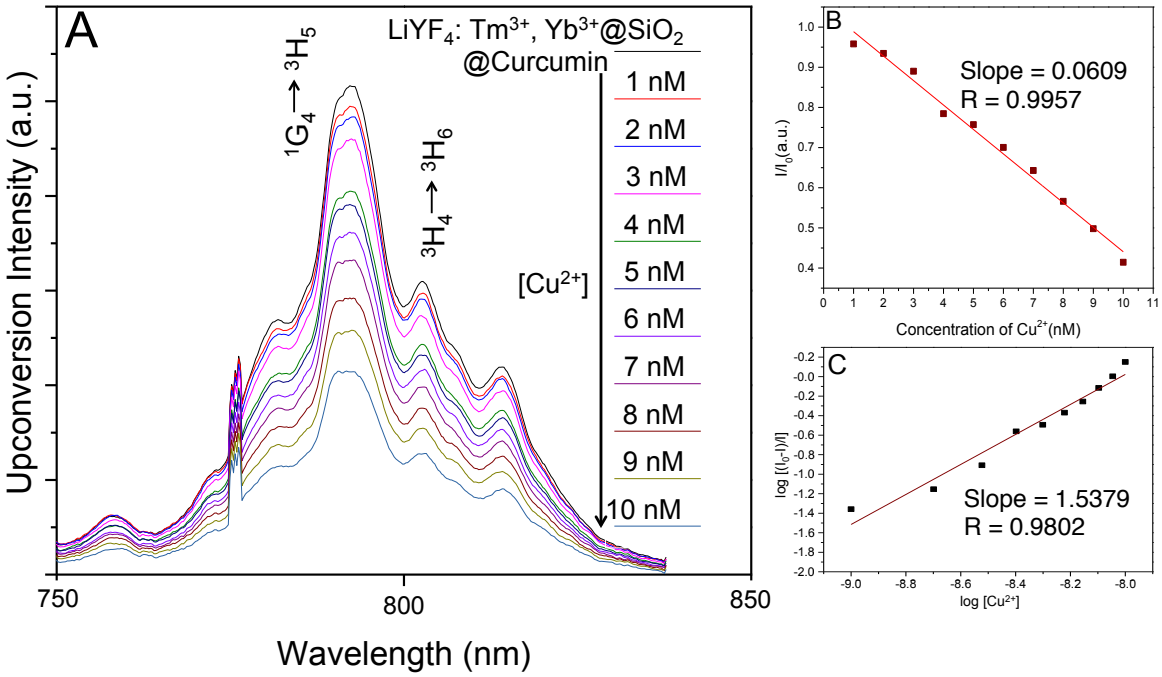

Figure 4.8 (A) Gradual decrease in the upconverted NIR intensity of $LiYF_4$:Tm^{3+}, Yb^{3+}@SiO_2-curcumin UCNPs upon successful titration of different concentrations of Cu^{2+} ions. (B) The stern-volmer plot of Cu^{2+} triggered luminescence quenching of the upconverted NIR emission of the $LiYF_4$:Tm^{3+}, Yb^{3+}@SiO_2-curcumin UCNPs. (C) Plot of $\log[(I_0-I)/I]$ against $\log[Cu^{2+}]$ for the $LiYF_4$:Tm^{3+}, Yb^{3+}@SiO_2-curcumin UCNPs and the quencher (Cu^{2+}).

4.3.7 Sensing of Cu^{2+} at the UV Absorption Wavelength

The UV–vis absorption spectrum of curcumin in the presence and absence of Cu^{2+} is shown in the Figure 4.9A. The free uncoordinated curcumin loaded silica coated UCNPs showed a single broad absorption band with a maximum absorption at 425 nm due to the $\pi \rightarrow \pi^*$ transition. Upon coordination with Cu^{2+} ion, this broad peak has been split into two peaks [61], and the new peak at 450 nm was due to the ligand to metal charge transfer transition (LMCT) [62]. The decrease in the UV absorption of curcumin at various concentrations of Cu^{2+} showed a strong linear dependence with an excellent linear coefficient value of 0.9921 (Figure 4.9B).

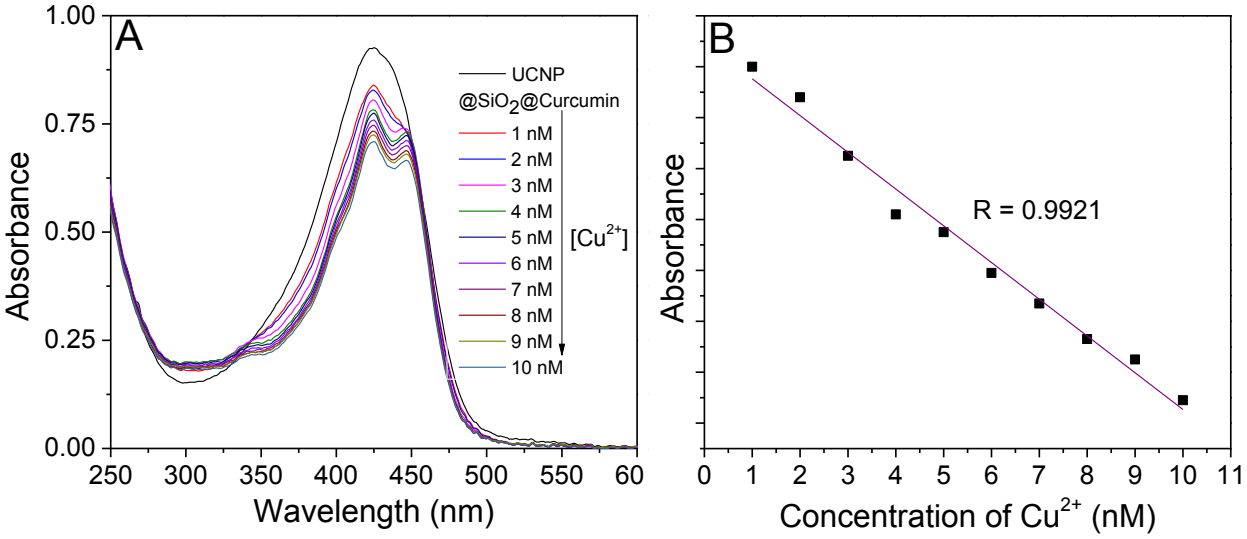

Figure 4.9 UV-vis absorption spectrum of $LiYF_4$:Tm^{3+}, Yb^{3+}@SiO_2-curcumin UCNPs in the presence of different concentrations of Cu^{2+} ions. (B). The decrease in absorbance intensity showing excellent linear relationship.

4.3.8 Selectivity of the $LiYF_4$:Tm^{3+}, Yb^{3+}@SiO_2-curcumin Nanosensor in the Visible Region

In order to confirm the selectivity of this nanohybrid material towards the Cu^{2+} ion, we have investigated both the absorption and upconversion luminescence responses of $LiYF_4$:Tm^{3+}, Yb^{3+}@SiO_2-curcumin against fourteen different metal ions (mono, bi, tri and tetravalent). As demonstrated in Figure 4.10, among all the metal ions tested, only Cu^{2+} quenched the green emission of curcumin upon UV excitation, which is very visible to the naked eye even at a concentration as low as 10 nM. The absorbance of other metal ions such as Fe^{2+}, Zn^{2+}, Ba^{2+}, Co^{2+}, Na^{+}, Sn^{4+}, Ni^{2+}, Cr^{3+}, Cd^{2+}, Hg^{2+}, $Pb^{2+,}$ and Ca^{2+} showed very little or no change in their absorbance (Figure 4.10).

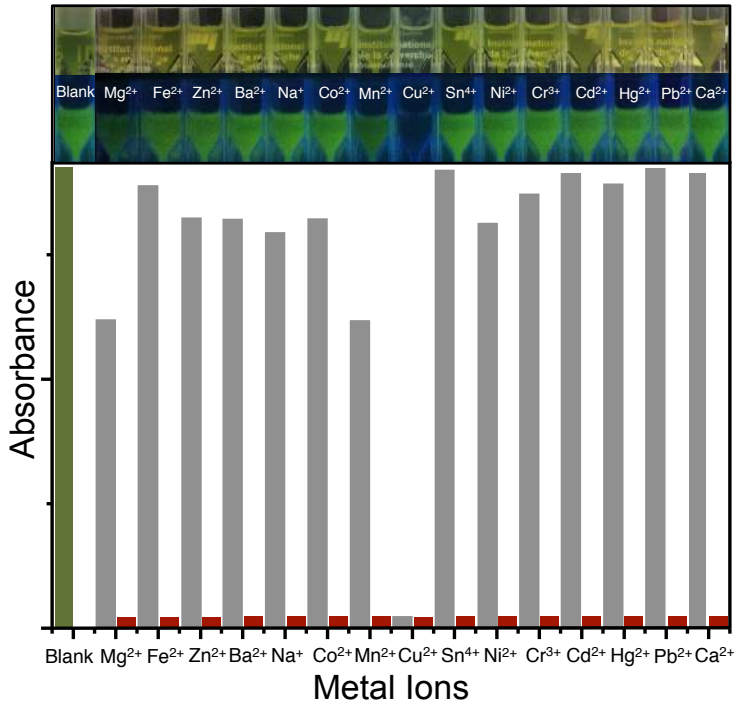

Figure 4.10 UV-vis absorbance of $LiYF_4:Tm^{3+}$, $Yb^{3+}@SiO_2$-curcumin UCNPs against different metal ions showing the high selectivity of the proposed nanohybrid material (Top); Optical images of $LiYF_4:Tm^{3+}$, $Yb^{3+}@SiO_2$-curcumin UCNPs in the presence of different metal ions (Bottom) (Grey bar: $LiYF_4:Tm^{3+}$, $Yb^{3+}@SiO_2$-curcumin UCNPs in the presence of various metal ions before adding Cu^{2+}; Burgundy bar: $LiYF_4:Tm^{3+}$, $Yb^{3+}@SiO_2$-curcumin UCNPs in the presence of various metal ions after adding Cu^{2+}).

4.3.9 Selectivity of the $LiYF_4:Tm^{3+}$, $Yb^{3+}@SiO_2$-curcumin Nanosensor in the NIR Region

The selectivity of the $LiYF_4:Tm^{3+}$, $Yb^{3+}@SiO_2$-curcumin UCNP sensor was also confirmed by upconversion luminescence measurements. The results showed that upconverted NIR luminescence intensity (800 nm) of the $LiYF_4:Tm^{3+}$, $Yb^{3+}@SiO_2$-curcumin UCNPs was quenched while the upconverted green emission intensity (510 nm) increased. The upconversion luminescence of the $LiYF_4:Tm^{3+}$, $Yb^{3+}@SiO_2$-curcumin UCNPs showed absolutely no change in their NIR emission intensities since the metal ions Mg^{2+}, Fe^{2+}, Zn^{2+}, Ba^{2+}, Co^{2+}, Na^{+}, Mn^{2+}, Sn^{4+}, Ni^{2+}, Cr^{3+}, Cd^{2+}, Hg^{2+}, Pb^{2+}

and Ca^{2+} do not absorb in this region. These results confirm that the $LiYF_4$:Tm^{3+}, Yb^{3+}@SiO_2-curcumin UCNPs are very selective towards Cu^{2+} ions over other metal ions including heavy metal ions such as Sn^{4+}, Cr^{3+}, Pb^{2+}, Hg^{2+} and Cd^{2+} confirming their robust nature. Competitive experiments were performed in which both Cu^{2+} ions (10 nM) and 10-fold excess of the other metal ions were simultaneously added to the solution containing the $LiYF_4$:Tm^{3+}, Yb^{3+}@SiO_2-curcumin UCNPs (Figure 4.11).

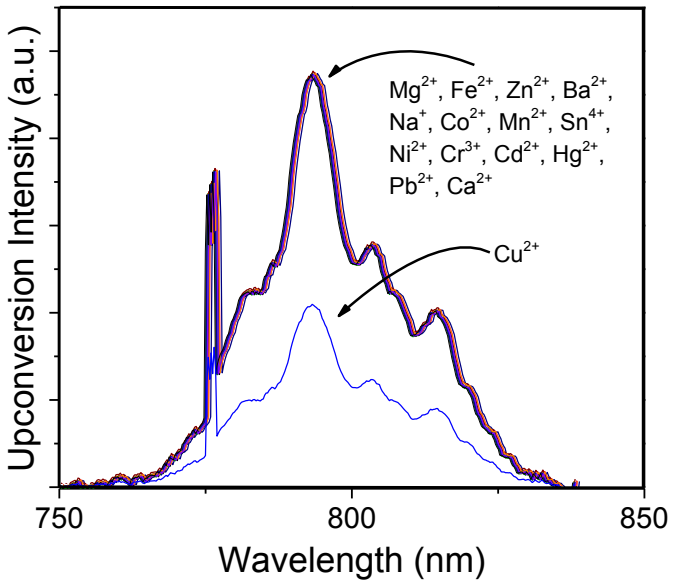

Figure 4.11 The selectivity of Cu^{2+} ion towards curcumin at the NIR region. Among all the ions tested, only Cu^{2+} absorbs in the NIR showing significant reduction in the NIR emission of UCNPs due to [Cu^{2+}←curcumin] complex formed at the surface of UCNPs.

The results showed that the upconversion luminescence intensity response of the $LiYF_4$:Tm^{3+}, Yb^{3+}@SiO_2-curcumin UCNPs by Cu^{2+} ions was not affected by the presence of other metal ions. Thus, $LiYF_4$: Tm^{3+}, Yb^{3+}@SiO_2-curcumin UCNPs have proven to be an excellent optical nanochemosensors for the selective detection of Cu^{2+} ions even in a complex medium.

4.3.10 Reusability of the $LiYF_4$:Tm^{3+}, Yb^{3+}@SiO_2-curcumin Nanosensor

For real world practical applications, it is imperative to confirm the reusability of the $LiYF_4$:Tm^{3+}, Yb^{3+}@SiO_2-curcumin UCNP sensor. When ethylenediaminetetraacetic acid (EDTA) (1 mM) was titrated against an aqueous solution containing 1 wt% of Cu^{2+} (10 nM) coordinated to the $LiYF_4$:Tm^{3+}, Yb^{3+}@SiO_2-curcumin UCNPs, the color of the solution changed from colorless (copper-coordinated to curcumin) to yellow. This confirms that almost all of the Cu^{2+} ions, which were once coordinated to curcumin are now being coordinated to EDTA.

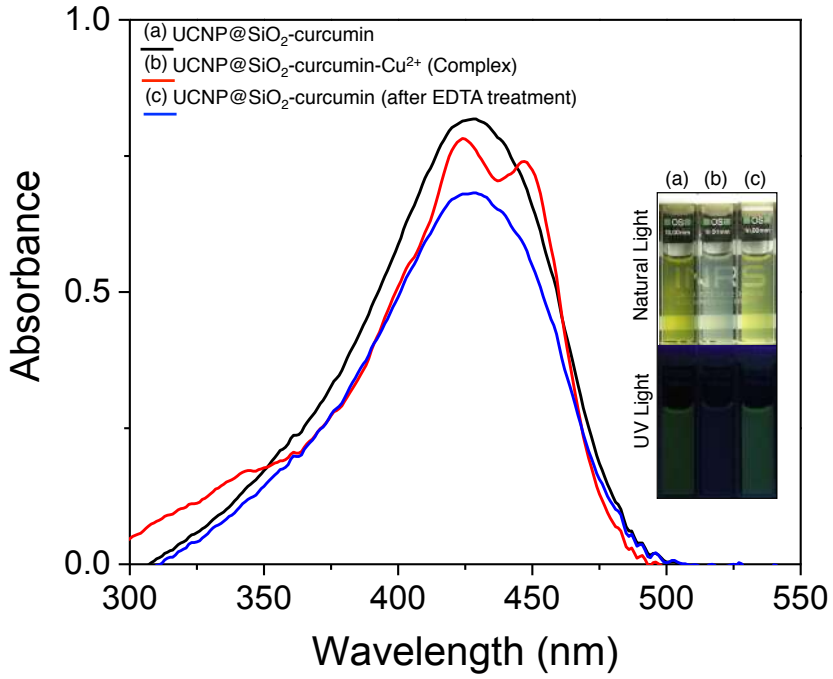

Figure 4.12 The absorbance spectrum of $LiYF_4$:Tm^{3+}, Yb^{3+}@SiO_2-curcumin UCNPs in the absence of Cu^{2+} (Black), in the presence of Cu^{2+} (Red) and after reaction with EDTA (Blue). The splitting of the peak upon addition of Cu^{2+} is due to the $\pi \rightarrow \pi^*$ and ligand to metal charge transfer transition.

Moreover, 85% of the original absorbance of $LiYF_4$:Tm^{3+}, Yb^{3+}@SiO_2-curcumin UCNPs was restored (Figure 4.12). These results confirmed that the coordination complex of curcumin on the $LiYF_4$:Tm^{3+},Yb^{3+}@SiO_2 surface is reversible and since EDTA (hexadentate) is a better ligand than the curcumin (bidentate), Cu^{2+} ions preferably coordinate with EDTA. This confirms the reusability of the curcumin loaded UCNPs for routine and rigorous Cu^{2+} ion sensing applications.

4.4 Experimental Section

4.4.1 Materials and Chemicals

Aqueous ammonia solution ($NH_3 \cdot H_2O$, 28%), tetraethylorthosilicate (TEOS > 98%), anhydrous ethanol, Y_2O_3 (99.99%), Yb_2O_3 (99.9%), Tm_2O_3 (99.99%), trifluoracetic acid (CF_3COOH), lithium trifluoroacetate (CF_3COOLi), oleic acid, 1-octadecen were obtained from Alfa Aesar. $CuCl_2$, $MgCl_2$, $FeCl_2$, $BaCl_2$, NaCl, $ZnCl_2$, $CoCl_2$, $MnCl_2$, $SnCl_4$, $NiCl_2$, $CrCl_3 \cdot 6H_2O$, $CdCl_2$, $HgCl_2$, $PbCl_2$, $CaCl_2$ and curcumin were obtained from Sigma-Aldrich. IGEPAL CO-520, hexane, were purchased from Fluka (USA). Ultrapure water (Millipore) with a resistivity greater than 18.0 MΩ cm was used in all experiments. All chemicals were used as received unless specified.

4.4.2 Instrumentation

The Fourier-transform infrared (FTIR) spectra were recorded on a Thermoscientific Nicolet Spectrometer using FTIR grade KBr as the background. Transmission Electron Microscopy (TEM) images were obtained with a Philips Tecnai 12 (120 kV) microscope. To observe the morphology and size distribution of the UCNPs, 10 mg of the UCNP sample was dispersed in 10 g of hexane and sonicated for 1 h. A drop of the resulting solution was evaporated on a formvar/carbon film supported on a 300 mesh copper grid (3 mm in diameter). X-ray photoelectron spectroscopy (XPS) analyses were performed on a VG Escalab 220i XL instrument equipped with 6 channeltrons using a non-monochromated Mg K X-ray source (1253.6 eV). To identify the phase of the UCNPs, X-ray diffraction (XRD) patterns were recorded using a Bruker D8 Advance Powder Diffractometer with Cu Kα radiation at λ = 0.154 nm operating at 45 kV and 40 mA. The UV-Vis absorption measurements were carried out using a Thermoscientific 2000 spectrophotometer.

The upconversion luminescence spectra were obtained using a Thorlabs fiber-coupled 980 nm laser diode (maximum power of 330 mW) as the excitation source. For the oleate-capped hydrophobic UCNPs, the samples (1 wt% in hexane) were placed in 10 mm path-length quartz cuvettes (Hellma, QS). The upconverted emission light was collected by a lens in a 90° configuration, and then transferred to a spectrophotometer

(Avaspec-2048L-USB2) using an optical fiber. Throughout the course of the experiments, the cuvette was placed in a fixed sample holder that guarantees a comparable laser focalization for every sample, and thus, the possibility to compare intensities between different samples. To confirm this, every spectrum was recorded multiple times.

4.4.3 Synthesis of oleic acid capped upconverting nanoparticles

The thulium (Tm^{3+}) and ytterbium (Yb^{3+}) co-doped $LiYF_4$ UCNPs (0.5 mol% Tm^{3+} and 25 mol% Yb^{3+}) were synthesized via the thermal decomposition method as described previously [60]. Briefly, the Ln^{3+} trifluoroacetate precursors were prepared by reacting Y_2O_3 (1 mmol), Yb_2O_3 (0.27 mmol), Tm_2O_3 (0.005 mmol) in 50/50 v/v CF_3COOH/H_2O at 80 °C for 6 h. Subsequently, the resultant clear solution was evaporated to dryness at 60 °C overnight. The obtained Ln^{3+} trifluoroacetate precursors were mixed with CF_3COOLi (2.5 mmol), oleic acid (20 mL) and 1-octadecene (20 mL). The resulting mixture was degassed to 110 °C with constant stirring under vacuum for 30 min. Thereafter, the temperature of the mixture was increased to 330 °C at a rate of 5 °C/min under argon flow. At this final temperature, the mixture remained for 1 h, after which it was allowed to cool to 70 °C prior to precipitation with ethanol. The $LiYF_4$:Tm^{3+}, Yb^{3+} UCNPs were then separated via centrifugation and further purified by re-dispersing in hexane followed by precipitation with ethanol three times.

4.4.4 Synthesis of $LiYF_4$:Tm^{3+}, Yb^{3+}@SiO_2 upconverting nanoparticles

The silica (SiO_2) shell around the $LiYF_4$:Tm^{3+}, Yb^{3+} UCNPs was grown by mixing 20 mg of the UCNPs dispersed in cyclohexane with 0.1 mL Igepal and 6 mL cyclohexane. After 10 min stirring, 0.4 mL Igepal and 0.08 mL NH_4OH were added to the above flask and sonicated for 20 min. Once the mixture became transparent, 0.04 mL TEOS was added and left to stir for 48 h. The SiO_2-coated $LiYF_4$:Tm^{3+}, Yb^{3+} UCNPs were separated by adding acetone, and subsequently washed with ethanol/water (1:1) twice.

4.4.5 Synthesis of $LiYF_4$:Tm^{3+}, Yb^{3+}@SiO_2-curcumin

5 mg of the curcumin was dissolved in 10 mL of ethanol containing 10 mg of $LiYF_4$:Tm^{3+}, Yb^{3+}@SiO_2. After stirring for 12 h, the $LiYF_4$:Tm^{3+}, Yb^{3+}@SiO_2 UCNPs

functionalized with the curcumin (henceforth $LiYF_4$:Tm^{3+}, Yb^{3+}@SiO_2-curcumin) were separated by centrifugation and washed with ethanol. Loading of the curcumin on the $LiYF_4$:Tm^{3+}, Yb^{3+}@SiO_2 UCNPs was measured by UV−vis absorption spectroscopy (Figure 4.4).

4.4.6 Sensing of Cu^{2+} using $LiYF_4$:Tm^{3+}, Yb^{3+}@SiO_2-curcumin nanohybrid

Various concentrations of Cu^{2+} were added to the 1 wt% aqueous solution of $LiYF_4$:Tm^{3+}, Yb^{3+}@SiO_2-curcumin and the upconversion luminescence optical measurements were performed with 980 nm excitation at room temperature and at constant stirring.

4.4.7 Regeneration of $LiYF_4$:Tm^{3+}, Yb^{3+}@SiO_2-curcumin nanohybrid material

Ethylenediaminetetraacetic acid (EDTA) (1 mM) solution was introduced into $LiYF_4$:Tm^{3+}, Yb^{3+}@SiO_2-curcumin-Cu^{2+} complex and the mixture was stirred for 2 h. The color of the solution slowly changed from colorless to yellow indicating the liberation of Cu^{2+} ions from the curcumin coordination complex. This step was repeated twice to ensure the complete removal of all Cu^{2+} ions from the $LiYF_4$:Tm^{3+}, Yb^{3+}@SiO_2-curcumin UCNPs. UV-vis absorption spectrum was performed on the resultant solution.

4.5 Conclusion

In summary, a near-infrared (NIR) excitable and UV to NIR emitting UCNPs tagged with a biocompatible organic natural product, curcumin, has been demonstrated to be a sensitive and selective luminescence quenching hybrid material for ratiometric sensing of Cu^{2+}. This nanohybrid material is very selective towards Cu^{2+} ions and prompts an optical on-off response in the visible region of the upconversion luminescence spectrum through energy transfer between the UCNP donors and the curcumin acceptors. In addition to the visible changes, the nanohybrid showed sensitive, detectable changes in the NIR region, which is very beneficial since the NIR wavelength is less prone to scattering, has increased penetration depths and thus can be effectively used in biological media. This curcumin based upconversion nanoprobe makes it possible for naked eye detection through colour change hence the metal ion can be detected

colorimetrically. The limit of detection for Cu^{2+} was found to be much lower than the allowed Cu^{2+} concentration as recommended by the World Health Organization (WHO), United States Environmental Protection Agency (USEPA) and Health Canada. The presence of curcumin on the silica surface of the UCNP gives additional biocompatibility and reduced toxicity since curcumin has been generally recognized as safe (GRAS) by the USFDA.

4.6 References

1. Olivares, M.; Uauy, R. Copper as an essential nutrient. *Am. J. Clin. Nutr*. **1996**, *63*, S791-S796.

2. Uauy, R.; Olivares, M.; Gonzalez, M. Essentiality of copper in humans. *Am. J. Clin. Nutr*. **1998**, *67*, 5, S952-S959.

3. Theophanides, T.; Anastassopoulou, J. Copper and carcinogenesis. *Crit. Rev. Oncol. Hematol*. **2002**, *42*, 57-64.

4. Finney, L.; Vogt, S.; Fukai, T.; Glesne, D. Copper and angiogenesis: Unravelling a relationship key to cancer progression. *Clin. Exp. Pharmacol*. *Physiol*. **2008**, *36*, 88-94.

5. Tisato, F.; Marzano, C.; Porchia, M.; Pellei, M.; Santini, C. Copper in diseases and treatments, and Copper-based anticancer strategies. *Med. Res. Rev*. **2010**, *30*, 708-749.

6. Bush, A. I. Metals and Neuroscience. *Curr. Opin. Chem. Biol*. **2000**, *4*, 184-191.

7. Madsen, E.; Gitlin, J. D. Copper and iron disorders of the brain. *Annu. Rev. Neurosci.* **2007**, *30*, 317-337.

8. Gaggelli, E.; Kozlowski, H.; Valensin, D.; Valensin, G. Copper homeostasis and neurodegenerative disorders (Alzheimer's, prion, and Parkinson's diseases and amyotrophic lateral sclerasis). *Chem. Rev*. **2006**, *106*, 1995-2044.

9. Strausak, D.; Mercer, J. F. B.; Dieter, H. H.; Stremmel, W.; Multhaup, G. Copper In disorders with neurological symptoms: Alzheimer's, Menkes, And Wilson diseases. *Brain Res. Bull*. **2001**, *55*, 175-185.

10. Waggoner, D. J.; Bartnikas, T. B.; Gitlin, J. D. The role of copper In neurodegenerative disease. *Neurobiol. Dis*. **1999**, *6*, 221-230.

11. Brown, D. R.; Kozlowski, H. Biological inorganic and bioinorganic chemistry of neurodegeneration based on Prion And Alzheimer diseases. *Dalton Trans*. **2004**, *13*, 1907-1917.

12. Donnelly, P. S.; Xiao, Z.; Wedd, A. G. Copper and Alzheimer's disease. *Curr. Opin. Chem. Biol*. **2007**, *11*, 128-133.

13. Milhauser, G. L. Copper binding in the prion protein. *Acc. Chem. Res*. **2004**, *37*, 79-85.

14. Shao, X.; Gu, H.; Wang, Z.; Chai, X.; Tian, Y.; Shi, G. Highly selective electrochemical strategy for monitoring of cerebral Cu^{2+} based on a carbon dot-TPEA hybridized surface. *Anal. Chem*. **2013**, *85*, 418−425.

15. Brewer, G. J. Alzheimer’s disease causation by copper toxicity and treatment with zinc. *Front. Aging Neurosci*. **2014**, *6*, 1-5.

16. Pramanik, D.; Ghosh, C.; Dey, S. G. Heme−Cu bound Aβ peptides: Spectroscopic characteri zation, reactivity, and relevance to Alzheimer’s disease. *J. Am. Chem. Soc*. **2011**, *133*, 15545−15552.

17. Zhu, A.; Ding, C.; Tian, Y. A. Two-photon ratiometric fluorescence probe for cupric ions in live cells and tissues. *Sci. Rep*. **2013**, *3*, 1−6.

18. Margalioth, E. J.; Schenker, J. G.; Chevion, M. Copper and zinc levels in normal and malignant tissues. *Cancer* **1983**, *5*, 868-872.

19. Diez, M.; Arroyo, M.; Cerdan, F. J.; Munoz, M.; Martin, M. A.; Balibrea, J. L. Serum and tissue trace metal levels in lung cancer. *Oncology* **1989**, *4*, 230-234.

20. Roland, K. Fluorescent chemosensors for Cu^{2+} ions: Fast, selective, and highly sensitive. *Angew. Chem. Int. Ed*. **1998**, *37*, 772-773.

21. Jung, J. Y.; Kang, M.; Chun, J.; Lee, J.; Kim J, Kim, J.; Lee, Y.; Kim, S. J.; Lee, C.; Yoon, J. A thiazolothiazole based Cu^{2+} selective colorimetric and fluorescent sensor via unique radical formation. *Chem. Commun*. **2013**, *49*, 176–178.

22. Kaur, N.; Kumar, S. Single molecular colorimetric probe for simultaneous estimation of Cu^{2+} and Ni^{2+}. *Chem. Commun*. **2007**, *29*, 3069–3070.

23. Miller, E. W.; Zeng, L.; Domaille, D. W.; Chang, C. J. Preparation and use of copper sensor-1, a synthetic fluorophore for live-cell copper imaging. *Nat. Protoc*. **2006**, *1*, 824–827.

24. Hirayama, T.; VanDebittner, B. G. C.; Gray L. W.; Lutsenko, S.; Chang, C. J. Near Infrared fluorescent sensor for in vivo copper imaging in a murine wilson disease model. *Proc. Natl. Acad. Sci. USA*. **2012**, *109*, 2228–2233.

25. Li, X.; Gao, X.; Shi, W.; Ma, H. Design strategies for water-soluble small molecular chromogenic and fluorogenic probes. *Chem. Rev*. **2014**, *114*, 590−659.

26. Singh, A. K.; Mehtab, S.; Jain, A. K. Selective electrochemical sensor for copper(II) ion based on chelating ionophores. *Anal. Chim. Acta* **2006**, *575*, 25–31.

27. Singh, L. P.; Bhatnagar, J. M. Copper(II) selective electrochemical sensor based on Schiff base complexes. *Talanta* **2004**, *64*, 313–319.

28. Yang, W.; Gooding, J. J.; Hibbert, D. B. Redox voltammetry of sub-parts per billion levels of Cu^{2+} at polyaspartate-modified gold electrodes. *Analyst* **2001**, *126*, 1573–1577.

29. Lin, T. W.; Huang, S. D. Direct and simultaneous determination of copper, chromium, aluminum, and manganese in urine with a multielement graphite furnace atomic absorption spectrometer. *Anal. Chem*. **2001**, *73*, 4319−4325.

30. Pourreza, N.; Hoveizavi, R. Simultaneous preconcentration of Cu, Fe and Pb as methylthymol blue complexes on naphthalene adsorbent and flame atomic absorption determination. *Anal. Chim. Acta* **2005**, *549*, 124−128.

31. Liu, Y.; Liang, P.; Guo, L. Nanometer titanium dioxide immobilized on silica gel as sorbent for preconcentration of metal ions prior to their determination by inductively coupled plasma atomic emission spectrometry. *Talanta* **2005**, *68*, 25−30.

32. Becker, J. S.; Matusch, A.; Depboylu, C.; Dobrowolska, J.; Zoriy, M. V. Quantitative imaging of selenium, copper, and zinc in thin sections of biological tissues (slugs-genus arion) measured by laser ablation inductively coupled plasma mass spectrometry. *Anal. Chem*. **2007**, *79*, 6074−6080.

33. Auzel, F. Upconversion and anti-stokes processes with f and d ions in solids. *Chem. Rev.* **2004**, *104*, 139-174.

34. Xiang, J.; Xu, l.; Gong, H.; Zhu, W.; Wang, C.; Xu, J.; Feng, l.; Cheng, l.; Peng, R.; liu. Z. Antigen-loaded upconversion nanoparticles for dendritic cell stimulation, tracking, and vaccination in dendritic cell-based immunotherapy. *ACS Nano* **2015**, *9*, 6401–6411.

35. Cheng, L.; Yang, K.; Shao, M.; Lee, S. T.; Liu, Z. Multicolor in vivo imaging of upconversion nanoparticles with emissions tuned by luminescence resonance energy transfer. *J. Phys. Chem. C* **2011**, *115*, 2686–2692.

36. Li, K.; Su, Q.; Yuan, W.; Tian, B.; Shen, B.; Li, Y.; Feng, W.; Li. F. Ratiometric monitoring of intracellular drug release by an upconversion drug delivery nanosystem. *ACS Appl. Mater. Interfaces* **2015**, *7*, 12278–12286.

37. Wang, X.; Yang, C. X.; Chen, J. T.; Yan, X. P. A dual-targeting upconversion nanoplatform for two-color fluorescence imaging-guided photodynamic therapy. *Anal. Chem*. **2014**, *86*, 3263–3267.

38. Vetrone, F.; Naccache, R.; Zamarrón, A.; Fuente, A. J.; Rodríguez, F. S.; Maestro, L. M.; Rodriguez, E. M.; Jaque, D.; Solé, J. G.; Capobianco, J. A. Temperature sensing using fluorescent nanothermometers. *ACS Nano* 2010, *4*, 3254–3258.

39. Selvin, P. R.; Rana T. M.; Hearst, J. E. Luminescence resonance energy transfer. *J. Am. Chem. Soc*. **1994**, *116*, 6029-6030.

40. Raj, J. G. J.; Quintanilla, M.; Mahmoud, K. A.; Ng, A.; Vetrone, F.; Zourob. M. Sensitive detection of ssDNA using an LRET-based upconverting nanohybrid material. *ACS App. Mater. Interfaces* **2015**, *7*, 18257−18265.

41. Ju, Q.; Uddayasankar, U.; Krull. U. Paper-based DNA detection using lanthanide-doped $LiYF_4$ upconversion nanocrystals as bioprobe. *Small* **2014**, *10*, 3912–3917.

42. Lu, Y.; Zhao, J.; Zhang, R.; Liu, Y.; Liu, D.; Goldys, E. M.; Yang, X.; Xi, P.; Sunna, A.; Lu, J.; Shi, Y.; Leif, R. C.; Huo, Y.; Shen, J.; Piper, J. A.; Robinson, J. P.; Jin, D. Tunable lifetime multiplexing using luminescent nanocrystals. *Nat. Photon.* **2014**, *8*, 32-36.

43. Liu. J. L.; Cheng, J. T.; Zhang, Y. Upconversion nanoparticle based LRET system for sensitive detection of MRSA DNA sequence. *Biosens. Bioelectron*. **2013**, *43*, 252-256.

44. Liu, C. H.; Chang, L. J.; Wang, H. H.; Bai, J.; Ren, W.; Li, Z. P. Upconversion nanophosphor: an efficient phosphopeptides-recognizing matrix and luminescence resonance energy transfer donor for robust detection of protein kinase. *Anal. Chem*. **2014**, *12*, 6095-6102.

45. Ye, W. W.; Tsang, M. K.; Liu, X.; Yang, M. Hao, J. Upconversion luminescence resonance energy transfer (LRET)-based biosensor for rapid and ultrasensitive detection of avian influenza virus H7 subtype. *Small* **2014**, *10*, 2390-2397.

46. Vetrone, F.; Naccache, R.; Mahalingam, V.; Morgan, C. G.; Capobianco, J. A. Luminescence resonance energy transfer from an upconverting nanoparticle to a fluorescent phycobiliprotein. *Nanoscale* **2010**, *2*, 1185-1189.

47. Deng, W.; Goldys. E. M. Chemical sensing with nanoparticles as optical reporters: from noble metal nanoparticles to quantum dots and upconverting nanoparticles. *Analyst*, **2014**, *139*, 5321-5334.

48. Ahn, J. C.; Kang, J. W.; Shin, J. I.; Chung, P. S. Combination treatment with photodynamic therapy and curcumin induces mitochondria-dependent apoptosis in AMC-HN3 cells. *Int. J. Oncol*. **2012**, *41*, 2184-2190.

49. Leite, D. P.; Paolillo, F. R.; Parmesano, T. N.; Fontana, C. R.; Bagnato, V. S. Effects of photodynamic therapy with blue light and curcumin as mouth rinse for oral disinfection: A randomized controlled trial. *Photomed. Laser Surg*. **2014**, *32*, 627-632.

50. Koon, H.; Leung, A. W.; Yue, K. K.; Mak, N. K. Photodynamic effect of curcumin on NPC/CNE2 cells. *J. Environ. Pathol. Toxicol. Oncol*. **2006**, *25*, 205-215.

51. Rao, C. V.; Rivenson, A.; Simi, B.; Reddy, B. S. Chemoprevention of colon carcinogenesis by dietary curcumin, a naturally-occurring plant phenolic compound. *Cancer Res*. **1995**, *55*, 259−266.

52. Lim, G. P.; Chu, T.; Yang, F. S.; Beech, W.; Frautschy, S. A.; Cole, G. M. The curry spice curcumin reduces oxidative damage and amyloid pathology in an Alzheimer transgenic mouse. *J. Neurosci*. **2001**, *21*, 8370−8377.

53. Ono, K.; Hasegawa, K.; Naiki, H.; Yamada, M. Curcumin has potent anti-amyloidogenic effects for Alzheimer's β-amyloid fibrils in vitro. *J. Neurosci*. *Res*. **2004**, *75*, 742−750.

54. Lantz, R. C.; Chen, G. J.; Solyom, A. M.; Jolad, S. D.; Timmermann, B. N. The effect of turmeric extracts on inflammatory mediator production. *Phytomedicine* **2005**, *12*, 445−452.

55. Salem, M.; Rohanib, S.; Gillies. E. R. Curcumin, a promising anti-cancer therapeutic: a review of its chemical properties, bioactivity and approaches to cancer cell delivery. *RSC Adv*. **2014**, *4*, 10815–10829.

56. Kawamori, T.; Lubet, R.; Steele, V. E.; Kelloff, G. J.; Kaskey, R. B.; Rao, C. V.; Reddy, B. S. Chemopreventive effect of curcumin, a naturally occurring anti-inflammatory agent, during the promotion/progression stages of colon cancer. *Cancer Res*. **1999**, *59*, 597-601.

57. Kakarala, M.; Brenner, D. E.; Korkaya, H.; Cheng, C.; Tazi, K.; Ginestier, C.; Liu, S.; Dontu, G.; Wicha, M. S. Targeting breast stem cells with the cancer preventive compounds curcumin and piperine. *Breast Cancer Res. Treat*. **2010**, *122*, 777-785.

58. Chan, M. M.; Huang, H. I.; Fenton, M. R.; Fong, D. In vivo inhibition of nitric oxide synthase gene expression by curcumin, a cancer preventive natural product with anti-inflammatory properties. *Biochem. Pharmacol*. **1998**, *55*, 1955-1962.

59. Genger, U. R.; Grabolle, M.; Jaricot, S. C.; Nitschke, R.; Nann, T. Quantum dots versus organic dyes as fluorescent labels. *Nat. Methods* 2008, *5*, 763-775.

60. Mahalingam, V.; Vetrone, F.; Naccache, R.; Speghini, A.; Capobianco, J. A. Colloidal Tm^{3+}/Yb^{3+} doped $LiYF_4$ nanocrystals: Multiple luminescence spanning the UV to NIR regions via low-energy excitation. *Adv. Mater*. **2009**, *21*, 4025-4028.

61. Leung, M. H. M.; Pham, D. T.; Lincoln, S. F.; Kee, T. W. Femtosecond transient absorption spectroscopy of Cu(II)–curcumin complexes. *Phys. Chem. Chem. Phys*. **2012**, *14*, 13580–13587.

62. Barik, A.; Mishraa, B.; Shenb, L.; Mohana, H.; Kadamc, R. M.; Duttad, S.; Zhangb, H. Y.; Priyadarsini. K. I. Evaluation of a new Cu(II)–curcumin complex as superoxide dismutase mimic and its free radical reactions. *Free Radic. Biol*. **2005**, *39*, 811–822.

63. Zhao, X. Z.; Jiang, T.; Wang, L.; Yang, H. Zhang, S.; Zhou. P. Interaction of curcumin with Zn(II) and Cu(II) ions based on experiment and theoretical calculation. *J. Mol. Struct*. **2010**, *984*, 316–325.

DOI : 10.1039/c5tb02555a

CHAPTER 5 – NEAR-INFRARED TRIGGERED GENERATION OF REACTIVE OXYGEN SPECIES FROM UPCONVERTING NANOPARTICLES DECORATED WITH AN ORGANOIRIDIUM COMPLEX

5.1 Abstract

Recently more effective generation of ROS in PDT has emerged as an indispensable tool for cancer research and treatment. The therapeutic mechanism of PDT relies on the in-situ photo-excitation of a suitable photosensitizer at its appropriate wavelength. To date, most of the commercially available photosensitizers use UV excitation for the generation of singlet oxygen to kill the cancer cells. However, excitation in the UV brings about many disadvantages among them; high scattering in biological media and low penetration depths are of much concern. In our present work, we address these issues by combining a water-soluble highly photoluminescent Ir complex with NIR sensitive UCNP. Use of NIR light to excite the UCNPs overcomes the scattering problem as well as the possibility of cellular imaging at higher penetration depths. For this purpose, we have constructed SiO_2 coated Tm^{3+}/Yb^{3+} co-doped $LiYF_4$ UCNPs decorated with highly photoluminescent Ir complex. Excitation of $LiYF_4$:Tm^{3+}, Yb^{3+} UCNP at 980 nm wavelength produces multiple sharp emissions ranging from deep UV to visible to NIR. Energy transfer between the UCNP and the locally decorated Ir complex would produce ROS, which in-turn, kills the tumor cells. Also one of the emission wavelengths from the UCNP would excite the photoluminescent Ir complex, which would emit red light in the visible region that is beneficial in cellular imaging.

5.2 Introduction

Over the course of the last few years, transition metal-based complexes have garnered a great deal of attention for a variety of applications [1,2]. In particular, Ir complexes are of significant interest due to their tunable properties, which can be altered by changing the ligands and their substituents around the metal center [3]. Their luminescence properties have been long studied since these luminescent complexes are well-known

CHAPTER 6 – SUPERPARAMAGNETIC IRON OXIDE NANOPARTICLES TAGGED WITH HETEROLEPTIC IRIDIUM PENDANTS FOR THE GENERATION OF REACTIVE OXYGEN SPECIES

6.1 Abstract

Core/shell superparamagnetic (Fe_3O_4) nanoparticles coated with a silica (SiO_2) shell (Fe_3O_4@SiO_2) have been synthesized and functionalized with a heteroleptic iridium (Ir) complex possessing excellent photoluminescent properties. The Fe_3O_4@SiO_2-Ir nanostructure proved to be an excellent nanocomposite material for the generation of reactive oxygen species (ROS) for potential application in photodynamic therapeutics (PDT). This water dispersible nanostructure could act as a trimodal nanoprobe due to its integrated magnetic, optical as well as PDT property. The Ir complex used in this work has significant advantages over most of the reported transition metal-based complexes due to the presence two bio-functionalizable carboxylic acid groups on one of its ligands. Here, we study the photophysical properties of the Fe_3O_4@SiO_2-Ir nanostructure and study its ability to generate ROS following optical excitation.

6.2 Introduction

Superparamagnetic iron oxide nanoparticles (SPIONs) have been studied extensively over the last decade owing to their tremendous potential in various biomedical applications. The interest from the research community stems primarily from their ease of synthesis with mild reaction conditions, facile surface functionalization chemistry, biocompatibility, and of course, excellent magnetic properties. SPIONs could be controlled by the application of an external magnetic field paving the way for targeted delivery of diverse cargo, including chemotherapeutics to cancer cells by incorporating drugs with the magnetic core nanoparticles [1]. Naturally, SPIONs also find applications in the field of imaging agents, magnetic separation in microbiology, and biochemical sensing [2-4]. To make the above potential applications of these SPIONs a reality, surface functionalization is required, especially since many of the synthesis techniques involve the use of organic solvent/ligands in the synthesis yielding hydrophobic nanoparticles [5]. One of the most versatile surface functionalization techniques to

render these SPIONs dispersible in water and other biological media (buffers for example), involves the growth of a layer of silica (SiO_2) on their surfaces. SiO_2 is chemically stable, biocompatible and can be easily used as a scaffold to covalently functionalize molecules for bio-conjugation purposes [5]. A large body of literature exists on the development of SPIONs with dual or multiple functionalities in order to endow these nanoparticle systems for various biomedical applications [6]. Given their propensity for integration in biomedical applications, there are many reports on the use of SPIONs in biology and nanomedicine [6]. SPIONS with a reasonably long retention time in the blood circulation, ability to biodegrade and low cytotoxicity are important factors that have allowed these nanoparticles to be used for biomedical [7] *in vivo* therapeutic applications [8], magnetic resonance imaging [9,10], bio-separation [11], catalysis [12] and cancer therapeutics [13].

With the advent of nanoscience, the synthesis of luminescent nanoparticles that can act as transducers in photodynamic therapy (PDT), in particular for cancer therapeutic applications has undergone a resurgence [14-16]. Different types of nanoparticles such as upconversion nanoparticles [17], inorganic quantum dots [18], graphene quantum dots [19] have been reported as triggers in PDT. The principle of PDT depends on the use of a photo-perturbable molecule called a sensitizer that becomes activated in the presence of molecular oxygen upon absorption of light at the appropriate wavelength. The result of this photo-induced process is the production of reactive oxygen species (ROS) such as free radicals and singlet oxygen and these highly reactive species are subsequently exploited to kill cancer cells. The major advantage of PDT is its non-invasive nature and the ease with which the cancer cells can be selectively targeted (when the cancer is surface based). However, direct dispensing of any photosensitizer may cause cellular damage to normal healthy cells and for this reason, encapsulation of the photosensitizer in nanoparticles is deemed appropriate [20, 21]. Although many groups have reported the use of magnetic nanoparticles for PDT, finding a suitable photosensitizer that shows stable luminescence with high quantum yield has been a challenge due to the photobleaching effects and reduced amount of singlet oxygen produced by such a hybrid system in a biological media owing to side reactions that could potentially lead to the formation of toxic byproducts [22-24]. Therefore, integration

of an efficient ROS generating photosensitizer and imaging agents on a single nanoparticle to develop a multimodal theranostic nanoplatform for potential application in PDT has been gaining interest in recent years [25-27].

In view of emerging applications of transition metal complexes in nanomedicine due to their tunable geometry, excellent photophysical and redox properites, novel transition metal based PDT agents have been investigated as replacements for organic molecule based PDT dyes such as porphyrins and phthalocyanins. The metal complexes offer additional advantages such as their ability to interact with DNA causing cleavage/damage [28]. In this respect transition metal complexes started to find applications in PDT since metal complexes can react with small molecules such as DNA directly from their excited state or could generate ROS in the solution [28, 29]. Recently research interests developed on the applications of other noble group metals such as platinum [30]. Interestingly enough, although iridium (Ir) belongs to the noble metals, its use as an effective PDT sensitizer has not been explored in great detail. In view of new opportunities for Ir in the field of PDT, in our present work, we have synthesized an integrated multimodal nanoprobe that is based on a highly photoluminescent Ir complex (Fe_3O_4@SiO_2-Ir). The nanohybrid material consisting of a superparamagnetic (Fe_3O_4) nanoparticle coated with a thin layer of silica (SiO_2) and subsequently functionalized with an organometallic Ir complex was thoroughly characterized and its ROS generating ability was demonstrated under UV excitation (Scheme 6.1).

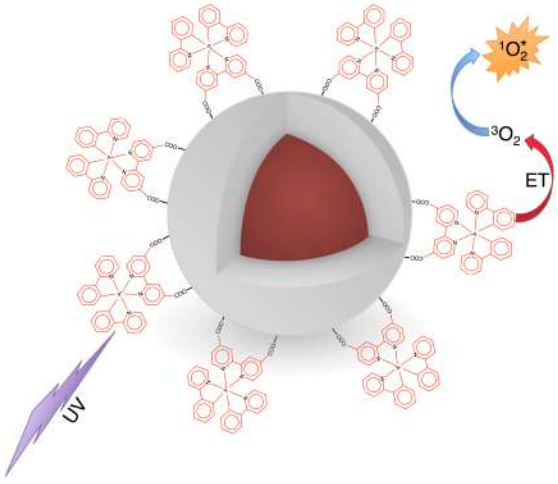

Scheme 6.1 Principle of ROS generation of SPION-Ir nanohybrid at direct UV excitation

6.3 Results and Discussion

6.3.1 Morphological Characterization

The core SPIONs were synthesized by the previously reported thermal decomposition method [31], however, with a slight modification where oleic acid was used as the surfactant and octadecene as the high boiling solvent in a two-step process. The hydrophobic SPIONs were then made dispersible in aqueous media by coating with a layer of SiO_2 using the commercially available surfactant Igepal [32]. The TEM images suggest that the SPIONs were uniform size with an average diameter of about 16 nm with a narrow size distribution (Figure 6.1, A-B) and following coating with SiO_2, the Fe_3O_4@SiO_2 SPIONs were of approximately 47 nm in diameter (Figure 6.1, C-D). The as obtained bare and SiO_2 coated SPIONs were characterized by XRD for structural analysis and crystallite size. The X-ray powder diffraction pattern of the sample was recorded on a Bruker D8 Advance diffractometer using Cu Kα radiation at λ = 0.154 nm operating at 45 kV and 40 mA at room temperature in the range of 20 to 70°. All the peaks of XRD patterns were analyzed and indexed using ICDD data-base, comparing with magnetite standard values [33]. The peaks indexed for SPIONS (220), (311), (400), (511), and (440) (JCPDS file No. 65-3107) corresponded to a cubic phase unit cell, confirming the cubic structure. The broad diffraction pattern of the SPIONS confirmed their sizes to be in nanoscale range. The other broad peak at 2θ = 24° is due to the amorphous silica coating on the surface of SPIONs.

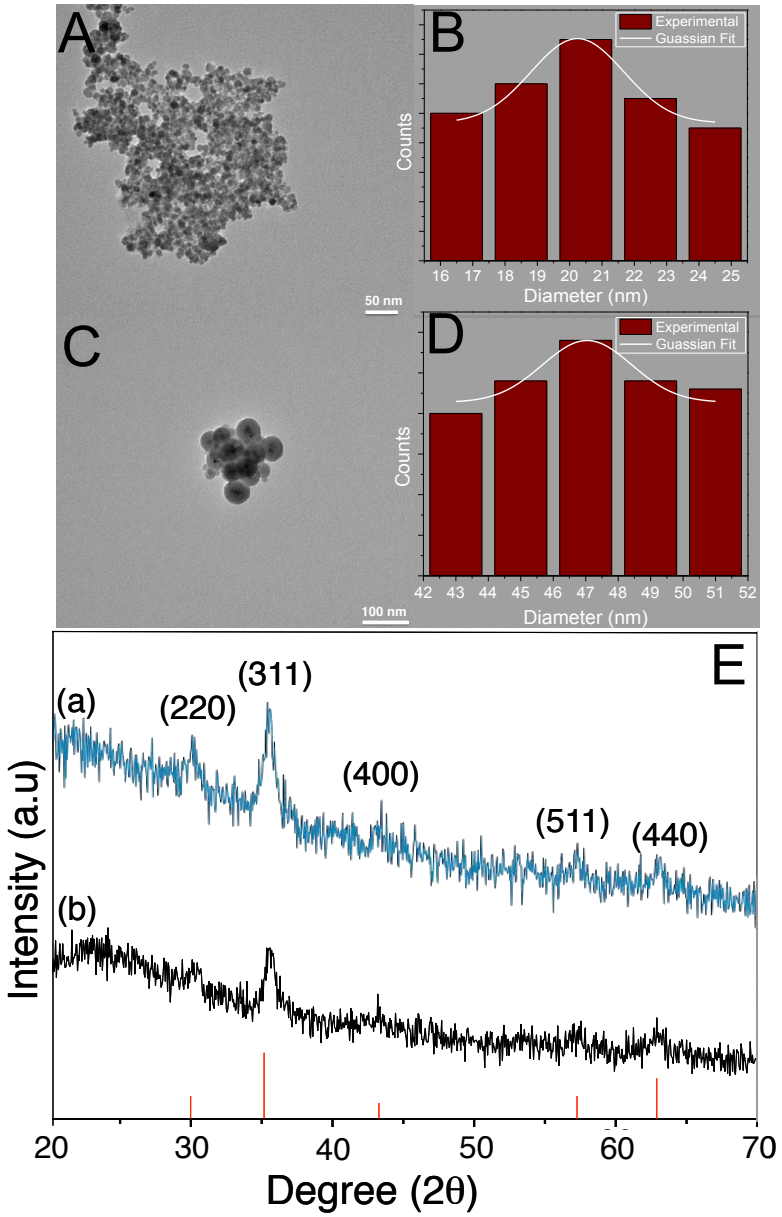

Figure 6.1 (A) and (C) are the TEM images of bare and SiO_2 coated SPIONs, respectively, with their respective particle size distribution histograms (B) and (D). (E) XRD pattern of the both bare (a) and SiO_2 coated (b) SPIONs (JCPDS file No. 65-3107).

6.3.2 Surface Characterization

The investigation of the surface functional groups of the SPIONs was carried out using Fourier transform infrared (FTIR) spectroscopy (Figure 6.2A). The FTIR spectrum of the parent SPIONs confirmed the presence of the oleate capping ligand due to the presence of the peaks at 1584 and 1698 cm^{-1} attributed to the symmetrical and asymmetrical stretching vibrations of carboxylate functional group [34]. Moreover, the FTIR spectrum also showed strong absorptions at 2847 and 2923 cm^{-1}, which were due

to the symmetrical and asymmetrical C–H stretching vibrations of the aliphatic chain of the surface oleate ligand. Furthermore, the band at 3438 cm^{-1} was due to the O–H stretching vibration of the oleic acid. The peak at 522 cm^{-1} was assigned to the presence of Fe-O coordinate bond vibration.

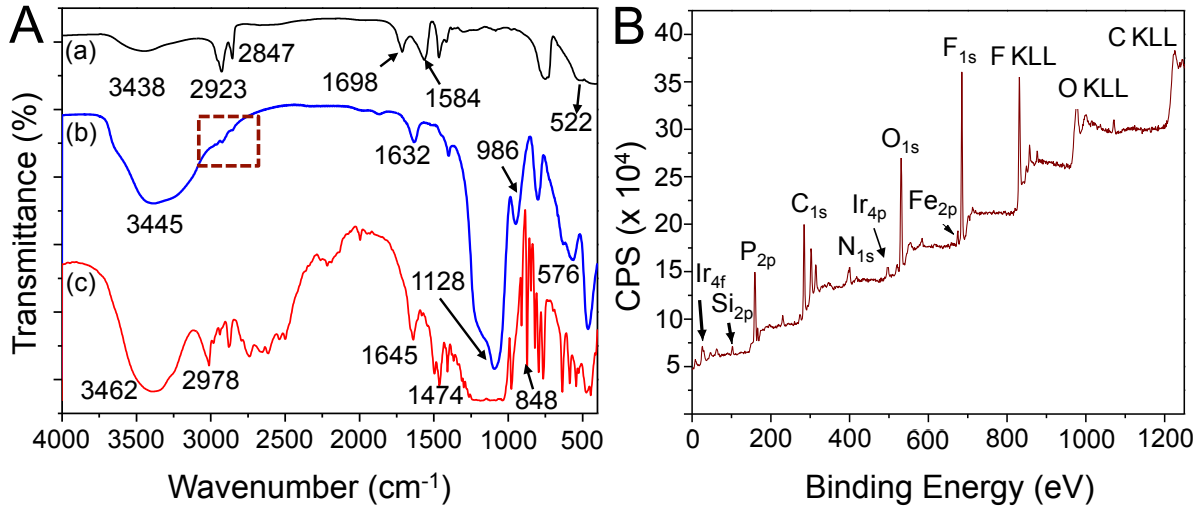

Figure 6.2 (A) FTIR Spectra of (a) oleate-capped Fe_3O_4 SPIONs; (b) SiO_2 coated Fe_3O_4 SPIONs (the broken square box indicates the reduced intensity of the symmetrical and asymmetrical stretching vibrations of C-H of oleate and (c) Ir complex decorated Fe_3O_4@SiO_2 (the Fe_3O_4@SiO_2-Ir) SPIONs. (B) XPS of the Fe_3O_4@SiO_2-Ir SPIONs.

The hydrophobic SPIONs were then rendered hydrophilic by surface modification by silica coating. The presence of SiO_2 on the SPION surface reduced the intensities of C–H symmetrical and asymmetrical vibrations of the oleate ligand (Figure 6.2 A(b)). Moreover, success of the SiO_2 coating was confirmed by the appearance of several new peaks in the spectrum including a new broad peak at 1128 cm^{-1}, which was due to the Si–O–Si stretching and a peak at 986 cm^{-1} due to Si–O–Si bending vibrations. The peak at 576 cm^{-1} was due to the Fe-O stretching vibration. This band intensity has slightly increased from the uncoated 522 cm^{-1} due to the availability of extensive oxygen at the interface between the SPION surface and SiO_2 and this resulted extensive Fe-O coordination. The successful decoration of the Ir complex on the Fe_3O_4@SiO_2 SPIONs (Fe_3O_4@SiO_2-Ir) was confirmed by the appearance of all the major functional groups in the FTIR spectrum. The peak at 3462 cm^{-1} was due to the O-H stretching vibration of the carboxyl functional groups of the Ir complex and the peaks at 2978, 1474 cm^{-1} were

due to the C-H stretching and aromatic C=C stretching frequencies, respectively, from the ligands of the Ir complex. Interestingly, the intensity of the peak at 1645 cm^{-1} was increased, due to C=O functional groups of the Ir complex at the SPION surface. Further confirmation is obtained from the intense peak at 848 cm^{-1}, which was due to P-F vibrations from the anionic part of the Ir complex. The FTIR results of the Fe_3O_4@SiO_2-Ir nanoparticles were further confirmed using X-ray photoelectron spectroscopy (XPS) as the presence of all the elements from Fe_3O_4, SiO_2 as well as the Ir complex at their respective binding energies were observed (Figure 6.2B).

6.3.3 Photophysical Characterization

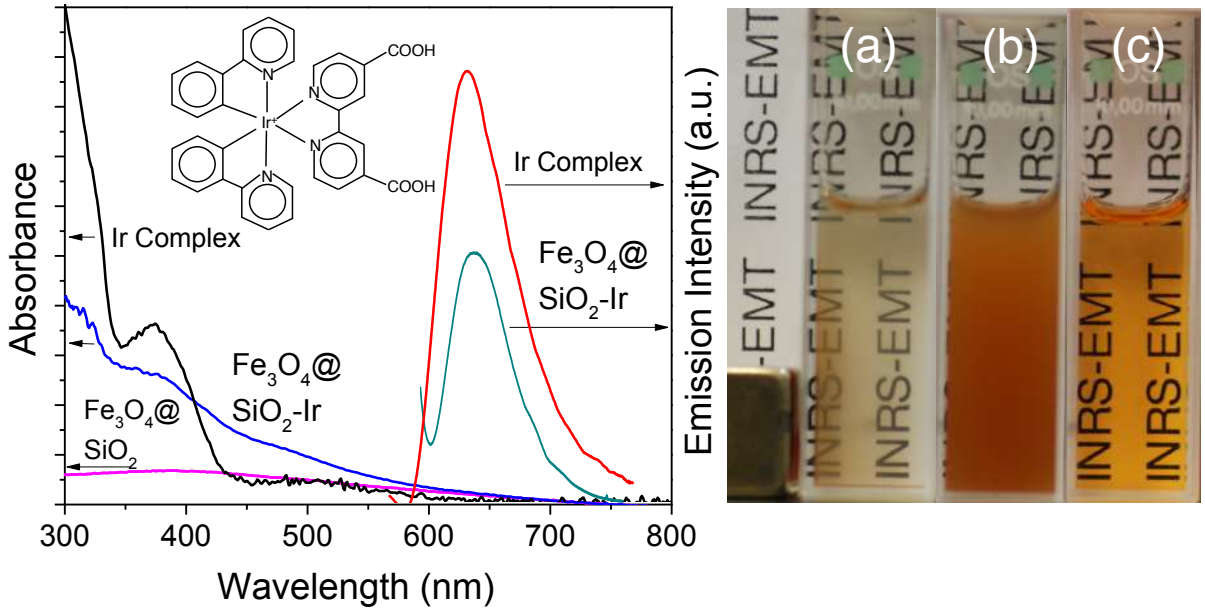

Figure 6.3 The UV-vis absorption and emission spectra of the Ir complex loaded SiO_2 coated SPIONs; inset is the molecular structure of the Ir complex (left); The optical images of (a) Fe_3O_4@SiO_2-Ir in the presence of (b) in the absence of magnet, (c) the cationic Ir complex alone in 1:1 ethanol:water solution.

The photophysical properties of the Ir decorated Fe_3O_4@SiO_2 SPIONs were thoroughly investigated and it is evident from the UV-visible spectra (Figure 6.3) that the Fe_3O_4@SiO_2 SPIONs did not show any significant absorption in the range where the Ir complex absorbs. However, when the complex was functionalized to the surface, the Fe_3O_4@SiO_2-Ir SPIONs showed two prominent absorption peaks at approximately 290 nm due to ligand centered $\pi \rightarrow \pi^*$ transition and at 380 nm due to metal-ligand charge

transfer. A less intense broad shoulder peak at 500 nm due to a weak n→π* transition was also observed. This clearly confirmed the functionalization of the Ir complex on the surface of the Fe_3O_4@SiO_2 SPIONs. In addition, the emission spectrum of Fe_3O_4@SiO_2-Ir SPIONs showed the characteristic Ir emission centered at 620 nm thus again confirming the presence of the Ir complex on the Fe_3O_4@SiO_2 SPIONs.

The Ir complex was functionalized on the surface of the Fe_3O_4@SiO_2 SPIONs using various Ir concentrations from 5 mM to 10 mM at 1 mM increments (Figure 6.4A). After functionalization, the supernatant Ir complex was removed for UV measurement and the loading efficiency was calculated to be 68%. The smaller size of the Fe_3O_4/SiO_2 SPIONs allowed for maximum loading while keeping the nanoparticle size less than 50 nm.

6.3.4 Generation of ROS with UV Excitation

The photosensitization effect of the Ir complex takes place under direct UV excitation, which results in the production of ROS. To evaluate the photosensitization effect of Ir complex when functionalized to the SPION, Fe_3O_4@SiO_2-Ir was dispersed in a solution containing the probe molecule DPBF. Direct excitation of Fe_3O_4@SiO_2-Ir with 360 nm UV radiation showed reduction in the absorption of DPBF since this probe reacts with the ROS ($^1O_2$*) and the decrease in absorption intensity is directly proportional to the amount of singlet oxygen produced in the sample [31,32]. To evaluate the release of ROS, the aqueous solution containing the Fe_3O_4@SiO_2-Ir SPIONs were sonicated for approximately 30 minutes and then added to 1 mL of DPBF solution.

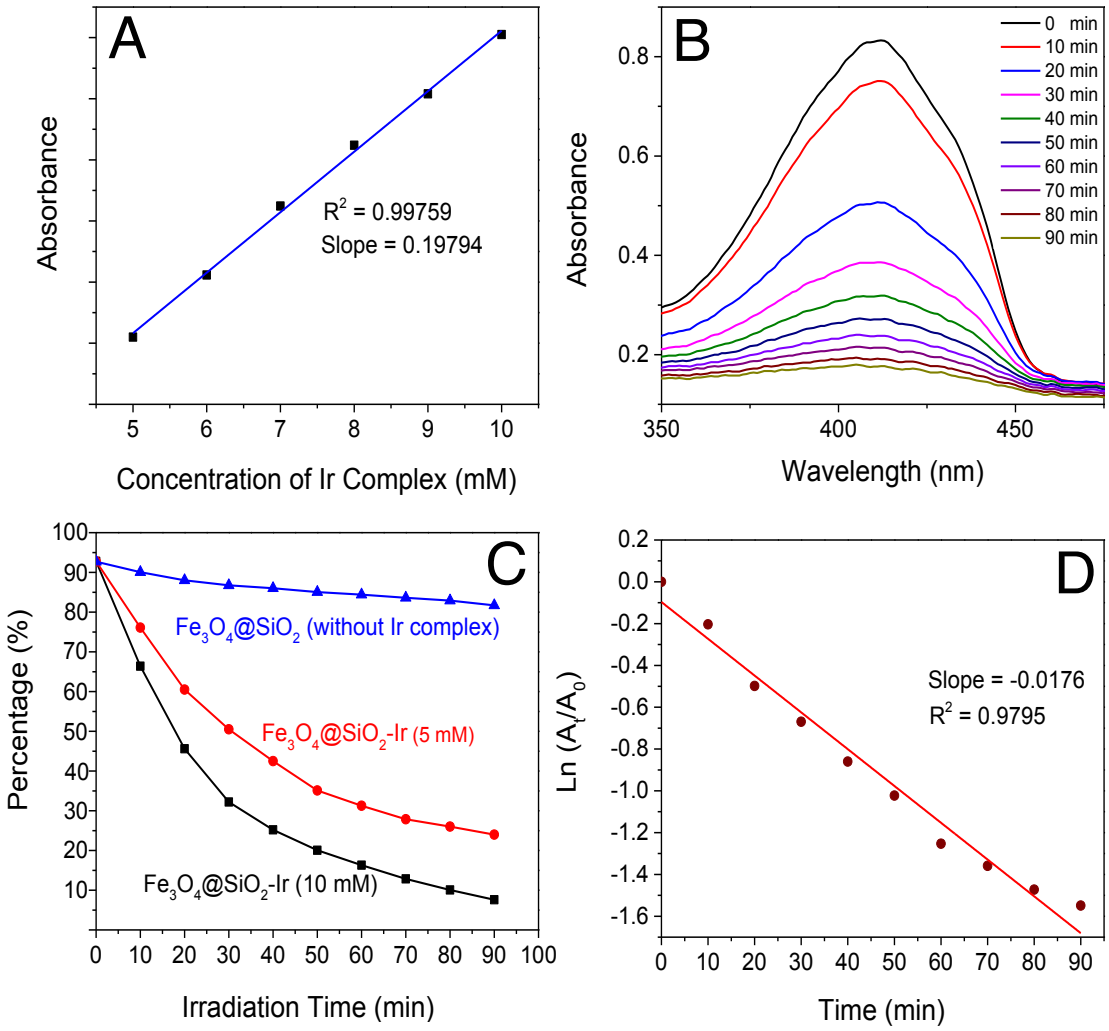

Figure 6.4 (A) Loading of the Ir complex on the SiO_2 coated magnetic nanoparticles. The loading percentage was calculated to be 68%. Increased loading showed increased absorbance confirming the successful encapsulation of the Ir complex on the surface of SiO_2. (B) Decrease in the absorption of the DPBF probe in the presence of Fe_3O_4@SiO_2 SPIONs decorated with the Ir complex at various time intervals. (C) Comparison of the absorbance peak of DPBF at 420 nm after 360 nm irradiation at different time intervals including Fe_3O_4@SiO_2 SPIONs without the Ir complex, Fe_3O_4@SiO_2 SPIONs functionalized with two different concentrations of Ir complex (5 mM and 10 mM). (D) Comparative plot of $\ln(A_t/A_0)$ as a function of time. A_0 is the initial absorbance, and A_t is the absorbance at different time intervals.

The resultant solution was covered in aluminium foil in order to protect the solution from natural light, which could interfere with the ROS production and subsequently affect the absorption measurements. The solution was then exposed to direct UV excitation at various time intervals with constant stirring and the absorption spectra of the solution

were recorded every ten minutes after irradiation (Figure 6.4B). The maximum absorbance of DPBF at 420 nm was plotted against the solution's exposure time (Figure 6.4C, black and magenta lines) and the results clearly demonstrate the steady decrease in the absorption of the DPBF probe when Ir complex was present on the Fe_3O_4@SiO_2 surface and hence confirmed the production of ROS. To evaluate that the production of ROS was solely due to the presence of the Ir complex, a control experiment was carried out. We investigated the Fe_3O_4@SiO_2 SPIONs alone (in the absence of the Ir complex) to ascertain whether it could be responsible for the ROS generation. As shown in Figure 6.4C (blue curve), no ROS was produced after UV excitation at multiple time intervals. Furthermore, we also investigated the efficiency of ROS production with different concentrations of Ir complex (5 mM and 10 mM) functionalized on the Fe_3O_4@SiO_2 SPIONs. As expected, higher concentration of Ir complex on the surface of the SPIONs produced a much faster decomposition of the probe DPBF molecule (black line) thus clearly confirming the role of singlet oxygen production by the Ir complex. Figure 6.4D presents the logarithmic ratio between the absorbance (A_t) of the probe DPBF molecule in the presence of the Fe_3O_4@SiO_2-Ir SPIONs at various time intervals after 360 nm UV irradiation, and its original value (A_0) before irradiation. The plot gives an excellent linear fit with a negative slope of 0.0176 corresponding to the photo-oxidation rate of the DPBF molecule. The negative slope confirms the fact that absorbance of the probe decreases when UV irradiation time increases with an excellent linear regression value of 0.9795.

6.4 Experimental Section

6.4.1 Materials and Chemicals

$FeCl_3 \cdot 6H_2O$, sodium oleate, oleic acid, triethylamine, IGEPAL CO-520, tetraethylorthosilicate (TEOS), 2-phenylpyridine, $IrCl_3 \cdot 3H_2O$, 2-ethoxyethanol, 2,2'-bipyridine-4,4'-dicarboxylic acid, sodium acetate, ammonium hexafluorophosphate, 1,3-Diphenylisobenzofuran (DPBF) (97%) were purchased from Aldrich. Solvents such as n-hexanol, methanol, hexane, toluene, ethanol, dichloromethane, acetone were obtained from Alfa Aesar. Ultrapure water (Millipore) of resistivity greater than 18.0 MΩ cm was used in all experiments. All chemicals were used as received unless specified.

6.4.2 Instrumentation

The Fourier-transform infrared (FTIR) spectra were recorded on a Thermoscientific Nicolet Spectrometer using FTIR grade KBr as the background. Transmission Electron Microscopy (TEM) images were obtained with a Philips Tecnai 12 (120 kV) microscope. To observe the morphology and size distribution of the SPIONs, 10 mg of the parent (uncoated) and SiO_2 coated SPION samples were dispersed in 10 g of hexane and ethanol, respectively, and sonicated for 1 h. A drop of the resulting solution was evaporated on a formvar/carbon film supported on a 300 mesh copper grid (3 mm in diameter). X-ray photoelectron spectroscopy (XPS) analyses were performed on a VG Escalab 220i XL instrument equipped with 6 channeltrons using a non-monochromated Mg K X-ray source (1253.6 eV). To identify the phase of the SPIONs, X-ray diffraction (XRD) patterns were recorded using a Bruker D8 Advance Powder Diffractometer with Cu Kα radiation at λ = 0.154 nm operating at 45 kV and 40 mA. The UV-Vis absorption measurements were carried out using a Thermoscientific 2000 spectrophotometer.

6.4.3 Synthesis of oleate-capped SPIONs (Fe_3O_4)

The oleate-capped hydrophobic SPIONs were synthesized as reported earlier [31] with slight modification. First, the iron-oleate precursor was synthesized which was later converted into smaller iron oxide magnetic nanoparticles (Fe_3O_4 SPIONs). For the synthesis of the precursor material, 18.25 g (120 mmol) sodium oleate and 5.4 g (40 mmol) ferric chloride hexahydrate were dissolved in a mixture of 60 mL ethanol,

80 mL MilliQ water, and 160 mL hexane. This mixture was refluxed at 75 °C for 5 h under an argon atmosphere. After the reaction, the organic layer that contains the iron-oleate complex was separated. The organic layer was removed using a rotary evaporator and the resultant dark brown viscous liquid was retrieved. In the second step of the synthesis, about 18 g of as synthesized iron oleate precursor was treated with 2.9 g of oleic acid in the presence of 100 mL of octadecene. The resultant solution was purged with argon gas to remove air and moisture in the solvent for about 30 min and slowly heated to 300 °C. The solution was kept at this temperature for 30 min. Between 200 and 250 °C, decarboxylation of the oleate from the iron oleate precursor starts to liberate carbon dioxide gas (Note: *it is highly recommended that this step of the reaction must be carried out in a well-ventilated fume hood*). After the reaction was complete, the solution was cooled down to the room temperature and an excess amount of ethanol was added to precipitate the SPIONs. The product was then washed several times with ethanol and acetone to remove any soluble impurities. Finally, the oleate-capped hydrophobic SPIONs were dispersed in hexane.

6.4.4 Synthesis of silica coated SPIONs (Fe_3O_4@SiO_2)

Silica coating of the SPIONs was performed as previously reported by Larsen *et al*. [32]. First, 10 mg of the oleate-capped SPIONs were dispersed in 2 mL of hexane and sonicated for 30 min. To this dispersion, 1.5 mL of triethylamine, 50 μL of TEOS and 200 μL of Igepal surfactant was added and ultrasonicated for another 30 min. The resultant emulsion was stirred for 4 h at room temperature. Then, about 10 mL of acetone was added to precipitate the Fe_3O_4@SiO_2 SPIONs and separated using an external magnet. The precipitate was washed several times with ethanol and finally the Fe_3O_4@SiO_2 SPIONs were dispersed either in water or PBS buffer solution.

6.4.5 Synthesis of Ir Complex

(i) Synthesis of precursor complex $[(ppy)_2Ir(\mu\text{-}Cl)]_2$ The Ir complex was synthesized according to the following procedure. Briefly, a mixture of 2-phenylpyridine (0.34 g, 2.2 mmol), $IrCl_3 \cdot 3H_2O$ (0.34g, 1 mmol) in a mixed solvent of 2-ethoxyethanol (15 mL) and water (5 mL) was stirred under N_2 at 120 ^oC for 20 h. The precipitate was then cooled to

room temperature and collected by filtration and washed with water, ethanol, acetone respectively, and subsequently dried in vacuum to give the $[(ppy)_2Ir(\mu\text{-}Cl)]_2$ dimer complex.

^{1}H NMR (500 MHz, $CDCl_3$) *δ*: 9.26 (d, *J* = 5.5 Hz, 1H), 7.96 (d, *J* = 8 Hz, 1H), 7.82 (t, *J* = 7.5 Hz, 1H), 7.58 (d, *J* = 7.5 Hz, 1H), 6.85 (m, 2H), 6.63 (t, *J* = 7.5 Hz, 1H), 5.89 (d, *J* = 8 Hz, 1H). ^{13}C NMR (125 MHz, acetone-d6) δ: 168.2 151.8 143.5 144.1 135.7 132.4 129.7 126.8 121.8 121.6 119.8 ppm. Calcd for $C_{44}H_{32}Cl_2Ir_2N_4$: C, 49.29; H, 3.01; N, 5.23. Found: C, 49.32; H, 3.07; N, 5.24. ESI-MS: 1072 [M^+].

(ii) Synthesis of $[(ppy)_2Ir(dcbpy)]^+PF_6^-$ $[(ppy)_2Ir(\mu\text{-}Cl)]_2$ (0.21 g, 0.2 mmol) was prepared as a solution in dichloromethane (15 mL) and added to a suspension of 2,2'-bipyridine-4,4'-dicarboxylic acid (0.098 g, 0.4 mmol) in methanol (20 mL). The reaction mixture was then heated to reflux with stirring for 4 h. To this solution, sodium acetate (excess) in methanol (5 mL) was added, and the mixture was stirred for a further 45 min. The solvent was then removed under reduced pressure, hydrochloric acid (1 M, 10 mL) was added, and the suspension was stirred for 20 min. The product was then filtered, washed with water (2 × 25 mL), vacuum dried, and the solid was then dissolved in methanol. A saturated solution of ammonium hexafluorophosphate in methanol (5 mL) was then added, and the mixture was stirred for a further 45 min. The solvent was removed under reduced pressure, and the residue was extracted into dichloromethane and filtered. The solvent was removed under reduced pressure to yield $[(ppy)_2Ir(dcbpy)]^+$ PF_6^- as a dark-red powder. The crude product was flash chromatographed on silica gel using CH_2Cl_2 as an eluent to afford the desired Ir(III) complex. (0.16 g, 69%).

^{1}H NMR (500 MHz, $CDCl_3$) *δ*: 6.32 (d, *J* = 5.9 Hz, 2H), 6.24 (t, *J* = 7.22 Hz, 2H), 6.54 (m, 2H), 6.64 (t, *J* = 7.46Hz, 2H), 7.22 (t, *J* = 7.34Hz, 2H), 7.52 (d, *J* = 7.50Hz, 2H), 7.48 (t, *J* = 7.50Hz, 2H), 7.58 (t, *J*=7.56Hz, 2H), 7.83(m, 2H), 8.46 (d, *J* = 5.52 Hz, 2H), 9.38 (s, 2 H). ^{13}C NMR (125 MHz, acetone-d6) δ: 121.08, 123.85, 124.77, 125.77, 126.07, 129.29, 131.53, 132.6, 139.91, 142.41, 145.05, 150.59, 150.82, 152.83, 157.77, 165.56, 168.65 ppm. mp (^{o}C): 194.5 Calcd for $C_{34}H_{24}F_6N_4O_4IrP$: C, 45.87; H, 2.69; N, 6.31. Found: C, 46.13; H, 2.84; N, 6.74. IR (KBr): *v* 2934 (s, OH), 1726 (s, CO), 852 (s, PF) cm^{-1}. ESI-MS: 745 [M^+]

6.4.6 Synthesis of Ir complex functionalized SPION@SiO_2-Ir (Fe_3O_4@SiO_2-Ir)

10 mg of the Ir complex was dissolved in 20 mL of ethanol containing the Fe_3O_4@SiO_2 SPIONs. After stirring for 12 h, the Fe_3O_4@SiO_2 SPIONs functionalized with the Ir complex (Fe_3O_4@SiO_2-Ir) were separated by centrifugation and washed several times with ethanol. Loading efficiency of the Ir complex on the Fe_3O_4@SiO_2 SPIONs was measured by UV-Vis absorption spectroscopy and determined to be 68%.

6.4.7 Detection of ROS

The generation of ROS was measured using the 1,3-diphenylisobenzofuran (DPBF) probe. In a typical process, 10 mg of the SPION@SiO_2-Ir SPIONs were well dispersed in 1 mL of DPBF solution (2.5 x 10^{-5} M in 1:1 water:ethanol mixture) with ultrasonic processing in the dark. The mixture was irradiated using a 360 nm UV lamp at 10 min time intervals and its absorption was measured by UV-Visible spectroscopy to monitor the change in absorption of DPBF at 420 nm. The decrease in absorption of the DPBF confirmed the generation of ROS.

6.5 Conclusion

In summary, we have synthesized monodispersed small core SPIONs (21 nm) and coated them with a layer of SiO_2 to render them water or buffer dispersible as well as make them amenable for Ir complex functionalization. The Fe_3O_4@SiO_2 SPIONs were then subsequently functionalized with different concentrations of a heteroleptic Ir complex at their surface and the photophysical properties of these Fe_3O_4@SiO_2-Ir SPIONs were evaluated. This nanohybrid showed strong emission maxima at 620 nm upon UV excitation due to the presence of surface tagged Ir complex. The presence of Ir complex acts as a photosensitizer and offers the generation of ROS under UV excitation. To confirm that the generation of ROS was only due to the Ir complex functionalization, a control experiment was carried out without the Ir complex on the surface of Fe_3O_4@SiO_2 SPIONs and no change was observed in the absorption of the DPBF probe thereby confirming that no ROS was produced for Fe_3O_4@SiO_2. When the same experiment was performed on Fe_3O_4@SiO_2-Ir SPIONs, the absorption intensity of the DPBF probe reduced significantly thus confirming the role of the Ir complex in the

production ROS production. The ROS generation was evaluated for two concentrations of the Ir complex (5 and 10 mM) functionalized on the surface of Fe_3O_4@SiO_2. The Fe_3O_4@SiO_2-Ir SPION with higher Ir concentration showed enhanced ROS generation compared to the one with lower Ir concentration again confirming that the presence of the Ir complex is necessary to realize improved efficiency in the ROS generation. This new multimodal Fe_3O_4@SiO_2-Ir nanoplatform paves the way for combined bio-imaging as well as photodynamic therapy due to the presence of the highly luminescent Ir complex and its efficiency in ROS production.

6.6 References

1. Ulbrich, K.; Holá, K.; Subr, V.; Bakandritsos, A.; Tuček, J.; Zbořil, R. Targeted drug delivery with polymers and magnetic nanoparticles: covalent and non-covalent approaches, release control, and clinical studies. *Chem. Rev.* **2016**, *116*, 5338–5431.

2. Gupta, A. K.; Gupta, M. Synthesis and surface engineering of iron oxide nanoparticles for biomedical applications. *Biomaterials* **2005**, *26*, 3995-4021.

3. Olsvik, R.; Popovic, T.; Skjerve, E.; Cudjoe, K. S.; Hornes, E.; Ugelstad, J.; Uhlen, M. Magnetic separation techniques in diagnostic microbiology. *Clin. Microbiol. Rev*. **1994**, *7*, 43- 54.

4. Widjojoatmodjo, M. N.; Fluit, A. C.; Torensma, R.; Verhoef, J. Comparison of immunomagnetic beads coated with protein A, protein G, or goat anti-mouse immunoglobulins. Applications in enzyme immunoassays and immunomagnetic separations. *J. Immunol. Methods* **1993**, *165*, 11-19.

5. Hao, R.; Xing, R.; Xu, Z.; Hou, Y.; Gao, S.; Sun, S. Synthesis, functionalization, and biomedical applications of multifunctional magnetic nanoparticles. *Adv. Mater*. **2010**, *22*, 2729-2742.

6. Gao, J.; Gu, H.; Xu, B. Multifunctional magnetic nanoparticles: Design, synthesis, and biomedical applications. *Acc. Chem. Res*. **2009**, *42*, 1097-1107.

7. Lee, J. H.; Huh, Y. M.; Jun, Y. W.; Seo, J. W.; Jang, J. T.; Song, H. T.; Kim, S.; Cho, E. J.; Yoon, H. G.; Suh, J. S.; Cheon, J. Artificially engineered magnetic nanoparticles for ultra-sensitive molecular imaging. *Nat. Med.* **2007**, *13*, 95-99.

8. Wang, L.; Bai, J.; Li, Y.; Huang, Y. Multifunctional nanoparticles displaying magnetization and near-IR absorption. *Angew. Chem. Int. Ed*. **2008**, *47*, 2439-2442.

9. Sun, C.; Lee, J. S. H.; Zhang, M. Magnetic nanoparticles in MR imaging and drug delivery. *Adv. Drug. Deliv. Rev*. **2008**, *60*, 1252–1265.

10. Na, H. B.; Song, I. C.; Hyeon. T. Inorganic nanoparticles for MRI contrast agents. **2009**, *21*, 2133–2148.

11. Vestal, C. R.; Zhang, Z. J. Synthesis and magnetic characterization of Mn and Co spinel ferrite-silica nanoparticles with tunable magnetic core. *Nano Lett*. **2003**, *3*, 1739–1743.

12. Lee, J.; Lee, Y.; Youn, J. K.; Na, H. B.; Yu, T.; Kim, H.; Lee, S. M.; Koo, Y. M.; Kwak, J. H.; Park, H. G.; Chang, H. N.; Hwang, M.; Park, J. G.; Kim, J.; Hyeon, T. Simple synthesis of functionalized superparamagnetic magnetite/silica core/shell nanoparticles and their application as magnetically separable high-performance biocatalysts. *Small* **2008**, *4*, 143-152.

13. Thorat, N. D.; Bohara, R. A.; Malgras, V.; Tofail, S. A. M.; Ahamad, T.; Alshehri, S.M.; Wu, K. C. W.; Yamauchi, Y. Multimodal superparamagnetic nanoparticles with unusually enhanced specific absorption rate for synergetic cancer therapeutics and magnetic resonance imaging. *ACS Appl. Mater. Interfaces* **2016**, *8*, 14656–14664.

14. Kim, K. S.; Kim, J.; Lee, J. Y.; Matsuda, S.; Hideshima, S.; Mori, Y.; Osaka, T.; Naa, K. Stimuli-responsive magnetic nanoparticles for tumor-targeted bimodal 5 imaging and photodynamic/hyperthermia combination therapy. *Nanoscale* **2016**, *8*, 11625-11634.

15. Wang, D.; Fei, B.; Halig, L. V.; Qin, X.; Hu, Z.; Xu, H.; Wang, Y. A.; Chen, Z.; Kim, S.; Shin, D. M.; Chen. Z. G. Targeted iron-oxide nanoparticle for photodynamic therapy and imaging of head and neck cancer. *ACS Nano* **2014**, *8*, 6620–6632.

16. Zhao, X.; Chen, Z.; Zhao, H.; Zhanga, D.; Taoa, L.; Lan. M. The multifunctional magnetic nanoparticles for simultaneous cancer near-infrared imaging and targeting photodynamic therapy. *RSC Adv.* **2014**, *4*, 62153-62159.

17. Idris, N. M.; Gnanasammandhan, M. K.; Zhang, J.; Ho, P. C.; Mahendran, R.; Zhang, Y. *In vivo* photodynamic therapy using upconversion nanoparticles as remote-controlled nanotransducers. *Nat. Med.* **2012**, *18*, 1580–1585.

18. Tsay, J. M.; Trzoss, M.; Shi, L.; Kong, X.; Selke, M.; Jung, M.E.; Weiss. S. Singlet oxygen production by peptide-coated quantum dot-photosensitizer conjugates. *J. Am. Chem. Soc*. **2007**, *129*, 6865-6871.

19. Ge, J.; Lan, M.; Zhou, B.; Liu, W.; Guo, L.; Wang, H.; Jia, Q.; Niu, G.; Huang, X.; Zhou, H.; Meng, X.; Wang, P.; Lee, C. S.; Zhang, W.; Han, X. A graphene quantum dot photodynamic therapy agent with high singlet oxygen generation. *Nat. Commun*. **2014**, *5:4596*, 1-10.

20. Chen, Z. G. Small-molecule delivery by nanoparticles for anticancer therapy. *Trends Mol. Med*. **2010**, *12*, 594-602.

21. Davis, M. E.; Chen, Z. G.; Shin. D. M. Nanoparticle therapeutics: An emerging treatment modality for cancer. *Nat. Rev. Drug Discov.* **2008***, 7*, 771-782.

22. Wen, C. Y.; Xie, H. Y.; Zhang, Z. L.; Wu, L. L.; Hu, J.; Tang, M.; Wu, M.; Pang. D. W. Fluorescent/magnetic micro/nano-spheres based on quantum dots and/or magnetic nanoparticles: preparation, properties, and their applications in cancer studies**.** *Nanoscale* **2016**, *8*, 12406-12429.

23. Kaewsaneha, C.; Tangboriboonrat, P.; Polpanich, D.; Elaissari. A. Multifunctional fluorescent-magnetic polymeric colloidal particles: Preparations and bioanalytical applications*. ACS Appl. Mater. Interfaces* **2015**, *7*, 23373–23386.

24. Ortgies, D.H.; Cueva, L.; Rosal, B.; Sanz-Rodríguez, F.; Fernández, N.; Cruz, M. C. I.; Salas, G.; Cabrera, D.; Teran, F. J.; Jaque, D.; Rodríguez. E. M. In vivo deep tissue fluorescence and magnetic imaging employing hybrid nanostructures. *ACS Appl. Mater. Interfaces* **2016**, *8*, 1406–1414.

25. Lv, R.; Zhong, C.; Li, R.; Yang, P.; He, F.; Gai, S.; Hou, Z.; Yang, G.; Lin. J. Multifunctional anticancer platform for multimodal imaging and visible light driven photodynamic/photothermal therapy. *Chem. Mater.* **2015**, *27*, 1751–1763.

26. Yang, G.; Yang, D.; Yang, P.; Lv, R.; Li, C.; Zhong, C.; He, F.; Gai, S.; Lin. J. A single 808 nm near-infrared light-mediated multiple imaging and photodynamic therapy based on titania coupled upconversion nanoparticles. *Chem. Mater.* **2015**, *27*, 7957-7968.

27. Lv, R.; Yang, D.; Yang, P.; Xu, J.; He, F.; Gai, S.; Li, C.; Dai, Y.; Yang, G.; Lin, J. Integration of upconversion nanoparticles and ultrathin black phosphorus for efficient photodynamic theranostics under 808 nm near-infrared light irradiation. *Chem. Mater.* **2016**, *28*, 4724-4734.

28. Liu, J.; Chen, Y.; Li, G.; Zhang, P.; Jin, C.; Zeng, L.; Ji, L.; Chao, H. Ruthenium (II) polypyridyl complexes as mitochondria-targeted two-photon photodynamic anticancer agents. *Biomaterials* **2015**, *56*, 140-153.

29. Huang, H.; Yu, B.; Zhang, P.; Huang, J.; Chen, Y.; Gasser, G.; Ji, L.; Chao, H. Highly charged ruthenium (II) polypyridyl complexes as lysosome-localized photosensitizers for two-photon photodynamic therapy. *Angew. Chem. Int. Ed*. **2015**, *16*, 14049-14052.

30. Doherty, R. E.; Sazanovich, I. V.; McKenzie, L. K.; Stasheuski, A. S.; Coyle, R.; Baggaley, E.; Bottomley, S.; Weinstein, J. A.; Bryant, H. E. Photodynamic killing of cancer cells by a platinum (II) complex with cyclometallating ligand. *Sci. Rep*. **2016**, *6:22668*, 1-9.

31. Park, J.; An, K.; Hwang, Y.; Park, J. G.; Noh, H. J.; Kim, J. Y.; Park, J. H.; Hwang, N. M.; Hyeon. T. Ultra-large-scale syntheses of monodisperse nanocrystals. *Nat. Mater*. **2004**, *3*, 891-895.

32. Larsen, E. K.; Nielsen, T.; Wittenborn, T.; Birkedal, H.; Jensen, V. T.; Jakobsen, M. H.; Ostergaard, L.; Horsman, M. R.; Besenbacher, F.; Howard, K. A.; Kjems, J. Size-dependent accumulation of PEGylated silane-coated magnetic iron oxide nanoparticles in murine tumors. *ACS Nano* **2009**, *3*, 1947-1951.

33. Bragg, W. L. The structure of magnetite and the spinels. *Nature* **1915**, *95*, 561.

34. Lee, S. Y.; Harris, M. T. Surface modification of magnetic nanoparticles capped by oleic acids: characterization and colloidal stability in polar solvents. *J. Colloid Interface Sci*. **2006** *293*, 401-408.

CHAPTER 7 – CONCLUSION AND FUTURE PERSPECTIVES

7.1 Conclusion

UCNPs possess several advantages compared to traditional organic fluorophores or other inorganic nanomaterials such as QDs, in particular, due to their ability to absorb low energy NIR radiation and emit high energy UV, visible, or NIR radiation. Moreover, UCNPs also have other positive attributes such as, sharp emission lines due to the shielding of the 4*f* shell, long lifetimes, and excellent photostability. Due to the NIR excitation wavelengths, they also have high penetration depths and virtually no background autofluorescence. Furthermore, UCNPs have been shown to be biocompatible with little to no cytotoxicity, and their surfaces can be easily functionalized making them ideal for biological applications. Unlike QDs, their emission does not result from the nanocrystal host itself but rather from the intentional doping of Ln^{3+} impurities within the crystal structure. Thus, emission color can be tuned by appropriate doping choices and concentration levels. Many of these unprecedented photophysical properties, which are uncommon in other nanoparticles, make UCNPs the desired nanomaterial for various technical and biomedical applications.

In this thesis, we have explored their applications in biosensing and chemical sensing as well as for the generation of ROS for photodynamic therapeutic applications.

The main conclusions could be summarized as follows;

1. A lable-free single stranded DNA nanobiosensor was developed using blue emiting $NaYF_4$:Tm^{3+}, Yb^{3+} UCNPs decorated on monodispersed polystyrene-*co*-acrylic acid nanoparticles as the energy donors and heteroleptic Ir complex decorated gold nanoparticle assembly as the energy acceptors. The energy donor and acceptor were engineered and brought into close proximity using hairpin shaped probe DNA. When the donor nanohybrid was excited at the NIR, the subsequent energy transfer was efficiently quenched by presence of acceptor nanohybrid in close proximity owing to the hairpin shaped structure. However, when the target DNA was introduced, the donor and acceptor moved further and further away, out of range of luminescence resonance energy transfer (LRET), resulting in increasing upconverted emission intensity. Since

the donor UCNPs work in the NIR region, the biosensor offers higher sensitivity for molecular beacon based ssDNA detection up to picomolar concentrations. The selectivity of this DNA nanobiosensor has been proven for single base mismatch.

2. In the next chapter of the thesis, we have synthesized $LiYF_4$ UCNPs co-doped with Tm^{3+} and Yb^{3+} ions showing strong upconverted emission spanning the UV to visible to NIR regions upon 980 nm NIR excitation. This UCNP was surface modified with a biocompatible organic natural product, curcumin. This organic-inorganic nanohybrid has been shown to be a sensitive and selective luminescence quenching material for ratiometric chemical sensing of Cu^{2+} in the visible region. In addition the nanohybrid was also very selective towards Cu^{2+} ions and showed sensitive, detectable changes in the NIR region, which is very beneficial since sensing in the NIR region is less prone to scattering, has higher penetration depths and thus can be effectively used in aqueous media (even in turbid media). This curcumin based UCNP probe offers excellent limit of detection (LOD) for Cu^{2+} up to 4.75 nM.

3. In another chapter of the thesis, we have synthesized a highly photoluminescent Ir complex and functionalized it on the surface of the NIR perturbable $LiYF_4$:Tm^{3+},Yb^{3+} UCNPs. This architecture offered the possibility of indirectly sensitizing the surface functionalized Ir complex through energy transfer of the upconverted radiation following NIR excitation thereby activating the Ir complex and subsequently generating ROS. This newly developed $LiYF_4$:Tm^{3+},Yb^{3+}@SiO_2-Ir nanoplatform paves the way for the NIR triggered generation of ROS, which effectively eliminates the need for low penetrating, high energy external UV excitation, normally required for such photosensitizers.

4. In the final chapter of the thesis, we have synthesized SiO_2 coated Fe_3O_4 SPIONs and functionalized them with a photoluminescent Ir complex. This integrated nanostructure is advantageous due to its magnetic core, which could be used as as MRI contrast agent. In addition, the surface tagged Ir complex is photoluminescent with long lifetime and hence the nanohybrid material could also be used for biolabeling and fluorescence imaging. Most importantly, this Fe_3O_4@SiO_2-Ir SPION generates ROS under UV excitation. The significant aspect of this Ir complex is that, it contains two bio-functionalizable carboxylic acid groups, which could be used to conjugate to any

biomolecule through relatively simple chemistry. The entire nanostructure is less than 50 nm in size hence can be effectively used in other biomedical applications.

7.2 Future Perspectives

NIR perturbable Ln^{3+}-doped UCNPs are excellent functional materials and can be used in many scientific disciplines, especially in the field of biomedical research, and have gained increased attention owing to their unique optical properties. This thesis paves the way for future work in many different directions. In biosensing, in continuation of research work done in this thesis, a new DNA bionanosensor could be developed using different host material and with different emissive dopants. There excellent opportunities for improvement of this biosensor to acheive greater sensitivity and selectivity. Fuerthermore, the quencher (energy acceptor) nanohybrid material could be modified with different transition metal complexes along with the gold nanoparticles or could be completely replaced by other metal plasmonic nanoparticles with ultimate aim of improving sensitivity and selectivity. In chemical sensing, we have used a naturally photoluminescent, biocompatible, organic natural product, curcumin, coupled with Tm^{3+}, Yb^{3+} co-doped $LiYF_4$ UCNPs and the upconverted NIR emission was used for the sensitive detection of Cu^{2+}. Our work in this thesis, offers unprecedented advantage since NIR emission was used for detection leading to improved sensitivity and selectivity. This work can also be extended by using any other naturally photoluminescent organic molecule along with suitable upconversion host crystals and emissive dopants. However, detection in the visible region of the spectrum could reduce the detection limit, hence proper attention must be paid to the choice of a suitable upconversion based donor material. Finally we used a highly photoluminescent Ir complex for the generation of ROS for potential applications in multimodal fluorescence imaging and photodynamic therapy. The use of transtion metal complexes offers many advantages such as large stokes shift, long lifetime, and relative lack of cytotoxicity. We have used an Ir complex in our work since this complex is more biocompatible than many other complexes, which are based on heavy toxic elements for similar applications. This work could be extended by changing the ligands surrounding the Ir metal center resulting in the phototunability of the molecule. Hence, the absorption and

emission properties of these complexes can be engineered depending on the desired application. Finally, the use of the Ir complex with SPIONs also brings about the possibility of many functional properties such as MRI, optical imaging, biolabeling, and ROS generation. In future work, this multimodality could be integrated onto a single suitable UCNP, which could work in the NIR region for enhanced sensitivity.

Overall, this thesis explores the applications of UCNPs (coupled with other fluorescent materials) in many different fields simultaneously. We have especially focused on blue emitting UCNPs with different hosts for applications such as DNA biosensing, chemical sensing and also for the generation of ROS in aqueous media. The choice of the host crystal and emissive dopants are important factors in targeting suitable applications. Henceforth, this work opens new doors to explore new applications in the field of biomedical science with UCNPs at the core.

RÉSUMÉ

Détection Bio/Chimique et Génération de Dérivés Réactifs de l'Oxygène Basées Sur des Nanoparticules à Conversion Ascendante

Joe Gerald Jesu Raj

INRS-EMT, 2017

L'intention de cette thèse est d'explorer de nouvelles applications des nanoparticules hybrides de conversion ascendante (NPCA) excitables dans le proche infrarouge dans les domaines de la détection biologique d'ADN et de la détection chimique du Cu^{2+}. Une attention particulière est portée à l'utilisation de ces NPCA et de nanoparticules d'oxyde de fer superparamagnétiques (NOFSP) avec un complexe d'iridium organométallique pour la génération de dérivés réactifs de l'oxygène (DRO), lesquels sont des intermédiaires réactifs dans des applications de thérapie photodynamique. Pour la détection biologique d'ADN, nous avons premièrement synthétisé des NPCA de $NaYF_4$ co-dopées par les lanthanides Tm^{3+}/Yb^{3+} et émettant dans le bleu. Ces NPCA servent d'émetteurs de lumière lorsqu'elles sont excitées par infrarouge à 980 nm. Elles ont ensuite été ajoutées sur des nanoparticules basées sur un polymère. Ce polymère/matériau nanohybride de conversion ascendante a été fonctionnalisé avec une séquence d'ADN sonde de façon appropriée, par son extrémité amine. Lors d'une synthèse séparée, des nanoparticules d'or (NPAu) monodispersées et un complexe d'iridium (Ir) cyclométallique ont été préparés. La présence de deux groupes fonctionnels carboxyle sur le complexe d'Ir a fourni la conjugaison chimique appropriée pour l'attachement covalent du complexe sur la surface des NPAu via une molécule de liaison ayant un groupe fonctionnel thiol. L'autre extrémité de la séquence d'ADN sonde est une extrémité thiol directement fonctionnalisée sur les NPAu, formant ainsi le matériau nanohybride accepteur. Le donneur nanohybride NPCA/polymère et l'accepteur nanohybride NPAu/Ir ont été mis à proximité via la formation de la structure hélicoïdale de l'ADN sonde. La proximité facilite le transfert d'énergie entre les NPCA dopées au Tm^{3+}/Yb^{3+} et les NPAu fonctionnalisées avec le complexe d'Ir. L'addition subséquente de la séquence d'ADN cible a conduit à l'hybridation de l'ADN et à son

élongation, augmentant ainsi la distance entre les nanohybrides donneur et accepteur. Puisque le transfert d'énergie est dépendant de la distance, un nanocapteur d'ADN à haute sensibilité a été développé. Ce nanocapteur est assez sensible pour détecter des concentration d'ADN cible jusqu'au niveau picomolaire et hautement sélectif, ce qui lui permet de détecter jusqu'à un seul mésappariement de bases. Des nanocapteurs optiques basés sur les dopants de Tm^{3+}/Yb^{3+} de conversion ascendante dans un cristal hôte différent, tel que $LiYF_4$, offre plusieurs avantages. Comparé à une matrice hôte de $NaYF_4$, le $LiYF_4$ offre non seulement une intensité d'émission comparable mais génère également des lignes d'émission additionnelles. Ces caractéristiques optiques du $LiYF_4$ permettent donc la conception de NP de $LiYF_4$ multifonctionnelles combinant deux modes de détection (conversions ascendante et descendante). Les composés contenant du lithium possèdent aussi la capacité de convertir des neutrons incidents en particules ionisantes secondaire. Ainsi, les matériaux dopés au lithium pourraient être bénéfiques dans un détecteur de neutrons à scintillation. Les cristaux de $LiYF_4$ purs sont transparents dans la bande spectrale de 0,12 - 7,5 µm et sont à la fois photorésistants et thermorésistants. Ils ont aussi un faible indice de réfraction non linéaire et de faibles constantes thermo-optiques, ce qui en fait des cristaux applicables en photonique, en optique, en technologie laser et en télécommunications. Les cristaux de $LiYF_4$ sont aussi stables en présence d'air et d'humidité. Considérant tous ces avantages, ces cristaux hôte peuvent être des matériaux hybrides de grande valeur pour plusieurs applications lorsqu'ils sont fonctionnalisés de façon appropriée. Dans ce travail, nous avons intégré un composé organique d'origine naturelle et ayant une importance médicinale, la curcumine, avec des nanoparticules de $LiYF_4$ dopées aux Tm^{3+}/Yb^{3+}. Ce matériau nanohybride organique/inorganique perturbable par proche infrarouge a été utilisé avec succès comme capteur chimique pour la détection d'ions de cuivre. Il a démontré une grande sélectivité, une biocompatibilité ainsi que d'excellentes propriétés de Stern-Volmer. Le transfert résonant d'énergie de luminescence a été effectué entre les NPCA donneuses et la curcumine liée localement comme molécule accepteuse ou reporter. Le transfert d'énergie est une caractéristique clé dans la détection du cuivre. Ceci a été obtenu par la synthèse prudente de nanoparticules tétragonales monodispersées de $LiYF_4$ dopées aux Tm^{3+}/Yb^{3+} et émettant dans l'UV

jusqu'au visible, suivie de leur enrobage par une fine couche de silice les rendant dispersibles dans l'eau. Les NPCA enrobées de silice constituent un matériau donneur adéquat lorsqu'elles sont fonctionnalisées avec la curcumine hautement biocompatible, ce qui mène à la formation d'un nanohybride inorganique/organique qui a prouvé être un excellent matériau pour la détection d'ions de cuivre à haute sensibilité. La limite de détection mesurée pour ce nanohybride est de 4,75 nM, ce qui est largement inférieur à la limite permise dans l'eau potable fixée par l'Agence de protection environnementale des États-Unis (USEPA). Le matériau nanohybride marqué à la curcumine a aussi démontré une sélectivité robuste envers les ions de cuivre, et ce même en la présence d'autre ions métalliques dont des métaux lourds. De plus, nous avons synthétisé des NPCA de $LiYF_4$:Tm^{3+}, Yb^{3+} monodispersées et nous les avons recouvertes d'une coquille de SiO_2 pour les rendre hydrophiles. Les NPCA ont ensuite été fonctionnalisées avec différentes concentrations d'un complexe d'organo-iridium sur leur surface. Les propriétés photophysiques de ces nanostructures de $LiYF_4$:Tm^{3+},Yb^{3+}@SiO_2-Ir ont été investiguées et il a été démontré que, suite à la fonctionnalisation de surface avec le complexe d'iridium, une extinction complète de l'émission UV convertie de façon ascendante provenant des ions Tm^{3+} était observée. Après l'absorption de lumière UV convertie de façon ascendante, le complexe d'Ir a démontré une capacité à générer des DRO, ce qui a été mesuré en présence d'une molécule sonde (DPBF). Des études spectroscopiques de la luminescence de conversion ascendante ont démontré que la photosensibilisation du complexe d'Ir était un processus de nature radiative. Pour confirmer que la génération de DRO était effectivement due à la photosensibilisation du complexe d'Ir des NPCA, deux expériences de contrôle ont été effectuées. Premièrement, les NPCA de $LiYF_4$:Tm^{3+},Yb^{3+}@SiO_2 seules (sans le complexe d'Ir) ont été étudiées pour observer si la lumière UV convertie de façon ascendante elle-même était capable de générer des DRO. Deuxièmement, le complexe d'Ir seul a été étudié après avoir été excité à 980 nm. Dans les deux cas, aucun DRO n'a été observé, indiquant qu'à la fois les NPCA et le complexe d'Ir sont nécessaires pour générer des DRO. Cette plateforme de $LiYF_4$:Tm^{3+},Yb^{3+}@SiO_2-Ir nouvellement développée jette les bases pour la génération de DRO déclenchée par PIR, ce qui élimine efficacement le besoin de l'excitation UV

externe peu pénétrante et à haute énergie normalement requise pour des photosensibilisateurs de ce genre. De plus, nous avons synthétisé et intégré une nanosonde multimodale qui consiste en un complexe d'Ir hautement fluorescent fonctionnalisé sur la surface de nanoparticules magnétiques (Fe_3O_4) recouvertes de silice. Ce système nanohybride rend possible la génération de DRO lors d'une illumination UV directe. La production de DRO est vitale pour des applications concernant l'oncologie de surface. Puisque le complexe d'Ir tel que synthétisé présente une émission visible intense sous excitation UV, le système de nanoparticules magnétiques décorées avec des complexes d'iridium présente plusieurs applications, par exemple en imagerie où la génération de DRO pourrait être utilisée comme nanosonde multimodale.

Objectif de Cette Thèse

L'objectif principal de cette thèse est de synthétiser des nanoparticules de conversion ascendante (NPCA) co-dopées aux Tm^{3+}/Yb^{3+} et émettant dans le UV/bleu, ainsi que de leur trouver de nouvelles applications dans le domaine des nanocapteurs biologiques et chimiques. Étant donné que l'intensité lumineuse émise et la longueur d'onde d'émission des NPCA dépendent de leur environnement cristallin local, différentes structures de cristal hôte (cubique, tétragonale) ont été synthétisées afin d'obtenir différentes symétries cristallines locales autour des dopants de lanthanide optiquement actifs. La caractérisation photophysique et morphologique des NPCA synthétisées a été effectuée à l'aide de différentes méthodes de caractérisation spectroscopique et de surface. Les NPCA synthétisées ont été appliquées avec succès au domaine des capteurs biologiques et chimiques ainsi qu'à la génération de dérivés réactifs de l'oxygène (DRO).

Plus spécifiquement, les objectifs de cette thèse sont résumés ci-dessous;

1. Synthétiser des NPCA cubiques de $NaYF_4:Yb^{3+},Tm^{3+}$ émettant dans le bleu. Les utiliser comme donneurs pour la détection sensible d'ADN simple brin (ADNsb) (biocapteur) basée sur le transfert résonant d'énergie de luminescence (TREL), et ce jusqu'à des concentrations picomolaires.

2. Synthétiser des NPCA tétragonales de $LiYF_4$:Yb^{3+},Tm^{3+} décorées avec un produit naturel hautement photoluminescent, la curcumine, et émettant dans l'ultraviolet (UV) jusqu'au proche infrarouge. Les utiliser pour la détection sensible de Cu^{2+} (capteur chimique) à une longueur d'onde d'excitation proche infrarouge.

3. Synthétiser des NPCA de $LiYF_4$:Yb^{3+},Tm^3 tétragonales décorées avec un complexe d'organo-iridium et émettant dans l'UV jusqu'au proche infrarouge. Les utiliser pour la génération de dérivés réactifs de l'oxygène.

4. Synthétiser des nanoparticules d'oxyde de fer magnétique (Fe_3O_4) décorées avec du Ir (III). Les utiliser pour la génération de dérivés réactifs de l'oxygène.

Détection Sensible d'ADNsb Basée Sur Le Processus TREL Avec Un Matériau Hybride De Conversion Ascendante

Les avancées de la recherche en pharmacogénomique, en découverte de médicaments, en génétique et en maladies infectieuses, ainsi que le développement rapide de la recherche sur l'ADN, alimentent le besoin de trouver des marqueurs fluorescents plus efficaces avec des caractéristiques améliorées. Une large gamme de points quantiques (PQ) fluorescents a été développée et utilisée avec succès lors d'analyses biologiques et de détections optiques basées sur le transfert résonant d'énergie de fluorescence (TREF). Toutefois, l'utilisation de PQ pour la détection de biomolécules est limitée par leur toxicité potentielle et par la présence d'un bruit de fond élevé lors de la présence de biomolécules fluorescentes qui interfèrent. Ce dernier problème est commun à plusieurs autres marqueurs de fluorescence comme les colorants organiques ou les nanoparticules d'or puisqu'ils nécessitent d'être excités dans la région ultraviolette (UV) ou visible du spectre électromagnétique pour obtenir un signal luminescent efficace. Une stratégie utilisée pour minimiser le bruit de fond est de déplacer la longueur d'onde d'excitation dans la région proche infrarouge (PIR). Aux longueurs d'onde PIR, la plupart des molécules organiques et l'eau sont transparents, augmentant ainsi le contraste du signal de luminescence puisque la longueur d'onde d'excitation est spécifique à la sonde optique. Récemment, des nanoparticules (NP) dopées avec des ions de lanthanides (le plus souvent Er^{3+}, Tm^{3+}, Yb^{3+} et Ho^{3+}) ont

attiré l'attention en tant que nanomatériaux fonctionnels pour une grande variété d'applications biologiques grâce à leurs pics d'émission f-f intenses et étroits ainsi qu'à leur longue durée de vie de photoluminescence (PL). En particulier, quand ils sont ajoutés comme dopants à des cristaux hôtes transparents, les dopants peuvent émettre dans l'UV, le visible et même le PIR après une excitation PIR. Cette transformation de la lumière, connue sous le nom de conversion ascendante (CA), est reliée à la présence d'états énergétiques distribués de façon à ce que plusieurs photons PIR puissent être absorbés successivement et émis en une seule étape sous la forme d'un photon à plus haute énergie. Puisque ces états intermédiaires sont des états électroniques réels des ions, le procédé d'excitation peut être effectué en utilisant des diodes laser PIR peu coûteuses et à émission continue. De plus, les ions de lanthanides sont par nature résistants au clignotement, au photoblanchiment et à la dégradation photochimique, ce qui leur donne un avantage supplémentaire par rapport aux colorants organiques et aux points quantiques pour le marquage biologique et les bioessais. L'utilisation de nanoparticules à conversion ascendante (NPCA) dans des capteurs basés sur le transfert résonant d'énergie de luminescence garantit aussi que le donneur et l'accepteur ne sont pas excités à la même longueur d'onde puisque l'excitation des NPCA se produit à une longueur d'onde proche infrarouge de 980 nm, ce qui réduit la possibilité d'autofluorescence et de bruit de fond d'interférence. Cela élimine aussi l'inconvénient de la diaphonie spectrale ou d'autres erreurs possibles durant la mesure. Pour cette raison, plusieurs biocapteurs basés sur le TREL et utilisant des NPCA ont été proposés récemment, utilisant diverses stratégies et quenchers tels que les colorants, les points quantiques de carbone ou les nanoparticules d'or (NPAu). En tant qu'excellents quenchers de luminescence, les NPAu ouvrent de nouvelles perspectives pour la détection de biomolécules à haute sensibilité dans des systèmes TREF grâce à leurs coefficients d'extinction élevés ainsi qu'à leur large spectre d'absorption de lumière visible chevauchant les longueurs d'onde d'émission des donneurs d'énergie communs. Des balises moléculaires ayant une structure en épingle à cheveu et marquées avec des nanoparticules d'or ont aussi été étudiées pour la détection biologique d'ADN basée sur le transfert résonant d'énergie de fluorescence (TREF). Jusqu'à un seul mésappariement de bases de l'ADN a été détecté avec succès

grâce à la formation d'une nanostructure auto-assemblée utilisant des nanoparticules d'or et un fluorophore dans un mécanisme de changement de conformation. Les paires NPCA-NPAu donneur-accepteur attirent de plus en plus d'attention en tant que nanocapteurs biologiques pour la détection rapide et sensible de virus. Jusqu'à récemment, seules des NPAu nues ont été utilisées comme quenchers dans la gamme spectrale verte puisque qu'elles démontrent une grande absorbance reliée à la résonance plasmonique dépendante de la taille du matériau, autour de 520 nm. Pour réaliser une paire donneur-accepteur avec les NPAu, le choix est limité aux ions Er^{3+} en tant qu'émetteurs en raison de leur forte luminescence aux longueurs d'onde vertes. En revanche, la plage de travail possible des NPCA en TREL peut être étendue à différentes couleurs, ce qui fournit la possibilité d'utiliser simultanément plusieurs canaux de détection. Le système proposé dans ce travail utilise des NPCA basées sur un ion activateur de Tm^{3+}, qui est avantageux en raison de son émission de conversion ascendante dans le UV/bleu, une possibilité qui n'a pas été explorée en détail pour la détection TREL jusqu'à maintenant. À cet effet, une NPAu absorbant efficacement la plus grande partie de l'émission du donneur devait être développée afin d'améliorer la sensibilité de la détection. Les complexes d'iridium cyclométalliques ont attiré un intérêt significatif dû à leur forte propriété d'électrochimiluminescence. Un complexe d'Ir (III) soluble dans l'eau avec des ligands de sucres attachés a été rapporté pour la détection d'antibiotiques. Des sondes d'allumage de luminescence d'Ir (III) basées sur le TREF ont aussi été développées pour la détection de cystéine et d'homocystéine. Très récemment, Li et al ont aussi développé un biocapteur d'ADN basé sur l'Ir (III) et ayant été appliqué avec succès à la détection de cellules cancéreuses. Le complexe d'Ir offre plusieurs avantages tels qu'une haute stabilité en solution, une forte photoluminescence et une solubilité dans l'eau, ce qui le rend adapté aux analyses biologiques. Dans ce travail, nous avons développé une biocapteur à haute sensibilité pour la détection d'une séquence ADN cible utilisant des nanohybrides de NPCA de $NaYF_4$:Tm^{3+}, Yb^{3+} sur du PSA/SiO_2 comme donneurs et des complexes d'iridium-bipyridine immobilisés sur des NPAu comme quenchers. De plus, au meilleur de notre connaissance, il n'y a eu aucun compte-rendu précédent de l'utilisation de NPCA comme biocapteur optique en

combinaison avec un complexe cyclométallique d'Ir (III) - NPAu comme quencher pour la détection d'ADN simple brin.

Résultats et Discussion

Le biocapteur de NPCA - TREL proposé est basé sur l'extinction de l'émission visible produite par des NPCA de $NaYF_4$:Tm^{3+}, Yb^{3+} à la suite d'une excitation lumineuse à 980 nm. Le coefficient d'extinction dépend de la distance entre les donneurs (NPCA) et les conjugués de $[(ppy)_2Ir(dcbpy)]^+PF_6^-$-NPAu comme accepteurs d'énergie, comme c'est habituellement le cas pour les processus TREL. Le complexe d'Ir tel que synthétisé démontre une forte absorption dans l'UV avec un maximum d'absorption à 290 nm dû à la transition $\pi \rightarrow \pi^*$, ainsi qu'un épaulement à 380 nm dû à la transition de transfert de charge métal-ligand (TCML). Lorsqu'excité par une lumière UV à 360 nm, le complexe d'Ir émet une lumière intense rouge-orange à 620 nm. Toutefois, quand il est immobilisé à la surface d'une NPAu, le complexe d'Ir cyclométallique montre une absorption à large spectre entre 300 et 800 nm, faisant du conjugué de $[(ppy)_2Ir(dcbpy)]^+PF_6^-$/NPAu un excellent quencher pour la détection optique basée sur le TREL. Un biocapteur TREL basé sur des NPCA offre un avantage supplémentaire: au lieu de directement éteindre le signal sonde, dans ce cas l'émission bleue, la base du processus de conversion ascendante est affectée, ce qui renforce la séparation entre la lumière venant du donneur et les émissions possibles provenant de l'accepteur. La présence d'un grand nombre de liaisons doubles conjuguées dans les cycles aromatiques liés au complexe d'Ir à la surface des nanoparticules promeut le processus de relaxation multiphononique aux niveaux intermédiaires lors du mécanisme de conversion ascendante, ce qui éteint plus efficacement l'émission visible des nanoparticules donneuses. En tant que nanostructures donneuses, des nanoparticules de poly(styrène-co-acide acrylique) (PSA) ont été synthétisées à partir de ses monomères correspondants. Les NPCA hydrophobes coiffées d'oléates ont été rendues hydrophiles à l'aide d'une procédure d'échange de ligands utilisant des ligands de citrate hydrophiles. Ensuite, les NPCA hydrophiles ont été incubées avec des nanostructures de PSA/SiO_2 afin de former le matériau nanohybride PSA/SiO_2/NPCA.

Transfert résonant d'énergie de luminescence et détection d'ADNsb

Les différentes transitions de niveaux énergétiques des NPCA chevauchent celles des nanoparticules d'or liées à l'Ir (III), ce qui fait de ces dernières un excellent matériau quencher pour la technique TREL. L'extinction de l'émission visible des $NaYF_4$:Tm^{3+}, Yb^{3+} par les conjugués Ir(III)-NPAu est possible grâce à deux processus différents, l'un radiatif et l'autre non radiatif. Lors du transfert d'énergie radiatif (réabsorption), les photons émis par les NPCA à chaque longueur d'onde sont absorbés par le quencher. Ce processus prend donc place à chaque longueur d'onde à laquelle les NPCA émettent (Figure 1B) et à laquelle les nanoparticules d'Au décorées d'Ir (III) absorbent (Figure 1A). D'autre part, le transfert d'énergie non radiatif est une interaction d'échange qui a lieu plus rapidement que l'émission de photons par les NPCA. En conséquent, il a lieu quand les transitions des NPCA (donneurs) et des quenchers (accepteurs) sont caractérisées par la même énergie.

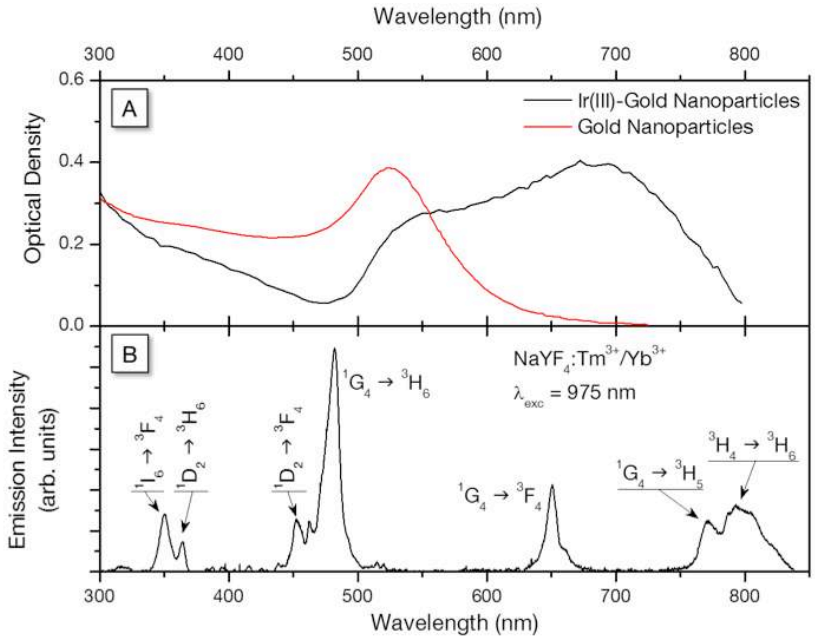

Figure 1. (A) Spectre d'absorption UV-Vis des NPAu (ligne rouge) et des complexes d'Ir $[(ppy)_2Ir(dcbpy)(4\text{-}ABT)_2]$ immobilisés sur les NPAu (ligne noire) (B) Spectre d'émission de conversion ascendante du $NaYF_4$:Tm^{3+}, Yb^{3+} dans l'hexane avec les transitions de niveaux énergétiques correspondantes, à la suite d'une excitation à 975 nm.

Il est évident que l'élargissement du spectre d'absorption du quencher résulte de la fonctionnalisation de surface des nanoparticules d'or par le complexe d'Ir. Cet élargissement est une caractéristique favorable de deux façons. Premièrement, du point

de vue du transfert d'énergie radiatif, plus d'émissions sont affectées par le quencher. Deuxièmement, du point du vue du transfert d'énergie non radiatif, l'absorption des NPAu décorées d'Ir est maintenant résonante à la fois avec les transitions $^3F_{2,3} \rightarrow {}^3H_6$ et $^1G_4 \rightarrow {}^3F_4$ des ions Tm^{3+}. Par conséquent, les accepteurs vont interrompre la voie de conversion ascendante usuelle, éteignant ainsi les émissions visibles reliées aux plus hauts niveaux excités. Lorsque la séquence d'ADN complémentaire est ajoutée au complexe, les deux assemblages de nanoparticules sont éloignés à cause de la formation de la structure hybride en double hélice allongée. La probabilité de transfert d'énergie de luminescence entre les deux assemblages est alors réduite, ce qui restaure l'intensité d'émission (allumage) des NPCA donneuses. Pour calibrer la sensibilité du complexe préparé, l'émission de luminescence a été mesurée pour plusieurs échantillons contenant la même concentration de complexes d'ADN sondes et ayant été titrés par différentes concentrations d'ADN cible jusqu'à un minimum de 1 pM. L'addition d'un contrôle négatif à la balise moléculaire sonde connectée aux nanohybrides, PSA/SiO_2NP/ $NaYF_4$:Tm^{3+},Yb^{3+}//$ADN_{sb(\text{Sonde})}$// Ir(III)-NPAu, ne montre pratiquement aucun changement dans l'intensité d'émission de conversion ascendante, ce qui confirme la sensibilité de notre méthode (Figure 2D). Pour confirmer la sélectivité de notre nanocapteur, nous avons titré la sonde d'ADN par une séquence d'ADN cible contenant un seul mésappariement de bases. La mesure de l'émission de conversion ascendante prouve que l'émission dans le bleu reste presque éteinte (Figure 2D) lors de l'excitation à 980 nm, confirmant la nature hautement sélective du nanocapteur biologique proposé. L'intensité d'émission (Figure 2A) est proportionnelle à la concentration de la séquence d'ADN sonde dans l'échantillon à cause de la structure d'ADN hybride en double hélice allongée qui augmente la distance entre les [$(ppy)_2$Ir(dcbpy)$(4\text{-ABT})_2$]/NPAu et les nanohybrides de NPCA décorées par PSA/SiO_2. À partir de la Figure 2D, il est clair que le nanocapteur proposé est assez sélectif pour détecter un seul mésappariement de bases. À des fins de calibration, l'aire sous les bandes d'émission (Figure 2A) a été tracée en fonction de la concentration d'ADN cible (Figure 2B). À partir de la figure 2B, il est évident que ces deux grandeurs sont reliées par une dépendance linéaire dans un graphique semi-logarithmique, ce qui donne la courbe de sensibilité pour le nanocapteur biologique d'ADNsb. Le fait que la

dépendance entre les grandeurs ne soit pas linéaire peut être attribué à la nature non linéaire du processus de conversion ascendante. En particulier, pour les nanoparticules de Tm^{3+}, Yb^{3+} dopées et excitées à 980 nm, le mécanisme de conversion ascendante nécessaire pour émettre de la lumière bleue est au minimum un processus du troisième ordre. Dans la stratégie d'extinction proposée, la luminescence est bloquée à partir du niveau émettant dans le PIR et agissant comme étape intermédiaire pour la conversion ascendante, au lieu de directement éteindre l'émission bleue. Ceci indique que la sensibilité du biocapteur, i.e. la différence d'intensité entre deux concentrations différentes ($\Delta I/\Delta[ADN]$), est plus élevée pour des concentrations plus faibles.

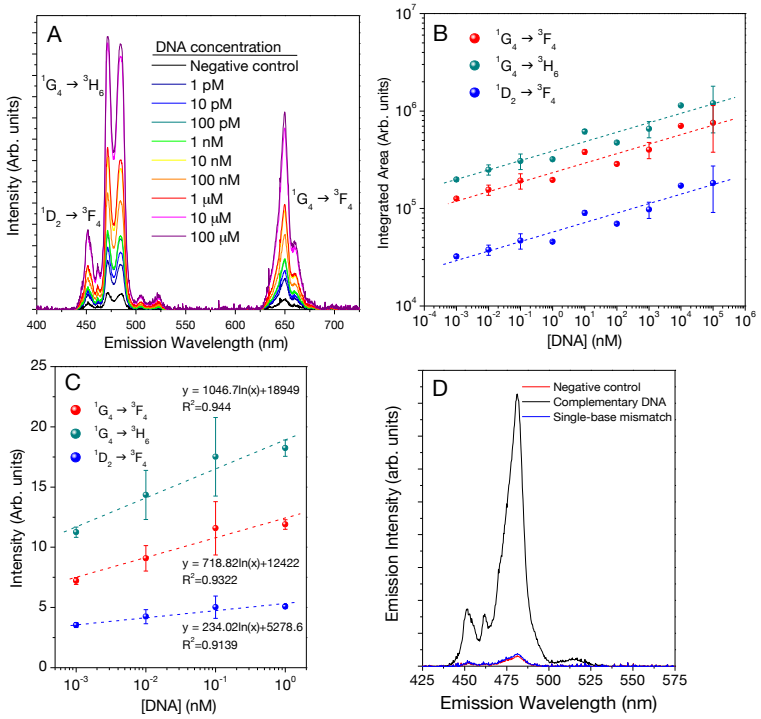

Figure 2. (A) Aire intégrée sous la courbe d'émission bleue vs concentration de la séquence d'ADN complémentaire (B) Spectre de conversion ascendante du capteur dans la région bleue, lors de l'addition de différentes concentration de la séquence d'ADNsb cible (C) Dépendance linéaire de l'intensité d'émission pour les concentrations d'ADN cible les plus faibles (D) Comparaison des intensités d'émission de luminescence pour les séquences d'ADN complémentaire, d'ADN de contrôle négatif et d'ADN avec un seul mésappariement de bases.

Ainsi, dans l'intervalle où le signal est normalement le plus faible, la différence d'intensité de luminescence est considérablement élevée, et ce même pour de petits changements de concentration d'ADN cible. Les mesures optiques initiales ont montré

un comportement non linéaire pour les plus grandes concentrations d'ADN. Ceci peut être attribué à la précipitation des nanohybrides lors de l'hybridation avec l'ADN cible. Aux plus grandes concentrations, l'hybridation de l'ADN mène à l'agrégation, ce qui conduit à la précipitation. C'est ce qui affecte la dépendance linéaire des mesures optiques. Toutefois, pour les concentration plus faibles allant de 1 nM à 1 pM, l'intensité d'émission démontre une dépendance linéaire située bien à l'intérieur des barres d'erreur (Figure 2C). Ceci confirme la sensibilité accrue et la reproductibilité de notre biocapteur, particulièrement aux concentrations d'ADN les plus faibles testées, soit jusqu'à 1 pM.

Conclusion

En conclusion, nous avons développé un nouveau détecteur d'ADN basé sur le TREL. Ce détecteur utilise des nanohybrides de PSA/SiO_2/NPCA fonctionnalisés comme donneurs d'énergie et des conjugués de [$(ppy)_2$Ir(dcbpy)(4-ABT)$_2$]-NPAu solubles dans l'eau comme quenchers efficaces. L'efficacité du détecteur a été démontrée jusqu'au niveau picomolaire. L'efficacité des NPCA de Tm^{3+}, Yb^{3+} co-dopées en tant que donneurs a été démontrée et ouvre la porte à la possibilité de réaliser des détecteurs multicanaux en combinaison avec d'autres lanthanides, par exemple les ions Er^{3+} qui sont les plus couramment utilisés. L'utilisation de nanoparticules de PSA qui peuvent être facilement fonctionnalisées avec différentes particules donneuses est aussi un avantage à cet égard. Nos résultats ont également fourni un système TREL sensible et simple à utiliser pour des analyses biologiques. Des études futures pourraient ouvrir la voie à une extension des applications de ce nouveau procédé de détection pour la détection multiplexée ultrasensible d'une vaste gamme d'analytes biomoléculaires.

***Les résultats ont été publiés dans ACS Applied Materials and Interfaces*:**
Joe Gerald Jesu Raj, Marta Quintanilla, Khaled A. Mahmoud, Andy Ng, Fiorenzo Vetrone and Mohammed Zourob, "Sensitive detection of *ss*DNA using an LRET based upconverting nanohybrid material", *ACS Appl. Mater. Interfaces*, 2015, 7, 18257−18265.

Direct Détection de Cu^{2+} Ions à Une Longueur d'onde Proche Infrarouge (PIR) et Visible Utilisant Un Matériau Nanohybride de Conversion Ascendante de $LiYF_4$:Tm^{3+}, Yb^{3+} Marqué à la Curcumine

Introduction

Les ions métalliques lourds sont considérés comme des polluants environnementaux et, à cause de leur nature toxique, les récepteurs capables de détecter un ion métallique lourd en particulier dans un mélange complexe sont d'un intérêt significatif. Ces récepteurs ont aussi des applications potentielles dans des systèmes biologiques et reliés à la santé. Parmi tous les ions métalliques lourds, l'ion Cu^{2+} est un cas particulier puisqu'il joue un rôle crucial dans le corps humain ainsi que dans d'autres organismes vivants. Toutefois, même si le cuivre joue un rôle important pour la santé humaine, sa présence à haute concentration peut causer des problèmes de santé sérieux tels que les maladies d'Alzheimer et de Parkinson. De plus, le cuivre est un des éléments lourds les plus communs qu'on peut trouver dans l'eau courante de plusieurs pays en voie de développement ou développés. Par conséquent, la détection d'ions de Cu^{2+} en la présence d'autres ions métalliques et d'impuretés présente une importance significative. Dans ce travail, un nanocapteur réutilisable de Cu^{2+} a été réalisé en utilisant des NPCA de $LiYF_4$:Tm^{3+}, Yb^{3+} comme donneurs d'énergie et un produit naturel organique plus biocompatible, la curcumine, comme molécule accepteuse d'énergie dans un procédé connu sous le nom de transfert résonant d'énergie de luminescence (TREL). L'utilisation de la curcumine sous forme de poudre de curcuma dérivée de la plante *curcuma longa* comme accepteur d'énergie offre des avantages sans précédent tels qu'une biocompatibilité accrue, aucune toxicité, une propriété de fluorescence excellente et une multifonctionnalité permettant entre autres son utilisation en thérapie photodynamique. La curcumine est aussi connue pour avoir des propriétés anti-inflammatoires et anti-cancer potentielles. Ce nanocapteur élimine complètement l'utilité de tout fluorophore organique toxique et plus coûteux. De plus, la plupart des fluorophores organiques disponibles commercialement souffrent d'un haut taux de blanchiment, de la nécessité d'une excitation UV directe qui augmente la diffusion et réduit la profondeur de pénétration dans un milieu biologique, de leur propension à

subir une réaction de photolyse menant à la désintégration des molécules et de leur possible réaction avec d'autres impuretés.

Dans le système nanohybride proposé, la détection ratiométrique du cuivre prend place à deux longueurs d'onde différentes. Premièrement, les longueurs d'onde visibles de 450 et 510 nm émises par les NPCA ont pu être modifiées grâce au marquage de la surface des NPCA par des molécules de curcumine. La présence de la curcumine sur la surface des NPCA absorbe fortement la lumière UV à 350 nm et bleue à 450 nm mais émet à 510 nm. Deuxièmement, la détection d'ions de cuivre prend place directement à la longueur d'onde proche infrarouge de 790 nm puisque les ions de cuivre absorbent fortement à cette longueur d'onde. La formation d'un complexe de coordination entre la curcumine à la surface d'une NPCA et le cuivre fournit une opportunité sans précédent de détecter ce dernier. Le complexe fournit une plateforme pour le transfert d'énergie proche infrarouge de la NPCA aux complexes d'ions de cuivre et de curcumine, en éteignant ainsi la longueur d'onde de 790 nm.

Résultats et discussion

Détection de Cu^{2+} à une longueur d'onde proche infrarouge (PIR)

L'intensité d'émission proche infrarouge des NPCA est graduellement éteinte lorsque la concentration de Cu^{2+} est augmentée. Le processus d'extinction suit l'équation de Stern-Volmer. Le graphique de Stern-Volmer présente un excellent coefficient de corrélation linéaire de 0,9957 et la constante d'extinction de Stern-Volmer est de 6,52 x 10^7. Ces résultats mettent en évidence un seul mécanisme d'extinction statique lorsque des NPCA marquées à la curcumine sont mélangées avec des Cu^{2+} de charges opposées puisqu'ils se coordonnent ensemble. La constante d'association (K_b) et la stœchiométrie du complexe (n) sont respectivement de 3.69 x 10^7 M^{-1} et 1.2 selon les calculs. La valeur élevée de la constante d'association confirme que l'interaction est forte entre la curcumine et le quencher, soit le Cu^{2+} à la surface de NPCA, ce qui augmente l'efficacité globale du transfert d'énergie de luminescence résonant. La stœchiométrie du complexe (n) est d'environ 1,2, ce qui nous informe sur la formation du complexe de coordination entre la curcumine et le Cu^{2+}.

Le matériau nanohybride $LiYF_4$:Tm^{3+}, Yb^{3+}@SiO_2-curcumine est très sélectif envers les ions de Cu^{2+} comparé à d'autres ions métalliques incluant des ions métalliques lourds tels que Sn^{4+}, Pb^{2+}, Hg^{2+} et Cd^{2+}. La nature robuste de ce matériau nanohybride a été confirmée en effectuant des mesures de luminescence de conversion ascendante en la présence d'autres ions métalliques. Dans les expériences compétitives effectuées, des ions de Cu^{2+} (10 nM) et d'autres ions métalliques en excès de 10 fois ont été simultanément ajoutés au $LiYF_4$:Tm^{3+}, Yb^{3+}@SiO_2-curcumine. Les résultats montrent que la réponse en intensité de luminescence de conversion ascendante des ions de $LiYF_4$:Tm^{3+}, Yb^{3+}@SiO_2-curcumine n'est pas affectée par la présence d'autre ions métalliques. Ainsi, il a été prouvé que le matériau nanohybride $LiYF_4$:Tm^{3+}, Yb^{3+}@SiO_2-curcumine est un excellent nanocapteur chimique optique pour la détection sélective d'ions Cu^{2+}, et ce même dans un milieu complexe.

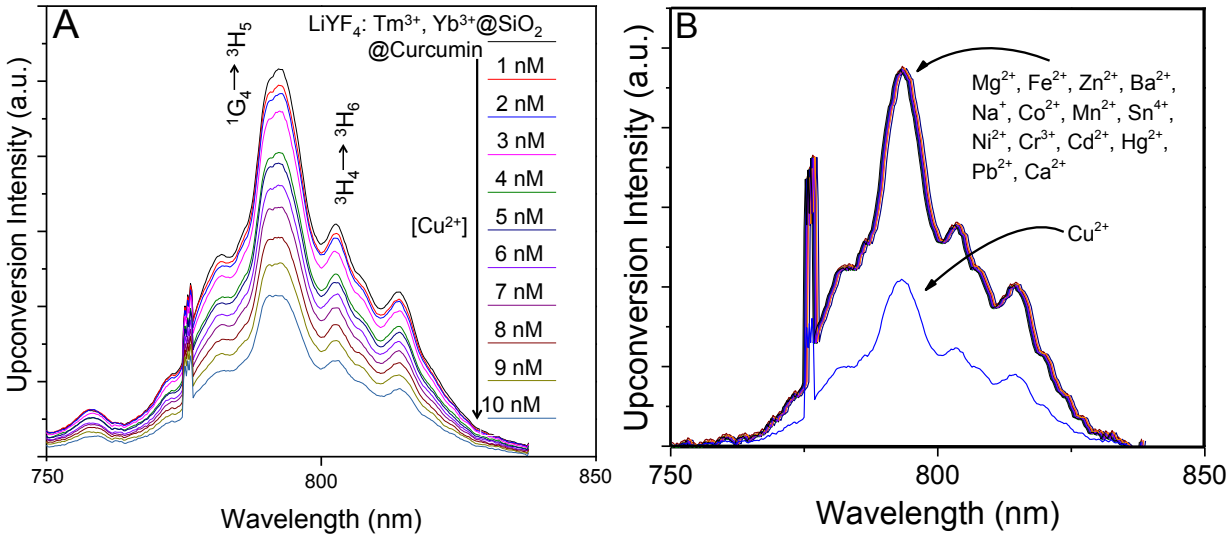

Figure 3. (A) Réduction de l'intensité d'émission des NPCA chargées de curcumine à la longueur d'onde PIR, pour différentes concentrations de Cu^{2+}. (B) Sélectivité envers les ions Cu^{2+} due à la formation de complexes [Cu^{2+} ← curcumine], en présence d'autres ions métalliques, dans la région PIR.

Réutilisabilité du nanocapteur de $LiYF_4$:Tm^{3+}, Yb^{3+}@SiO_2-curcumine

Pour des applications pratiques de la vie réelle, il est impératif de confirmer la réutilisabilité du matériau nanohybride synthétisé. Quand l'acide éthylène diamine tétraacétique (EDTA) a été titré par une solution contenant le nanomatériau hybride $LiYF_4$:Tm^{3+}, Yb^{3+}@SiO_2-curcumine coordonné au Cu^{2+}, la couleur de la solution a

changé d'incolore (cuivre coordonné à la curcumine) à jaune. Ceci confirme que presque tous les ions de Cu^{2+} qui étaient coordonnés à la curcumine avant le titrage sont coordonnés au EDTA après le titrage. De plus, 85% de l'absorbance originale du matériau nanohybride $LiYF_4$:Tm^{3+}, Yb^{3+}@SiO_2-curcumine a été restaurée. Ces résultats confirment que le complexe de coordination de la curcumine à la surface des NPCA recouvertes de silice est réversible et que, puisque l'EDTA (hexadenté) est un meilleur ligand que la curcumine (bidentée), les ions de Cu^{2+} se coordonnent préférentiellement avec l'EDTA. Ceci assure la réutilisabilité des NPCA chargées de curcumine pour des applications de détection d'ions Cu^{2+} de routine et pour des applications plus rigoureuses.

Conclusion

En conclusion, il a été démontré que des NPCA excitables dans le PIR, émettant dans l'UV jusqu'au PIR et marquées avec un produit naturel organique et biocompatible, la curcumine, constituent un matériau hybride quencher sensible et sélectif pour la détection ratiométrique du Cu^{2+}. Ce matériau nanohybride est très sélectif envers les ions de Cu^{2+} et provoque une réponse optique de type allumé-éteint dans la région visible du spectre de luminescence de conversion ascendante via un transfert résonant d'énergie de luminescence. En plus des changements dans les longueurs d'onde visibles, les nanohybrides ont aussi montré des changements dans la région PIR, ce qui est très avantageux puisque les longueurs d'onde proche infrarouge diffusent moins et possèdent de plus grandes profondeurs de pénétration, rendant ainsi possible leur utilisation efficace en milieu biologique. Cette nanosonde à conversion ascendante basée sur la curcumine rend la détection possible à l'œil nu via un changement de couleur puisque l'ion métallique peut être détecté par colorimétrie. La limite de détection du Cu^{2+} trouvée est beaucoup plus faible que la concentration de Cu^{2+} permise selon les recommandations de l'OMS, de l'USEPA et de Santé Canada. La présence de curcumine sur la surface de silice des nanoparticules ajoute une biocompatibilité supplémentaire et réduit la toxicité puisque la curcumine a été classée "généralement reconnue comme sûre" (*generally recognized as safe*, GRAS) par la USFDA.

Les résultats sont en voie de publication dans ACS Sensors

Génération de Dérivés Réactifs de l'Oxygène Déclenchée Par Illumination Proche Infrarouge de Nanoparticules de Conversion Ascendante Décorées Avec Un Complexe d'Organo-Iridium

Introduction

Au cours des dernières années, les complexes basés sur les métaux de transition ont suscité beaucoup d'attention pour une grande variété d'applications. En particulier, les complexes d'iridium (Ir) cyclométalliques présentent un intérêt significatif à cause de leurs propriétés accordables, qui peuvent être modifiées en changeant les ligands et leurs substituants autour du centre métallique. Les propriétés de luminescence de ces complexes luminescents ont longtemps été étudiées puisqu'ils sont bien connus pour leurs grands déplacements de Stokes, leurs longues durées de vie, leurs longueurs d'onde d'absorption et d'émission accordables ainsi que leurs rendements quantiques élevés, des caractéristiques qui sont attribuables à leurs transitions de transfert de charge métal-ligand (TCML). Ces propriétés photophysiques remarquables rendent les complexes d'Ir accessibles pour une large gamme d'applications optoélectroniques, incluant l'imagerie biomédicale et en particulier son utilisation en cancérologie. L'influence des complexes d'Ir dans le domaine de la recherche sur le cancer n'est pas limitée aux applications en imagerie biologique. Ces complexes ont été étudiés pour des utilisations en thérapies anticancéreuses, particulièrement en chimiothérapie et en thérapie photodynamique (TPD). Un des principaux inconvénients de l'utilisation de ces complexes de métaux de transitions pour des applications en TPD, comme pour d'autres photosensibilisateurs utilisés en clinique, est la nécessité d'exciter le photosensibilisateur avec une grande énergie lumineuse UV ou avec de la lumière visible. Une faible pénétration du tissu ou une haute énergie lumineuse freine l'utilisation des complexes dans des systèmes vivants où des cancers sont cachés profondément dans le corps. Pour des applications efficaces en TPD, il est important d'utiliser des systèmes qui peuvent être activés dans la région PIR puisqu'à cette longueur d'onde, la génération de dérivés réactifs de l'oxygène peut être effectuée à de plus grandes profondeurs de pénétration et en évitant la fluorescence de fond.

Dans le cadre de ce travail, nous avons synthétisé des NPCA de $LiYF_4$:Tm^{3+},Yb^{3+}@SiO_2 décorées avec un complexe d'organo-iridium hydrophile afin d'étudier la génération de DRO suivant une excitation PIR à 980 nm. C'est à notre connaissance le premier compte-rendu de l'utilisation d'un complexe d'organo-iridium pour la génération de DRO déclenchée par PIR. De plus, le complexe d'organo-iridium hydrophile possède deux groupes fonctionnels carboxyle (-COOH) qui sont facilement disponibles pour une future bioconjugaison de diverses molécules. Ainsi, la nanostructure $LiYF_4$:Tm^{3+},Yb^{3+}@SiO_2-Ir peut servir d'échafaudage à partir duquel des propriétés additionnelles pourraient être ajoutées au complexe dans le futur.

Résultats et Discussion

L'objectif principal du système nanostructuré NPCA@SiO_2-Ir conçu dans le cadre de ce travail était de sensibiliser le complexe d'Ir via un rayonnement UV convertie de façon ascendante puisque le complexe possède une forte absorption dans la région UV (voir ci-dessous). Par conséquent, des NPCA à émission UV intense convertie de façon ascendante étaient requises. Parmi un certain nombre de NPCA satisfaisant à ce critère, la NPCA de $LiYF_4$:Tm^{3+},Yb^{3+} a été choisie puisque son émission UV intense convertie de façon ascendante démontre une capacité à sensibiliser d'autres processus activés par la lumière.

Génération de dérivés réactifs de l'oxygène (DRO) par excitation PIR

Pour étudier ceci, les nanostructures de $LiYF_4$:Tm^{3+},Yb^{3+}@SiO_2-Ir ont été dispersées dans une solution contenant la molécule sonde, 1,3-diphenylisobenzofurane (DPBF). En utilisant cette méthode, la génération de DRO déclenchée par PIR chez les nanostructures de $LiYF_4$:Tm^{3+},Yb^{3+}@SiO_2-Ir peut être indirectement suivie via la diminution du spectre d'absorption de la molécule sonde DPBF, qui montre une forte absorption à 420 nm. Le DPBF est hautement réactif en présence de $^1O_2$ et le décompose, ce qui a pour résultat de diminuer l'absorption à 420 nm en la présence de $^1O_2$. La diminution de l'intensité d'absorption est directement proportionnelle à la quantité de $^1O_2$ produite dans l'échantillon. Afin de mesurer la libération de DRO, les nanostructures de NPCA@SiO_2-Ir ont été dispersées dans une solution aqueuse qui contient la molécule sonde DPBF ayant été irradiée par un laser PIR à 980 nm durant différents intervalles de temps. Les spectres d'absorption ont été enregistrés après chaque dix minutes d'irradiation.

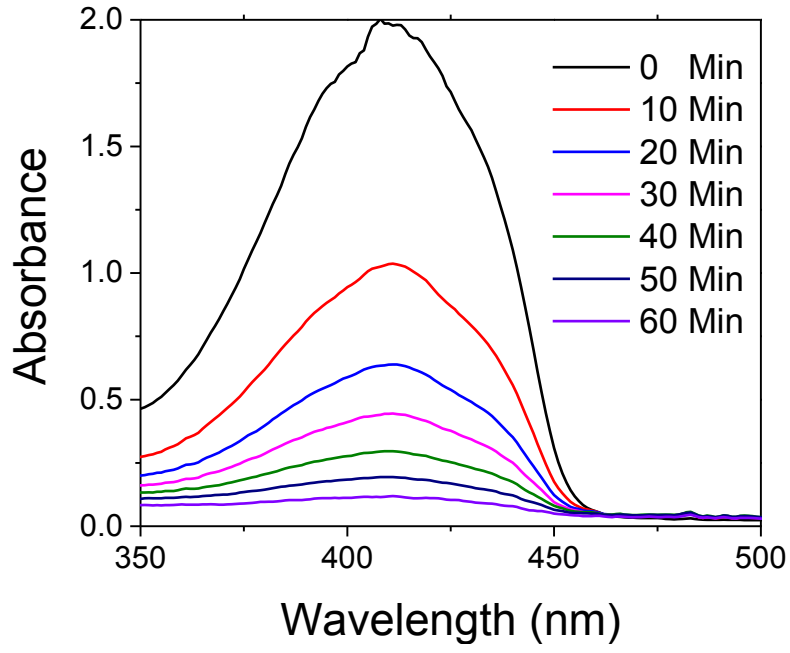

Figure 4. Diminution du spectre d'absorption du DPBF en présence de la nanostructure de NPCA@SiO_2@Ir, après différents intervalles de temps.

Conclusions

En résumé, nous avons synthétisé des NPCA monodispersées de $LiYF_4$:Tm^{3+},Yb^{3+} (65 nm de largeur et 110 nm de longueur) et nous les avons recouvertes d'une coquille de 13 nm de SiO_2 afin de les rendre hydrophiles. Les NPCA ont ensuite été fonctionnalisées avec différentes concentrations d'un complexe d'organo-iridium sur leur surface. Les propriétés photophysiques de ces nanostructures de $LiYF_4$:Tm^{3+},Yb^{3+}@SiO_2-Ir ont été investiguées et il a été démontré que, suite à la fonctionnalisation de surface avec le complexe d'iridium, une extinction complète de l'émission UV convertie de façon ascendante provenant des ions Tm^{3+} était observée. Après l'absorption de lumière UV convertie de façon ascendante, le complexe d'Ir a démontré une capacité à générer des DRO, ce qui a été mesuré en présence d'une molécule sonde (DPBF). Des études spectroscopiques de la luminescence de conversion ascendante ont démontré que la photosensibilisation du complexe d'Ir était un processus de nature radiative. Pour confirmer que la génération de DRO était effectivement due à la photosensibilisation du complexe d'Ir des NPCA, deux expériences de contrôle ont été effectuées. Premièrement, les NPCA de $LiYF_4$:Tm^{3+},Yb^{3+}@SiO_2 seules (sans le complexe d'Ir) ont été étudiées pour observer si la lumière UV convertie de façon ascendante elle-même était capable de générer des DRO. Deuxièmement, le complexe d'Ir seul a été étudié après avoir été excité à 980 nm. Dans les deux cas, aucun DRO n'a été observé, indiquant qu'à la fois les NPCA et le complexe d'Ir sont nécessaires pour générer des DRO. Cette plateforme de $LiYF_4$:Tm^{3+},Yb^{3+}@SiO_2-Ir nouvellement développée jette les bases pour la génération de DRO déclenchée par PIR, ce qui élimine efficacement le besoin de l'excitation UV externe peu pénétrante et à haute énergie normalement requise pour des photosensibilisateurs de ce genre.

***Les résultats ont été publiés dans Journal of Materials Chemistry B*:**

Joe Gerald Jesu Raj, Marta Quintanilla and Fiorenzo Vetrone, "Near-Infrared Triggered Generation of Reactive Oxygen Species from Upconverting Nanoparticles Decorated with an Organoiridium Complex " *J. Mater. Chem. B*, 2016, 4, 3113 - 3120.

Nanoparticules Magnétiques Marquées Avec Des Complexes d'Iridium Hétéroleptiques Cyclométalliques Pour la Génération d'Espèces Réactives de l'Oxygène

Introduction

Les nanoparticules d'oxyde de fer superparamagnétiques ont récemment attiré beaucoup d'attention grâce à plusieurs applications biomédicales. Cela est attribuable à leur synthèse facile, à leur biocompatibilité, à leurs conditions de réaction douces, à leur chimie de fonctionnalisation de surface simple et à leurs propriétés magnétiques. Les propriétés magnétiques des nanoparticules d'oxyde de fer pourraient être contrôlées par l'application d'un champ magnétique externe. Ceci ouvre la voie à la livraison de médicaments ciblée vers des cellules cancéreuses par un cœur magnétique encapsulé dans une couche de médicament, et ce en changeant le champ magnétique appliqué. Ces nanoparticules d'oxyde de fer superparamagnétiques trouvent aussi des applications dans le domaine de l'imagerie par résonance magnétique (IRM) comme agent de contraste, en microbiologie pour la séparation magnétique et en détection biochimique. Toutefois, l'inconvénient principal des nanoparticules magnétiques est leur agglomération après synthèse. Les revêtements de surface et la fonctionnalisation pourraient résoudre ce problème de façon efficace. Les surfaces de silice sont chimiquement stables, biocompatibles et peuvent aisément être fonctionnalisées à des fins de bioconjugaison. Un nanosystème hybride offre des combinaisons de propriétés telles que la séparation magnétique et la détection optique d'un analyte cible. Dans les dernières années, la thérapie photodynamique a attiré beaucoup d'attention en essais cliniques. Le principe de la thérapie photodynamique dépend de l'utilisation d'une molécule photoperturbable appelée sensibilisateur. En présence d'oxygène moléculaire, le sensibilisateur peut être activé par la une lumière de longueur d'onde appropriée afin de produire des dérivés réactifs de l'oxygène (DRO) tels que des radicaux libres et de l'oxygène singulet. Récemment, les complexes de métaux de transition ont attiré beaucoup d'attention due au développement de la nanothérapie multimodale. Toutefois, la plupart des sensibilisateurs basés sur un métal de transition ayant déjà été décrits sont des complexes de ruthénium. Curieusement, les complexes d'Ir n'ont pas été

explorés autant que les complexes d'autres métaux. D'Ir a une propriété intéressante qui le rend unique par rapport aux autres complexes, soit l'effet d'atome lourd. L'intégration d'un tel complexe photoluminescent avec des nanoparticules magnétiques offre la multimodalité. L'utilisation de nanoparticules d'oxyde de fer magnétiques avec d'autres fluorophores organiques ou avec des points quantiques inorganiques pourrait avoir des effets contraires au but recherché puisque les fluorophores organiques sont connus pour posséder des effets cytotoxiques et de photoblanchiment et que les points quantiques basés sur un métal lourd sont considérés comme hautement cytotoxiques malgré leurs rendements quantiques plus élevés. Ainsi, afin de surmonter ces effets néfastes, il est possible d'utiliser un complexe constitué d'un métal de transition et possédant la propriété d'être optiquement accordable.

Génération de dérivés réactifs de l'oxygène (DRO) par excitation UV

L'effet de photosensibilisation du complexe d'Ir prend place sous illumination UV directe, ce qui conduit à la production de dérivés réactifs de l'oxygène. Pour évaluer l'effet du complexe d'Ir, le matériau hybride Fe_3O_4@SiO_2-Ir a été dispersé dans une solution contenant la molécule sonde DPBF. L'excitation directe de la nanostructure par un rayonnement UV à 360 nm conduit à une réduction de l'absorption du DPBF (montré ci-dessous) puisqu'il réagit avec le DRO ($^1O_2$*). La diminution de l'intensité d'absorption est directement proportionnelle à la quantité d'oxygène singulet produite dans l'échantillon.

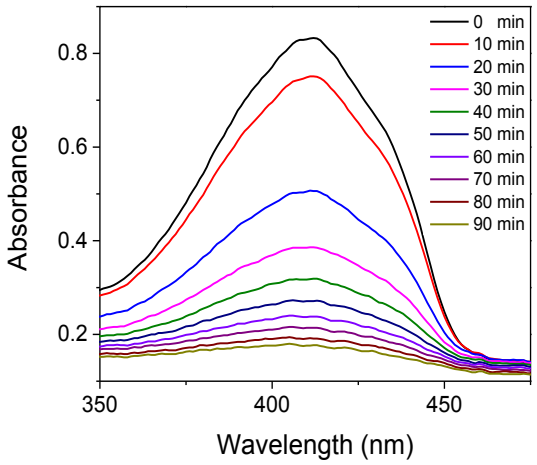

Figure 5. Diminution du spectre d'absorption du DPBF en la présence de nanostructures de Fe_3O_4@SiO_2-Ir pour différents intervalles de temps.

Conclusion

En résumé, nous avons synthétisé des nanoparticules magnétiques (Fe_3O_4) monodispersées à petit noyau (21 nm) et nous les avons recouvertes de SiO_2 pour les rendre dispersibles dans l'eau ou dans une solution tampon ainsi que pour y augmenter le nombre de complexes d'Ir. Différentes concentrations d'un complexe d'organo-iridium hétéroleptique cyclométallique ont ensuite été ajoutées à la surface des NP de Fe_3O_4@SiO_2. Les propriétés photophysiques de ces nanostructures de Fe_3O_4@SiO_2-Ir ont été évaluées. Pour confirmer que la génération de DRO est due au complexe d'Ir, une expérience de contrôle a été effectuée sans le complexe d'Ir à la surface des Fe_3O_4@SiO_2. Premièrement, les NP de Fe_3O_4@SiO_2 seules ont été étudiées en la présence de DPBF. La sonde n'a montré aucun changement d'absorption à 420 nm lors de l'excitation UV, et ce après différents intervalles de temps. L'absence de tout changement dans l'absorption de la sonde confirme qu'aucun DRO n'a été produit par le Fe_3O_4@SiO_2. Toutefois, quand la même expérience a été effectuée sur une nanostructure de Fe_3O_4@SiO_2-Ir, l'intensité d'absorption du DPBF a été significativement réduite, ce qui confirme le rôle du complexe d'Ir dans la production de DRO par la nanostructure. Ceci a été évalué pour des concentrations d'Ir à la surface de la silice faibles à élevées. La nanostructure avec la plus grande concentration d'Ir testée a montré une génération de DRO plus grande qu'avec une plus faible concentration d'Ir, et ce après le même temps. Ceci confirme que la présence d'une plus grande quantité du complexe d'Ir est nécessaire pour atteindre une meilleure efficacité de génération de DRO. Cette nouvelle nanoplateforme de Fe_3O_4@SiO_2-Ir ouvre la voie à l'imagerie biologique ainsi qu'à la thérapie photodynamique grâce à la présence du complexe d'Ir hautement luminescent et à son efficacité de production de DRO dans un seul matériau nanocomposite.

Les résultats sont en voie de publication.

PUBLICATIONS

1. **Joe Gerald Jesu Raj**, Marta Quintanilla, Khaled A. Mahmoud, Andy Ng, Fiorenzo Vetrone and Mohammed Zourob, Sensitive detection of *ss*DNA using an LRET based upconverting nanohybrid material, *ACS Appl. Mater. Interfaces* **2015**, *7*, 18257−18265.
2. **Joe Gerald Jesu Raj**, Marta Quintanilla and Fiorenzo Vetrone, Near-Infrared Triggered Generation of Reactive Oxygen Species from Upconverting Nanoparticles Decorated with an Organoiridium Complex *J. Mater. Chem. B* **2016**, 4, 3113 - 3120.
3. **Joe Gerald Jesu Raj** and Fiorenzo Vetrone, "Direct Near Infrared Sensing of Cu^{2+} Ions using Curcumin Tagged $LiYF_4$:Tm^{3+}, Yb^{3+} Nanohybrid Material " *ACS Sensors* (To be submitted).
4. **Joe Gerald Jesu Raj** and Fiorenzo Vetrone, "Superparamagnetic Iron Oxide Nanoparticles Tagged with Cyclometalated Heteroleptic Iridium Pendants for the Generation of Reactive Oxygen Species (To be submitted).

CONFERENCE PRESENTATIONS

1. **Joe Gerald Jesu Raj** and Fiorenzo Vetrone, "Cyclometalated Iridium Complex Decorated Upconversion Nanoparticles for Photodynamic Therapy and Cellular Imaging" – Paper presented at the Annual Meeting of *Centre for the Self-Assembled Chemical Structures (CSACS)*, Montreal, Canada, 05 May, 2015.
2. **Joe Gerald Jesu Raj**, Marta Quintanilla and Fiorenzo Vetrone, "Carbon Nanodots as Sensitizers for Visible Upconversion" – Paper presented at the *International Conference on Material Science and Technology*, Montreal, Canada, October 27-31, **2013**.
3. **Joe Gerald Jesu Raj**, Marta Quintanilla, Khaled A. Mahmoud, Andy Ng, Fiorenzo Vetrone and Mohammed Zourob, "Multi-model DNA biosensor based on fluorescence resonance energy transfer between lanthanide doped hybrid core-shell PSA beads and gold nanoparticles" Paper presented at the *Canadian Society for Chemistry (CSC) 2012 Conference*, Calgary, Alberta, Canada, May 26-30, **2012**.